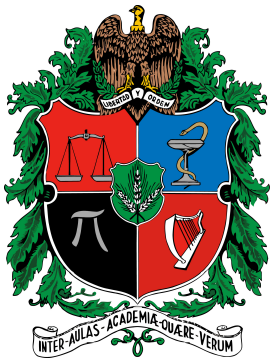

Hot Corrosion Resistance of Dense Ceria-Yttria Stabilized Zirconia/Yttria Stabilized Zirconia (CYSZ/YSZ) Bilayer Coatings Deposited by Atmospheric Plasma Spray

Jhonattan de la Roche Yepes M.Sc

Universidad Nacional de Colombia
Facultad de Minas
Medellín, Colombia
2019

Hot Corrosion Resistance of Dense Ceria-Yttria Stabilized Zirconia/Yttria Stabilized Zirconia (CYSZ/YSZ) Bilayer Coatings Deposited by Atmospheric Plasma Spray

Jhonattan de la Roche Yepes M.Sc

Thesis submitted as a requirement to get for the degree:
Doctor in engineering with emphasis in materials science

Advisor:
Alejandro Toro Ph.D
Co-Advisor:
Juan Manuel Alvarado Ph.D

Research group:
Tribology and Surfaces Group- GTS

Universidad Nacional de Colombia
Facultad de Minas
Medellín, Colombia
2019

Dedicado a todas las personas
que han creído en mí... ¡Gracias!

"I have no special talents. I am only passionately curious".
Albert Einstein

Acknowledgments

Agradezco a mi familia, principalmente a mi esposa, mis suegros y mi Padre por su apoyo, paciencia y total compañía durante el desarrollo de este doctorado.

Agradezco especialmente a mis directores Alejandro Toro y Juan Manuel Alvarado por creer en mí, por su respaldo incondicional y por aportar fuertemente en mi crecimiento como profesional.

A empresas públicas de Medellín (EPM), a los ingenieros Pablo Andrés Gómez y José Andrés Gómez, personal técnico Geovany Fernández y Hugo Hincapié por el apoyo financiero, técnico y facilitar las instalaciones de la empresa para el desarrollo de este proyecto de investigación.

A todos mis compañeros e integrantes del Grupo de Tribología y Superficies por su colaboración, amistad y apoyo durante todo el tiempo que tomó realizar cada parte de este proyecto.

A todas y cada una de las personas que de una u otra forma me animaron y colaboraron para seguir adelante como mis compañeros y amigos Darío, Alex, El Emperador, Juancho y desde las lejanías mis amigas Martha, Angela y Alejandra.

A COLCIENCIAS por la beca Doctorados Nacionales 2014 convocatoria 647.

A la Universidad Nacional de Colombia sede Medellín y a sus profesores por toda la formación académica brindada que contribuyo a mi crecimiento como futuro Doctor.

Abstract

In this work, the hot corrosion (HC) resistance in thermal barrier coatings (TBC) of dense Ceria-Yttria Stabilized Zirconia (D-CYSZ)/ Yttria Stabilized Zirconia (YSZ) deposited using atmospheric plasma spray technique on Inconel 625 substrates was evaluated, varying the layer thickness of CYSZ (0, 50, 100 and 150 μm) maintaining a total coating system thickness of 300 μm. Initially, HC tests were carried out on 7YSZ commercial powders (Metco 204 NS-G) in order to find proper conditions for HC on the deposited coatings. It was found that the mixture of 32 wt.% Na_2SO_4 + 68 wt.% V_2O_5, 1 wt.% salt concentration and 900°C are the most aggressive conditions for HC of YSZ.

Microstructural characterization of the bilayer systems D-CYSZ/YSZ was carried out. D-CYSZ layer presented a DVC type microstructure (Dense Vertically Cracked) with a crack density of 4.32, 3.87 and 3.19 cracks/mm for the layer thicknesses of 50, 100 and 150 μm respectively. YSZ layers presented a porosity of 16% with large, medium and small globular porosity, as well as inter- and intra-splat cracks.

Thermal shock resistance test of the bilayer systems was carried out, showing delamination of the D-CYSZ layer after 359 cycles. However, all the bilayer systems tested exceeded the 600 cycles without presenting delamination of the system at the BC/TC interface above 20%, preserving the thermal protection of the substrate after these cycles.

Finally, HC test showed that although the dense layers presented vertical cracks, they gave the projection against molten salt attack, since the YSZ system (without D-CYSZ) presented severe changes in its microstructure under the HC test parameters found in the work (HC-standard). In addition, under most aggressive conditions (varying concentration and cycles) D-CYSZ layer acted as a barrier and protect the subsequent layers, since YSZ system showed delamination and higher cohesive weakness than the systems with D-CYSZ layer.

Keywords: Hot corrosion, APS, YSZ, CYSZ, TBC.

Resumen

En este trabajo, se evaluó la resistencia a la corrosión en caliente (HC) en recubrimientos barrera térmica (TBC) de circonia estabilizada con ceria e itria densa (D-CYSZ)/circonia estabilizada con itria (YSZ) depositadas con la técnica de aspersión térmica por plasma atmosférico (APS) sobre sustratos de Inconel 625, variando el espesor de capa de D-CYSZ (0, 50, 100 y 150 μm) manteniendo un espesor total del sistema de 300 μm. Inicialmente, se realizó pruebas HC en polvos comerciales de 7YSZ (Metco 204 NS-G) con el fin de hallar las condiciones para las pruebas en los recubrimientos. Se encontró que la mezcla 0.32 wt.% Na_2SO_4 + 0.68 wt.% V_2O_5, 1 wt.% de concentración de sal y 900°C son las condiciones más agresivas para pruebas HC en YSZ.

Se realizó la caracterización microestructural de los sistemas bicapa D-CYSZ/YSZ. La capa de D-CYSZ presentó una microestructura tipo DVC (*Dense Vertically Cracked*) con densidad de grietas de 4.32, 3.87 y 3.19 grietas/mm para las capas de 50, 100 y 150 μm respectivamente. Las capas de YSZ presentaron la microestructura típica de un sistema TBC, con una porosidad del $\sim$16% con porosidad globular de gran, mediano y pequeño tamaño, así como grietas inter e intra splat.

Se evaluó la resistencia termo-mecánica de los sistemas bicapa, donde presentaron desprendimiento de la capa de D-CYSZ a partir del ciclo 359. Sin embargo, todos los sistemas TBC evaluados superaron los 600 ciclos sin presentar delaminación del recubrimiento en la intercara BC/TC por encima del 20%, preservando la protección del sustrato despues de esos ciclos.

Finalmente, las pruebas HC mostraton que aunque las capas densas presentaron grietas verticales, estas dieron protección ante el ataque por sales, ya que el sistema YSZ presentó cambios severos en su microestructura bajo las condiciones HC halladas en el trabajo (HC-standard). Además, en condiciones más agresivas (variando la concentración y en ciclos) el sistema YSZ presentó delaminación y mayor debilidad cohesiva que los sistemas con capa D-CYSZ.

Palabras clave: Corrosion en caliente, APS, YSZ, CYSZ, TBC.

Contents

List of Figures

List of Tables

1 Introduction

Energy supply in Colombia is highly reliable despite the dependence of the country on hydroelectric power plants (circa 70%), with thermoelectric plants accounting for 29% and other sources such as coal, wind power, etc. responsible for only 1%. In spite of seasons of low rainfall, and even when the water reservoir levels are critical, *"it is practically impossible that there will be blackouts and rationing"* [1]. However, according to the *Asociación Colombiana de Generadores de Energía Eléctrica (Acolgen)* it is mandatory to increase the competitiveness of the sector by lowering the cost of energy. For example, during periods of "El NIÑO" (low rainfall) the cost of energy rises and hydroelectric production is low *"since thermoelectric power plants meet demand, but the cost of gas is between 3 and 4 times higher than when using water"* [1]. Since the price of gas doesn't depend on the thermoelectric power plants, a practical way to reduce the price of thermoelectric energy production is by increasing the generation efficiency and by decreasing operating costs.

Over the last 30 years, the efficiency of the gas turbines increased due to the improvement in the design of the alloy chemistry, casting engineering (i.e., directionally solidified and a single crystal) and blades with internal cooling channels into the component [2]. Additionally, a considerable increase in turbine efficiency has been achieved through the use of thermal barrier coatings (TBCs) in the hot gas path where the parts exposed to the highest operational temperatures (combustor chamber, liner, first stage blades, among others), and the conditions of the components exceed the inherent capacity of the base material [2–4]. The use of TBCs with a thickness between 100 and 500 μm, together with the internal cooling of the component, provides a reduction in the alloy surface temperature between 100 and 300°C, which allows modern gas turbines to operate at temperatures close to the incipient melting point of the current superalloys (1300°C) [5].

A thermal barrier coating system is typically composed of 3 layers (two ceramic and one metallic) called Bond Coat (BC), Thermally Grown Oxide (TGO) and Topcoat (TC) onto a metallic substrate (e.g., a Ni-based superalloy). Y_2O_3-stabilized ZrO_2 (7YSZ) solid solution is typically used as a TC, the addition of 7 to 8 wt% ($\sim$ 4 to 4.5 mol%) of Y_2O_3 stabilizes the non-transformable tetragonal phase (t') at high temperature. This variation of the tetragonal phase (t) does not undergo the martensitic transformation to monoclinic phase during cooling and is more stable [5,6]. Moreover, t' combined with porosity and microstructural defects provides multiple desirable properties that make it a material of choice for the TC, such as lower thermal conductivity (i.e. 1.2 and 1.8 $Wm^{-1}K^{-1}$) [7,8], high thermal expansion coefficient ($\sim$11x10^{-6} °C^{-1}) closed to the bond coat ($\sim$14x10^{-6} °C^{-1}), highly compliance and strain tolerance. Most important, this composition range where the ferroelastic toughening mechanisms are active, making 7YSZ TBCs mechanically robust [6].

As an alternative to natural gas, thermoelectric turbines can operate with liquid fuels such as fuel oil, diesel, and biodiesel, which are more economical, available and/or efficient than gas. However, when low-grade fuels are used, their impurities, for instance, Sodium (Na), Vanadium (V) and Sulfur (S) are oxidized during combustion to form salts that have strong acid-base properties, such as Sodium sulfate (Na_2SO_4) and Vanadium pentoxide (V_2O_5). These salts in molten state infiltrate through the TC thickness and react with Y_2O_3, accelerating the tetragonal to monoclinic transformation process due to the destabilization of phase t' [9–11]. This type of degradation is a form of Hot Corrosion (HC).

Considering the effects caused by the fuel contaminants in turbine components, many efforts have been focused on investigating TBCs with better HC resistance, such as TC architectures with different microstructures (e.g. bilayer structures, densified vertical cracking overlays and functionally graded strcutures) [12–15], and other materials with higher HC resistance to molten salts like $Gd_2Zr_2O_7$ [16, 17], $La_2(Zr_{0.7}Ce_{0.3})_2O_7$ [18], and ZrO_2 stabilized with In_2O_3, Sc_2O_3, Ta_2O_5 [19–21]. Ceria-Yttria Stabilized Zirconia (CYSZ) is one of the candidates that have shown good resistance to molten salts [10, 22] because Cerium oxide (CeO_2) as stabilizer of *t* phase in Zirconia has more acidity than Y_2O_3 (Lewis acid-base nature), making the reactions with the molten salts slower [23]. Moreover, CYSZ has higher thermal expansion coefficient, lower thermal conductivity, more phase stability and higher thermal-shock resistance than 7YSZ [24] make it a good candidate to use it for TBCs applications.

Combining the concept of TC architectures with the better HC resistance of the CYSZ, this work studies the HC resistance of different TBC's bilayer architectures as a function of thickness of a dense Ceria-Yttria Stabilized Zirconia (D-CYSZ) overlay onto the porous 7YSZ layer, observing changes in terms of microstructure and morphological features as a consequence of exposure to mixture of V_2O_5 and Na_2SO_4 molten salts.

2 Objectives

2.1 General objective

To study the effect of using a dense Ceria-Yttria Stabilized Zirconia (D-CYSZ) overlay on the Hot-Corrosion resistance of Yttria Stabilized Zirconia (YSZ) Thermal Barrier Coatings deposited by Atmospheric Plasma Spray onto Ni-base superalloy.

Specific Objectives

- To develop a laboratory methodology to reproduce in-service salt-induced hot-corrosion (HC) attack to investigate the degradation mechanisms on CYSZ, YSZ and NiCoCrAlY specimens.
- To establish deposition protocols (surface preparation, cleaning and spraying parameters) for NiCoCrAlY bond-coat, YSZ top-coat and D-CYSZ overlay by Atmospheric Plasma Spray.
- To evaluate the Na_2SO_4/V_2O_5 induced HC attack on D-CYSZ/YSZ/NiCoCrAlY/Superalloy coating systems as a function of the D-CYSZ thickness.
- To characterize the changes in microstructure and morphological features of the coatings obtained, including pores, cracks, phases and oxides present, among others, as a consequence of the exposition to thermal fatigue and hot corrosion conditions.

3 | Background

3.1 Thermal Spray

Thermal spray is a generic term for a group of coating processes used to apply metallic and nonmetallic coatings onto a wide variety of substrates. These processes are grouped into three major categories: Flame spray, electric arc spray, and plasma spray. These energy sources are used to heat the coating material (in powder, wire or rod form) to a molten or semi-molten state. The resultant heated particles are accelerated and propelled toward a prepared surface by either process gases or atomization jets. Upon impact, a bond forms with the surface, and the arrival of subsequent particles causes thickness buildup and formation of a lamellar structure, as it is shown in figure 3.1.

Figure 3.1: Principles of thermal spray [25].

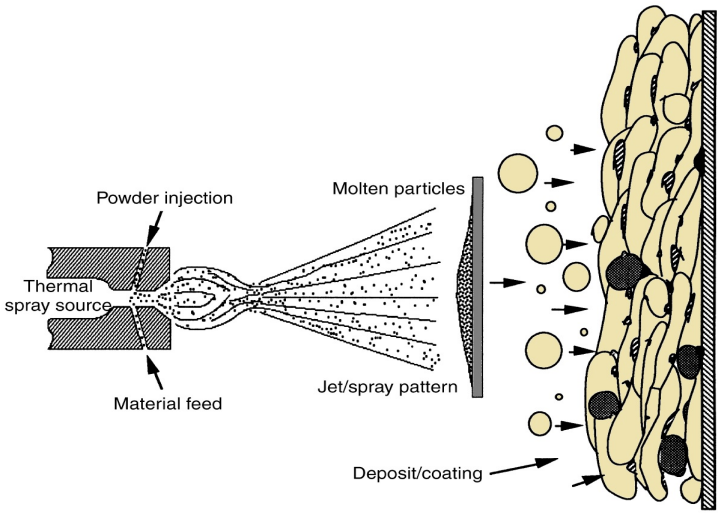

One advantage of thermal spray processes is the extensive wide variety of materials that can be used to produce coatings; indeed, any material that melts without decomposing can be used as a feedstock. A second advantage is the ability of most thermal spray processes to apply coatings without significant heat input to the substrate. Thus, materials with high melting points, such as tungsten, can be applied to finely machined, fully heat-treated parts without changing the properties and in the absence of excessive thermal distortion of the part. A third advantage is the ability, in most cases, to strip off and recoat worn or damaged coatings without changing part properties or dimensions. A disadvantage is the line-of-sight nature of these deposition processes, which means that only the areas that the torch or gun can “see” are coated; for that reason, there are also size limitations, for example it is

impossible to coat small, deep cavities into which a torch or gun will not fit.

Thermal spray technologies differ from other deposition processes in that they are not an atomic deposition. They do not deposit material onto surfaces as individual ions, atoms, or molecules; because they are high-enthalpy (high energy density) processes, with high deposition rates relative to other coating processes such as chemical vapor deposition (CVD), physical vapor deposition (PVD), and electroplating. Additionally, thermal spray processes are capable of operating over a broad range of temperature, velocity, and atmospheric conditions, enabling them to apply the largest variety of materials. Finally, thermal spray coatings are considered to be "overlay" coatings, which can be defined as materials added to an original surface (called the substrate) where there is little or no mixing or dilution between the coating and the substrate, thus preserving the composition of the base material. However, diffusion and alloying often occur with thermal spray coatings, but the reaction zone is extremely narrow due to the excessively rapid cooling rates of the individual molten droplets impacting the relatively massive and cold substrate [25].

3.1.1 Plasma spray

In plasma spraying, an electric arc generates plasma within a plasma torch. The arc is struck between a cathode and a cylindrical anode nozzle, and the plasma gas is injected at the base of the cathode, heated by the arc, and exits the nozzle as a jet at high temperature and velocity. Figure 3.2 presents the scheme of plasma spray.

Figure 3.2: Schematic diagram of the plasma spray process [26].

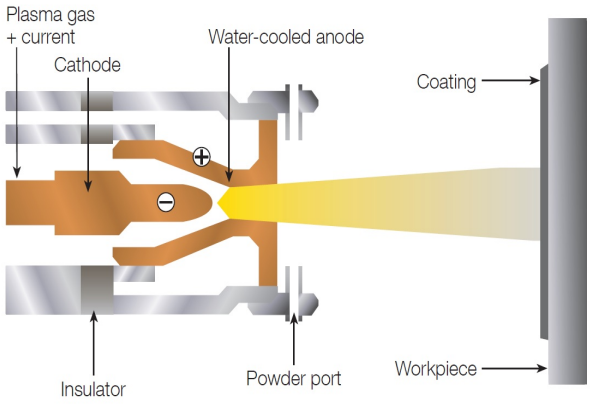

Peak temperatures at the nozzle exit can be 12000 to 15000 K, and peak velocities range from 500 to 2500 m/s, (subsonic velocities at these temperatures) depending on torch design, plasma gases, and operating parameters. Powders are generally injected radially into the plasma jet downstream of the arc root either inside the nozzle while the jet is still confined or right outside the nozzle and the angle of injection can be perpendicular to the jet axis or with a small angle against the direction of the plasma flow. The spray particles are heated and accelerated by the plasma and projected to the substrate where they form splats and eventually the coating [27].

Plasma spray can be performed as:

1. Atmospheric plasma spaying (APS), where the plasma jet exits the torch into the atmospheric environment (i.e., air lab).
2. Controlled atmosphere plasma spraying (CPS), where the jet exits the torch under a chamber with controlled atmosphere (generally argon), for example, to avoid exposure to oxygen.
3. Low-pressure plasma spraying or vacuum plasma spraying (LPPS or VPS), where the jet exits the torch into a low-pressure chamber at about 10-30 kPa.

Process parameters

- Arc plasma

Working gases composition: Typical plasma jets use argon together with another secondary (auxiliary) gas because pure argon creates a low-energy plasma, which is related to its ionization potential and thermal heat capacity. Nitrogen, on the other hand, is one of the hottest plasma gases; however, it is also a reactive gas and has some material limitations. Argon mixtures with 20 to 50$\%$ vol. of helium are often used as it increases the thermal conductivity of the plasma stream, improving the heat capability of the plasma. Argon/hydrogen mixtures are also commonly used, with hydrogen additions of approximately 5 to 15$\%$ vol., which provide increased enthalpy over argon/helium due to the diatomic structure of hydrogen and its high collisional cross-section related to its low mass [25]. The trade-off with increased enthalpy is decreased anode/cathode life, consumable life with one common gun design using argon/hydrogen is 8 to 40 hours where another design will be 100 to 160 hours. In ascending order of enthalpy, the common plasma gas combinations are:

- Argon (Ar)
- Argon/Helium (Ar/He)
- Argon/Hydrogen (Ar/H_2)
- Nitrogen/Hydrogen (N_2/H_2)

Anode lifetime may be more a function of increasing copper contamination as the electrode wears. Those components with higher wear rates have yet shorter usable lives because of copper spitting [25].

Electric power: The power depends on the type of plasma torch, typically is up to 80 kW, and can reach to 200 kW in water stabilized torches or even 250 kW in high power ones [28]. The power is directly related to the properties of plasma, such as enthalpy, viscosity, and density [26]. These directly affect the temperature and speed of the particles, modifying the characteristics of the coating.

Geometry of electrodes: The cathode tip should have different shapes for different working gases. The geometry (profile, diameter) of an electrode influences the plasma flow pattern, temperature, and velocity. For example, application of a convergent-divergent anode nozzle was reported to reduce arc-voltage fluctuations. The electric arc "contacts" the anode and cathode in one or more places (roots) resulting in deterioration and wear, this occurs due to the high density of heat flux reached in an arc spot, 10^8 W/m^2 [28].

Plasma stabilization: with a relatively low frequency below 3000-4000 Hz is the prime source of statistical variance in the in-flight particle velocity and temperature; for example, particle temperature and velocity variations up to 600 °C and 200 m/s respectively were observed for ceramic particles. Thus, a particle traveling on a peak of plasma energy may be overheated, while another particle traveling at minimum plasma energy may have a temperature below the melting point, hence forming "unmelts" and other related defects in a coating or begin just bounced off the surface. Figure 3.3 illustrates the time dependence and corresponding spectra on the voltage fluctuation. The data show that the maximum intensity of fluctuation was observed around 4000 Hz and Argon plasma has a minimum level of the voltage fluctuation compared with Ar/H_2 plasma; moreover, the increase of fluctuation was also observed when worn electrodes were used during the experiments [26].

Figure 3.3: Time dependence (a) and corresponding power spectra (b) on the voltage fluctuation for new, and used electrodes, and for two gas mixtures. Plasma parameters, 50 slmp Ar or 4/50 slmp H_2/Ar, 500 A, 3 μs sampling time [26].

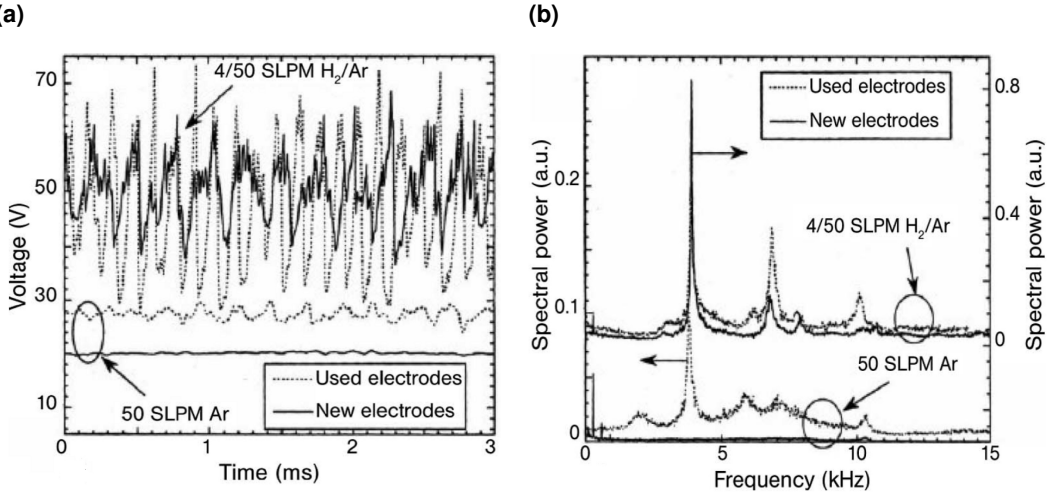

- Powder

The properties of the powder have a considerable influence on the quality of the coatings and are classified into physical and chemical ones:

Physical:

- Granulometry
- Internal and external morphology
- Apparent density and flowability
- Thermal properties

Chemical:

- Chemical composition
- Phase content

- Element distribution

There are many routes for powder production, including chemical precipitation processes, mechanical crushing/milling or thermal treatments (atomizing/sintering). In general, feedstock requires a defined morphology (usually spherical) and a well-defined powder-size distribution. Wide tolerances in particle-size distribution, particle shape, and chemistry reduce the powder costs considerably; however, this leads to an increase in the scattering of the coating process and finally a reduction of coating quality [26]. Table 3.1 shows the industrial methods to produce powders with different morphologies.

Table 3.1: Different powder-production processes used for different spray powders leading to different morphologies [26].

Production process	Material	Spray powder	Particle morphology
Gas, water atomized	Metals, alloys	Cu, Ni, Co,Ni50Cr, NiCrAlY, Zr, Ti, Ni20Cr	Gas atomized: more round, more expensive Water atomized: coarse, cheaper, dense particles
Fused and crushed	Oxides	Al_2O_3, Al_2O_3–TiO_2, Cr_2O_3, ZrO_2–Y_2O_3	Blocked, dense particles
Sintered and crushed	Oxide, carbides	Al_2O_3–TiO_2, Cr_2O_3, WC-Co, WC–10Co4Cr	Blocked, porous particles
Spheroidized (with a plasma gun)	Metals, carbides	Mo, WC–17Co	Changed from blocked to round Porous particles
Agglomerated (spray dried)	Oxide	ZrO_2–Y_2O_3	Porous particles
Agglomerated, sintered, spheroidized	Metals, oxides, carbides	Cr_3C_2-NiCr, ZrO_2–Y_2O_3, Mo, WC–Co, Hydroxyapatite	Porous particles
Cladded	Alloys, carbides	NiMoAl, Ni_5Al, WCNi	Dense particles

All the parameters mentioned above are directly reflected in the coating quality:

- Particle size influences the particle trajectory in the plasma/hot gas plume and, consequently, its in-flight thermal history and the shape of the coating spot, which in turn determine the coating microstructure, deposition efficiency, and thickness.
- Particle morphology (as seen in figure 3.4) affect the feeding conditions (by influencing the apparent density) as well as injection conditions and in-flight parameters since they influence the aerodynamic forces and heat fluxes in the gas flow.
- Powder chemical composition and specific physical characteristics (e.g. crystalline phase structure) determine the coating's functionality.
- The powder flowability strongly affects the powder feeding and injection conditions.
- Powder density influences the deposition rate (in the case of volumetric powder metering) with an effect on the coating thickness.

- The powder specific surface is an important characteristic that influences particle in-flight treatment and density of voids and microcracks in the coating [26].

Figure 3.4: Different types of powder morphologies, (a) crushed and milled powders, (b) spray-dried agglomerated powders, (c) spray-dried and sintered powders, and (d) plasma-densified (spheroidized) powders [26].

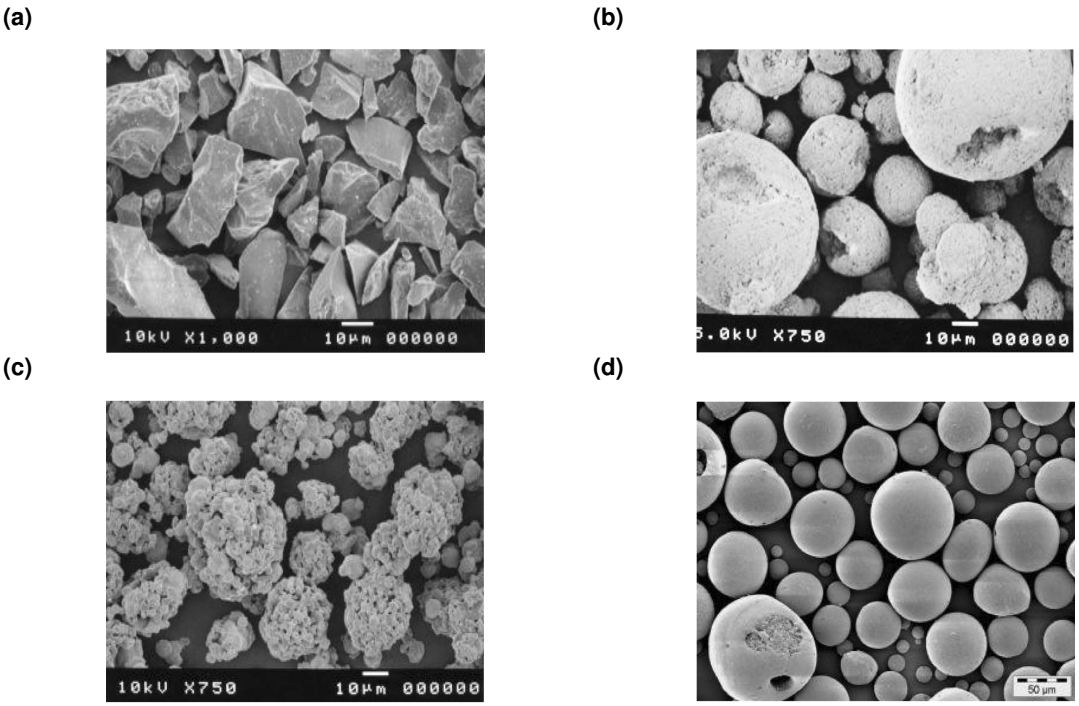

- Other important process parameters

- **Spray distance:** It affects the dwell time of particle and therefore its temperature generally is in the range 60 to 130 mm.
- **Spray velocity:** Is the velocity of the torch regard to the substrate, it is in the range 50 to 2000 mm/s.
- **Substrate temperature:** It is an important practice to eliminate a moisture from the sample surface. Moreover, preheat produce a pre-expansion of the substrate so that it subsequently shrinks with the coating, reducing the residual stress created in the coating during cooing, specially when spraying ceramics onto metals [25, 28]. Usually, the temperature should be kept in the range of 373 to 423 K [28], however heat at temperature between 373 to 423 K during 60 seconds is sufficient to remove moisture [25]. Some metals such as aluminum and aluminum alloys, copper and copper alloys, titanium and manganese alloys are not recommended to pre-heat, because accelerates the oxide film growth and interfere with coating adhesion. In the case of stainless steels and Ni-base superalloys, the best pre-heat temperature is close to 373 K followed by a quick application of the first pass of sprayed material, this precaution is recommended to avoid the gowning of refractory oxide which interferes with coating adhesion mechanisms [25].

- **Post spraying treatment:** It is used to improve coating density and other properties Some examples include [28].
  - Furnace annealing
  - Laser treatment
  - Sealing with organic and inorganic sealants
  - Spark-plasma treatment

Coating characteristics

Among the essential plasma spray coating features characteristics to define the properties of the coating include: the lamellar splat structure, entrapped unmelted or resolidified particles, pores, oxide inclusions, grains, phases, cracks and bond interfaces [25]. Figure 3.5 illustrates the scheme of typical coating characteristics on a cross-section SEM micrograph of YSZ coating deposited by APS.

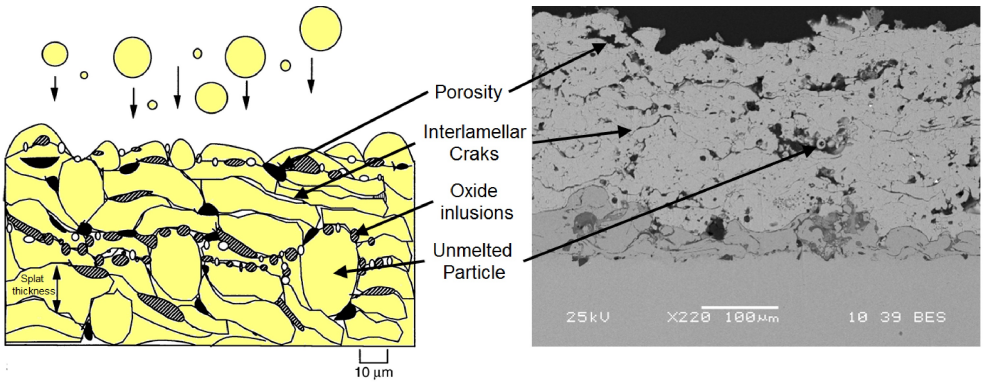

Figure 3.5: Cross-section of the plasma spray coating microstructure [25, 29].

The basic unit that describes a plasma spray coating microstructure is the *"splat"*, this is the term given to a single impacted droplet/particle (see in figure 3.6a). A continuous coating layer is composed of many overlapping splats that solidify and adhere to one another; thus, the splat is the basic structural building block in thermal spray, including APS. The splats are formed when the accelerated molten particles impact a prepared surface, spread over (become flattened and form lamellar structures), and fill the underlying interstitial spaces. Finally, they solidify into columnar or fine-grained equiaxial crystals [25, 27]. Figure 3.6b shows the scheme of a splat structure, where these are seen on edge, revealing the characteristic lamellar structure.

In general, thermal spray processes are also characterized by rapid solidification, with rates (for metals) between 10^5 to 10^8 °C/s, producing grain sizes with smaller than 5μm [25]. The solidification starts after contact of the molten particle with the substrate, where the heat is dissipated through the substrate normal to the deposition direction. The splat area in contact with the substrate serves as a "heat-sink" and nucleation of the crystals starts from this surface. For the first splats striking the cold and smooth substrate, nucleation would be heterogeneous (starts from the cold substrate) and the grains grow columnar as shown in figure 3.6c. On the other hand, a fine-grained equiaxed microstructure has a homogeneous nucleation (starts inside the lamella), and is favored by a lower rate of heat dissipation at

Figure 3.6: (a) SEM micrography of a individual splat, (b) typical plasma spray splat structures, (c) columnar structure [25, 30, 31].

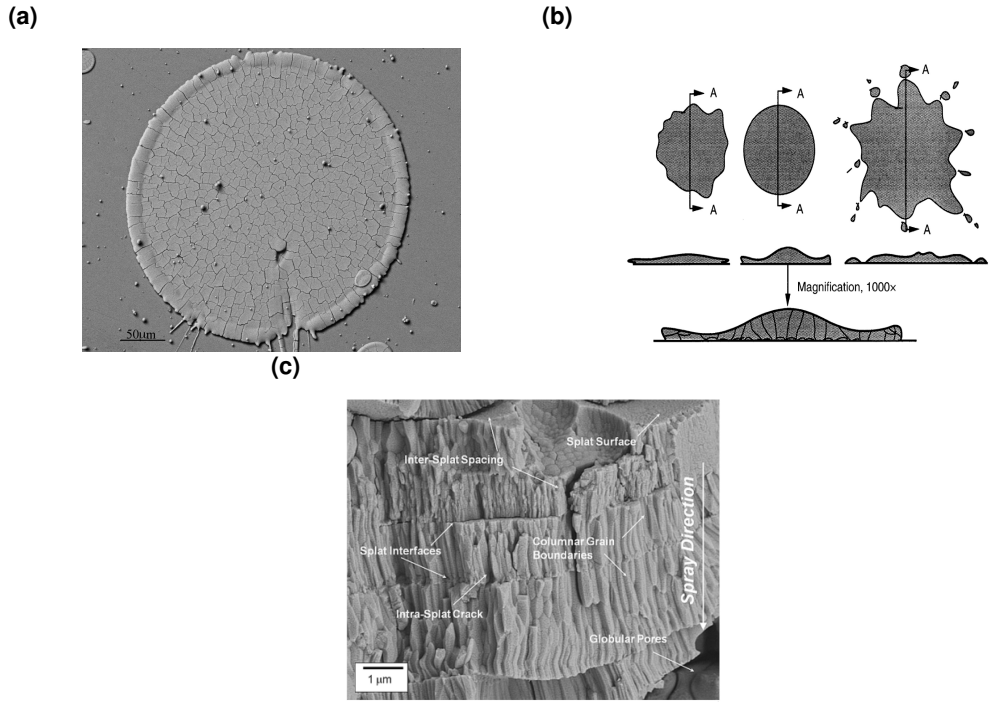

the interface with the substrate (or a previously deposited layer) caused by the increase in thermal contact resistance (resulting from substrate oxidation and/or roughness) and/or increase in substrate temperature [28].

Oxide stringers: Oxide inclusions (stringers) are produced by particle/atmosphere interaction and/or heating of the coating surface during deposition, in the case of interaction with the air, the particle surface forms oxide and/or nitride films. Longer dwell times and higher particle temperatures increase the thickness of these films, producing higher concentrations of oxide stringers withing the coating.

It has been found that the oxides may reach hardnesses exceeding 1000 DPH (Diamond Pyramid Hardness). Therefore, the composite mixture of metal and metal oxides becomes harder than the metal coating itself. This increased hardness can lead to brittle coatings due to the reduced ductility of the oxides. If the amount of oxides is too high the cohesive strength of the coating is reduced. Usually, oxide or nitride inclusions are often considered detrimental to coating properties; however, in some applications, they are desired because they can increase wear resistance or lower thermal conductivity [25].

3.2 Thermal Barrier Coatings- TBCs

A Thermal Barrier Coating (TBC) is a multilayered-multimaterial system composed of a substrate and different layers made of different materials (e.g., two ceramic and one metallic) with specific properties and functions. As it is shown in figure 3.7, a typical TBC system is composed by a Bond Coat (BC), a Thermally Grown Oxide (TGO), and a ceramic Top Coat

(TC) layer. These layers are commonly applied by thermal spray techniques such as Atmospheric Plasma Spray (APS), High Velocity Oxyfuel (HVOF), Low Pressure Plasma Spray (LPPS), and Flame spray. Other techniques such as cathodic arc/ion plasma deposition and Electron Beam Physical Vapor Deposition (EB-PVD) are also used [32, 33].

Figure 3.7: Cross-sectional SEM view of (a) Electron-Beam Physical-Vapor Deposited (EB-PVD) TBC, superimposed onto a schematic diagram showing the temperature reduction provided by the TBC; (b) Atmospheric Plasma Sprayed (APS) TBC that has been subjected to 120 thermal cycles; (c) mechanism by which TBCs reduce the temperature of the turbine blade [5, 34].

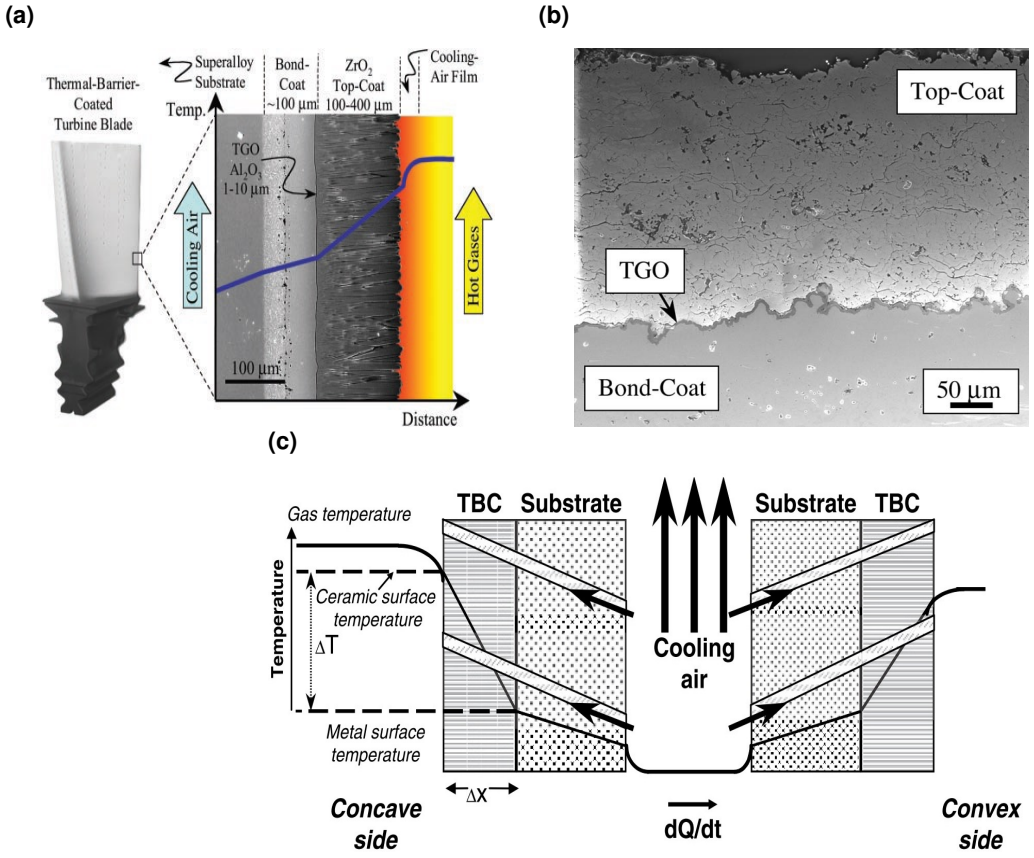

Many engineering design factors influence the overall efficiency of gas-turbine engines, but one of the most effective to increase the turbine engine efficiency is the use of TBCs. Typically, parts such as the combustor, vanes, and blades of gas-turbine engines used for aircraft, marine propulsion, and power generation are coated with $\sim$7 wt% Y_2O_3-stabilized ZrO_2 (7YSZ) ceramics with a thickness between 100 to 500 μm, which along with internal cooling of the underlying (figure 3.7c), provide a significant decrease of the surface temperature (100 to 300 °C). This progress has allowed to modern gas-turbine engines to operate at temperatures above the melting temperature of the superalloy ($\sim$ 1300°C), thereby improving engine efficiency and performance [5, 32]. The figure 3.8 shows the increment of gas-temperature facilitated by the use of TBCs, in conjunction with innovative air-cooling approaches, has been much higher than that enabled by earlier materials advances, including the development of single-crystal Ni-based superalloys [4].

Figure 3.8: Progression of temperature capabilities of Ni-based superalloys and thermal-barrier coating (TBC) materials over the past 50 years [6].

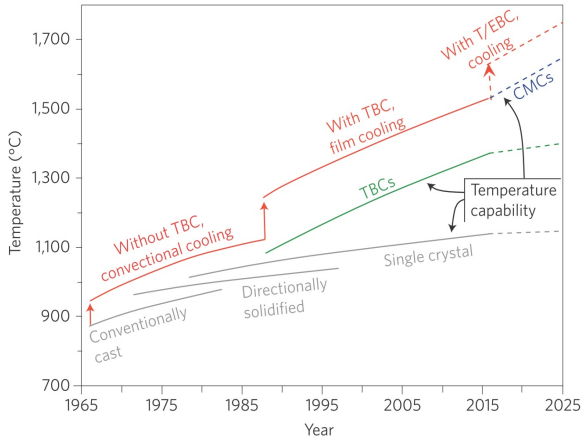

3.2.1 Constituents of TBCs system

Substrate: Material used in gas turbine engines is a unique class of complex alloys based on Ni and Co that not only exhibits extraordinarily high strength, but also maintains strength across a wide elevated temperature range ($\geq$ 80% of the melting point), hence the name "superalloys" [34]. The microstructure of a typical superalloy consists of different phases [34–36] which are:

- **Gamma phase (γ):** This phase has an FCC structure, forms a continuous matrix in which other phases reside. Elements such as iron, chromium, ruthenium, molybdenum, rhenium, and tungsten stabilize this phase, (see figure 3.9a).
- **Gamma prime phase (γ'):** This intermetallic forms a precipitate phase coherent with the γ-matrix with composition Ni_3(Al, Ta, Ti). Aluminium, titanium, niobium, and tantalum, have greater atomic radii and promotes its formation. In Nickel-Iron superalloys and those rich in niobium, an ordered phase, γ"(Ni_3Nb), is preferred instead of γ', (see figure 3.9a).
- **Carbides and borides:** Carbon present at concentrations up to 0.2 wt%, combines with reactive elements such as titanium, tantalum, and hafnium to form MC carbides. During turbine operation, these can decompose to other species, such as $M_{23}C_6$ and M_6C, which prefer to reside on the γ-grain boundaries, and which are rich in chromium, molybdenum and tungsten. Boron can combine with elements such as chromium or molybdenum to form borides which reside on the γ-grain boundaries.
- **Other phases:** In service-aged conditions can be found the topologically close-packed (TCP) phases: μ, σ, Laves etc., (see figure 3.9b).

Superalloy strengthening mechanisms include solid solution as well as coherent and incoherent precipitation. In the case of solid solution mechanism, several metallic elements dissolve in the γ matrix (e.g. Cr, Co, Fe, Mo, Ta, W, and Re in Ni-base alloys whereas Ni, Cr, Mo, W, Nb, and Ta in Co-base alloys) substituting atoms of the Nickel or Cobalt cells. This replacement creates stress fields that impede dislocation motion by interacting with the stress fields of dislocations, increasing strength. Incoherent precipitates are carbides type

Figure 3.9: Examples of the phases formed in a René N5 Ni-base superalloy: (a) the high-temperature strength phases γ and γ' and (b) TCP precipitates [36].

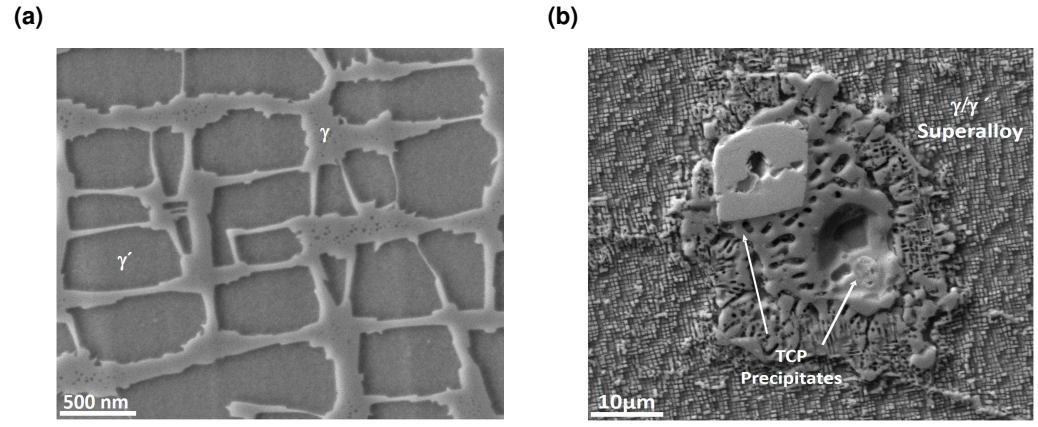

MC and $M_{23}C_6$ formed during the processing and heat treatment. Carbides within grains impede dislocation motion while grain boundary carbides pin boundary movement, discouraging grain growth and limiting grain boundary sliding. This is the primary strengthening mechanism of Co-base superalloys. γ' and γ" are the coherent precipitates, which also prevent dislocation motion and increase the strength. Coherent precipitates have little driving force for growth in size, and therein lies the clue to the strength retention of γ'-strengthened superalloys over a wide high-temperature range [34].

In the early years of turbine development, the understanding between age hardening, creep and γ' volume fraction and the steadily increasing operating-temperature requirements for the aircraft engines, resulted in the development of wrought alloys with increasing levels of aluminum plus titanium. However, component forgeability problems led to this direction of development not going beyond a certain extent, for that reason, the composition of the wrought alloys became restricted by the hot workability requirements. This situation led to the development of conventional equiaxed cast nickel-base alloys, their compositions can be tailored for good high temperature strength as there was no forgeability requirement. Furthermore, the cast components are intrinsically stronger than forgings at high temperatures, due to the coarse grain size of castings [37]. Directional solidification (DS) is also being employed to produce advanced technology nozzles and blades; the result is a blade with an oriented grain structure that runs parallel to the major axis of the part and contains no transverse grain boundaries, as in ordinary blades. The elimination of these transverse grain boundaries confers additional creep and rupture strength on the alloy, and the orientation of the grain structure provides a favorable modulus of elasticity in the longitudinal direction to enhance fatigue life. The use of directionally solidified blades results in a substantial increase in the creep life or a substantial increase to the stress at a fixed life [38]. Nowadays, the superalloy (nickel or cobalt based) component is investment-cast in single crystal (SC) or polycrystalline forms, and it contains as many as 5 to 12 additional elements that are added for the enhancement of specific properties such as high-temperature strength, ductility, oxidation resistance, hot corrosion resistance, and castability [5]. Figure 3.10 schematically shows the improvement in creep strength of a cast superalloy by switching over from equiaxed polycrystalline investment casting to DS casting to SC casting.

Figure 3.10: Relative creep deformation of equiaxed, DS, and SC superalloy castings [37].

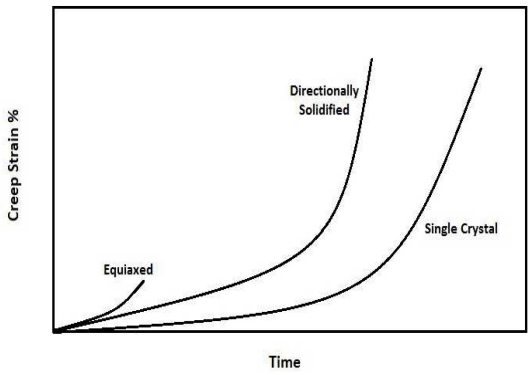

Bond coat (BC): This is a metallic layer that improves the adhesion between the substrate and the ceramic top coat. Additionally, it protects the substrate against corrosion and oxidation due to the formation of Al_2O_3 scale during high-temperature exposure, and reduces the stresses caused by the difference in thermal expansion between the top coat and the substrate. The first bond coats were the nickel aluminides (e.g., NiAl), but they showed poor resistance against sulfidation. The addition of Platinum was beneficial to this alloy in terms of reducing Al_2O_3-scale spallation, and improving their oxidation behavior. These types of bond coat are usually made by diffusion processes [39, 40]. Another type of bond coat is the two-phase overlay γ+β MCrAlX coatings (where M = Fe, Co, Ni or NiCo and X = Y, Hf, Si, or other minor additives such as Re). The MCrAlY type bond coats usually contain (in wt-$\%$) 15–25$\%$Cr, 10–15$\%$Al and 0.2–0.5$\%$Y, and consist of a β-NiAl phase in a γ-Ni matrix. The choice of M depends on the atmosphere in which the coating operates, for example, NiCrAlY coatings have a lower resistance against sulfidation than CoCrAlY coatings, but their mechanical strength is higher. Table 3.2 lists the compositions of some common overlay coatings. Bond coats are typically 100–150 μm thick, and are applied using a variety of overlay processes: APS, HVOF, LPPS, cathodic arc/ion plasma deposition or EB-PVD. [32, 40].

It is important to point out that the composition of a diffusion coating is dictated by thermodynamic and kinetic constraints; on the other hand, the composition of an overlay coating is dictated mainly by the composition or elemental ratio of the coating source. Consequently, the composition of an overlay coating can be easily varied to specific requirements and hence can often provide superior protection compared to the diffusion coatings. However, most of the bond coats applied to superalloy components are diffusion coatings [39] due to the cost of the overlay coating processes which are about 2–4 times more expensive than the diffusion processes [32]. The selection between these coating types by turbine engine manufacturers is based on experience, design philosophy, performance, and cost. In general, bond coats must fulfill the following characteristics [32]:

- Minimal interdiffusion with the substrate to minimize Al depletion and upward diffusion of refractory elements and impurities such as S, and avoid the formation of "secondary reaction zone" (SRZ) below the bond coat on the newer generation of Ni-based superalloys.
- Minimal strain misfit with the substrate resulting from thermal expansion differences.

Table 3.2: Compositions of some commonly used and prototype MCrAlY overlay coatings, in weight % [35].

	Ni	Co	Cr	Al	Y	Ti	Si	Hf	Others
NiCrAlY	Bal		25	6	0.4				
NiCrAlY	Bal		22	10	1				
NiCrAlY	Bal		31	11	0.6				
NiCrAlY	Bal		35	6	0.5				
CoNiCrAlY	32	Bal	21	8	0.5				
CoCrAlY	-	Bal	25	14	0.5				
NiCoCrAlTaY	Bal	23	20	8.5	0.6				4 Ta
NiCoCrAlYSi	Bal	0-40	12.5-20	2-8	0-0.25	0-10	2-10		0-4 Nb 0-4 Mo 0-20 Fe 0-5 Mn
NiCrAlTi	Bal		30-40	1-10		1-5			
NiCoCrAlHf	Bal	0-40	10-45	6-25				0-10	

- High creep strength to suppress plasticity/rumpling effect.
- Compatibility with the process to coat the internal cooling passages of the blade.
- Minimum use of Pt and other expensive elements such as Ru, Re, and Pd.
- Minimally affected by impurities such as S, C, and others.

Thermally Grown Oxide (TGO): At peak operating conditions the bond coat temperature in gas-turbine engines typically exceeds 700 °C, resulting in bond coat oxidation and the inevitable formation of a third layer (i.e., the thermally grown oxide TGO, 1 to 10 μm in thickness) between the bond coat and the ceramic topcoat. Although the formation of the TGO is inevitable, the ideal bond coat is engineered to ensure that the TGO forms as α-Al_2O_3 and due to it is slow-growth, uniform, and defect free; so as to, a TGO has a very low oxygen ionic diffusivity and provides an excellent diffusion barrier, retarding further bond coat oxidation [5]. Nonetheless, based on electron microscopic characterization, the general microstructural features of the TGO formed on overlay coatings of MCrAlY is composed of large and elongated alumina grains at the TGO metal interface (see figure 3.11). This morphology is such that oxygen diffusion in the alumina grains is faster than aluminum diffusion. Moreover, Yttrium can get oxidized either as garnet, $Y_3Al_5O_{12}$, or as segregates as finer precipitates. Zirconium is also found within the TGO, leading to the speculation that some of the alumina has formed at the expense of the reduction of zirconia at high temperature ($\sim$1200 °C), where such reduction is thermodynamically feasible [34].

However, the TGO growth rate affects the eventual spallation of the TBC when it is cycled at high temperature in an oxidizing environment. Experimental and field data from aircraft gas turbine engines suggest that typical TGO thickness at TBC spallation is in the 6 to 7 μm range and certainly below 10 μm [34]; on the contrary, Dariola et al, observed thermally grown oxide thickness up to 17 μm before failure in the β-NiAl bond coat [32].

Top coat (TC): This layer provides thermal insulation to the TBC system. Moreover, it must fulfill some basic requirements: high melting point, no phase transformation between room

Figure 3.11: TGO microstructure [34].

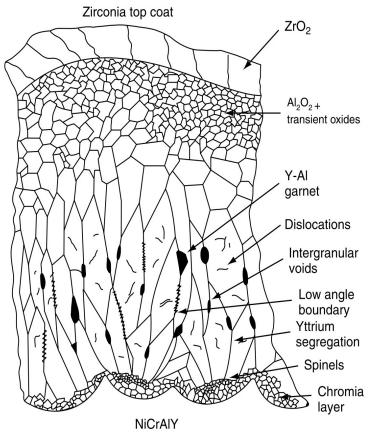

temperature and its operating temperature, low thermal conductivity, chemical inertness, thermal expansion match with the metallic substrate, good adherence, and low sintering rate of the porous microstructure [5, 24]. For that reason, materials such as 7YSZ (ZrO_2 with 7-8$\%$wt.of Y_2O_3), Mullite ($3Al_2O_3.2SiO_2$), Alumina (Al_2O_3), Ceria-Yttria Stabilized Zirconia (CYSZ), and $La_2Zr_2O_7$ are considered for a topcoat materials. The advantages and disadvantages of other TBC materials are compared with the 7YSZ and listed in table 3.3. However, the current technology is based essentially on the thermal barrier material, 7YSZ. Nowadays, the current technology is based on 7YSZ due to its durability over performance. Higher Y contents offer improved insulating potential, but 7YSZ showed superior cyclic life in early tests and continues to prevail over novel materials based on similar criteria and its established processability by both APS and EB-PVD [41].

Table 3.3: TBC materials and their characteristics [24].

Material	Advantages	Disadvantages
YSZ	High thermal expansion coefficient (α=10.7x10^{-6} K^{-1} (293–1273 K)), Low thermal conductivity ($\sim$2.3 W.m^{-1}.K^{-1} at 1273 K [5]), High thermal shock resistance	Sintering above 1473 $^{\circ}$K, phase transformation (1443 K), Corrosion, Oxygen-transparent
Mullite	High corrosion-resistance, Low thermal conductivity (3.3 W.m^{-1}.K^{-1} at 1400 K), Good thermal-shock resistance below 1273 K, Not oxygen-transparent	Crystallization (1023-1273°K), Very low thermal expansion coefficient (α=5.3x10^{-6}K^{-1} (293–1273 K)
Alumina	High corrosion-resistance, High hardness, Not oxygen-transparent	Phase transformation (1273 K), High thermal conductivity, Relatively low thermal expansion coefficient (α=9.6x10^{-6}K^{-1} (293–1273 K)
CYSZ	High thermal expansion coefficient, Low thermal conductivity, High corrosion-resistance, Less phase transformation between monoclinic and tetragonal phase than YSZ, High thermal-shock resistance	Increased sintering rate, CeO_2 precipitation ($>$1373 K), CeO_2 loss during spraying
$La_2Zr_2O_7$	Very high thermal stability, Low thermal conductivity (1.56 W.m^{-1}.K^{-1} at 1273 K), Low sintering, Not oxygen-transparent	Relatively low thermal expansion coefficient (α=9.1x10^{-6}K^{-1} (293–1273 K)

3.3 Yttria Stabilized Zirconia (YSZ)

Zirconia is a crystalline dioxide of zirconium that exhibits mechanical properties similar to those of metals, and its color is similar to tooth color. In 1975, Garvie proposed a model to rationalize the good mechanical properties of zirconia, by virtue of which it has been called "ceramic steel" [42]. Pure zirconia undergoes a polymorphic phase transformation during heating and cooling, these are evident from the phase diagram of figure 3.12a such as melting point at 2690 °C, cubic (*F*) to tetragonal (*t*) phase change at 2370 °C, and tetragonal (*t*) to monoclinic (*m*) phase change at 1170°C.

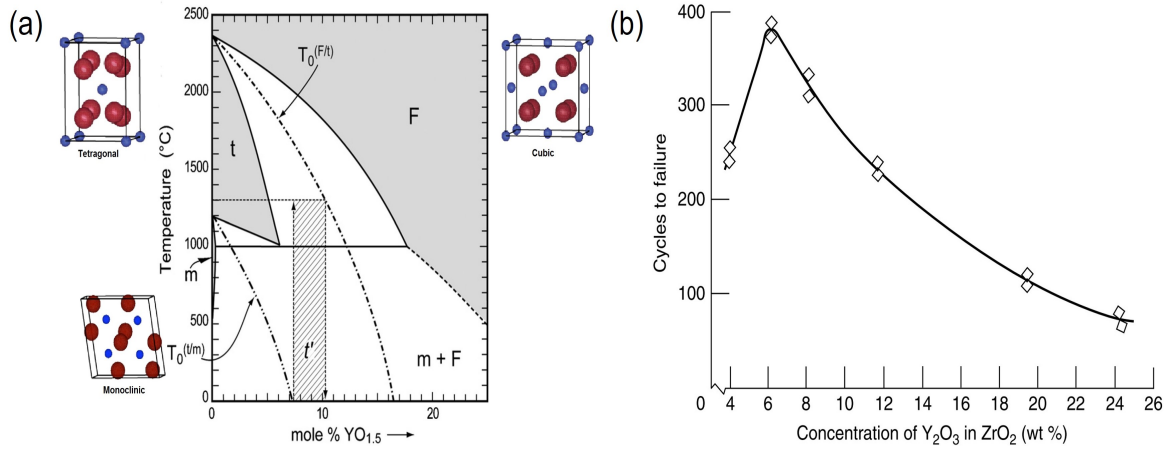

Figure 3.12: Changes produced by yttria content (a) ZrO_2–$YO_{1.5}$ phase diagram [43], (b) TBC composition selection based on durability [34].

The tetragonal (*t*) to monoclinic (*m*) phase transformation is martensitic in nature because it does not require diffusion and occurs by small displacements of atoms in the structure, this transformation occurs on cooling zirconia from high temperature and involves a 3 to 5% volume expansion. This change induces a significant shear strain as high as 10% in the structure, affecting the integrity of any application. For that reason, combining zirconia with other oxides such as CaO, MgO, Y_2O_3, CeO_2, Sc_2O_3, and In_2O_3 inhibits the phase transformation, stabilizes the high temperature tetragonal phase, and eliminates the volume change. Among the stabilizers, the most widely used is yttria, because of the long term stability of the resulting material. Phase diagram (figure 3.12a) accommodates the formation of such non-equilibrium structures by introducing three discontinuous horizontal lines designated by *m*, *t'*, and *F* in the plot.

When YSZ has less than about 4 wt. $\%$ yttria, cooling from high-temperature results in phase transformation from *t* to *m*, which is deleterious for the integrity of the TBCs. With yttria content ranging between 4 and 10 wt. $\%$, the phase formed is *t'*, called non-transformable tetragonal, which remains stable on cooling without the formation of the *m* phase. For an yttrium level greater than 10 wt.$\%$, the low-temperature phase is cubic *F*; this phase generally lacks the strength and durability characteristic of the *t'* phase [34]. For that reason, 7-8 wt. $\%$ of yttria (7-8 YSZ) is the most widely studied and used TC material because it provides the best performance at high-temperature applications such as diesel engines and gas turbines; despite the discovery of lower thermal conductivity options, YSZ remains the material

of choice because its low, temperature-invariant, thermal conductivity; major durability to cycle tests, and high toughness [24, 43]. Figure 3.12b shows the YSZ high-temperature rig test durability as a function of yttria level. Significantly lower yttria contents do not inhibit the transformation to monoclinic phase, while higher levels stabilize a cubic phase which lacks adequate strength and toughness.

There are two main methods for the deposition of YSZ-TC, by Atmospheric Plasma Spray (APS) and Electron Beam Physical Vapor Deposition (EB-PVD) techniques (Microstructures are showed in figure 3.7 a and b). In the EB-PVD technique, the coating growing laterally and in thickness to form individual columns, this offers the advantage of a superior strain, erosion, and thermal shock tolerant behavior than APS coatings. Nevertheless, these merits are gained at the expense of rather high thermal conductivity and low production cost [8]. The table 3.4 compared the properties of both methods at room temperature.

Table 3.4: Properties of YSZ-TBCs at room temperature [8].

Property/Characteristic	EB-PVD	APS
Thermal conductivity ($Wm^{-1}K^{-1}$)	1.5-1.9	0.8-1.1
Surface Roughness (mm)	1	10
Adhesive strength (MPa)	400	20-40
Young's modulus (GPa)	90	200
Erosion rate (normalized to PVD)	1	7
Growth rate (μm/h)	200-300	10000
Production cost	High	Low

3.4 Ceria-Yttria Stabilized Zirconia (CYSZ)

As mentioned in the previous section, some rare earth oxides can be added to zirconia to stabilize its tetragonal and cubic phases, providing high-temperature phase stability, giving that CeO_2 is one of the principal candidates to replace Yttria to stabilize zirconia phases [44]. CYSZ coatings have demonstrated higher phase stability, thermal shock resistance, fracture toughness, hot corrosion resistance, and thermal insulation than YSZ coatings [24, 44, 45]. The properties are listed in table 3.3, and figure 3.13 shows the phase diagram of ZrO_2-CeO_2 system.

The phase diagram shows that CeO_2 provides partial stabilization of the tetragonal ZrO_2 phase over a wide range of compositions. Also, the large ratio of cerium ionic radius to zirconium ionic radius might retard the cation diffusivity. Therefore, the substitution of Zr^{+4} by Ce^{+4} decreases the tetragonality (c/a ratio) and, thus, stabilizes the tetragonal phase to room temperature by decreasing the martensite start (Ms) temperature [47]. However, plasma-sprayed ZrO_2 stabilized CeO_2 coatings present a Ce valence reduction (Ce^{+4} to Ce^{+3}) due to a reducing environment of hydrogen of the plasma jet, and a rapid cooling rate after spray process [47, 48], this change improves the insulation behavior but reduces tetragonal stability [24,49]. The reason to co-doped Y_2O_3 the ZrO_2-CeO_2 system is to counteract the effect of the change in the oxidation state of Ce, Y_2O_3 co-stabilizes ZrO_2 through the substitution of the Zr^{+4} by the Y^{+3}, producing oxygen vacancies and their ionic radius misfit between them reduces the tetragonality, contributing stabilize the high-temperature

Figure 3.13: ZrO_2–CeO_2 phase diagram [46].

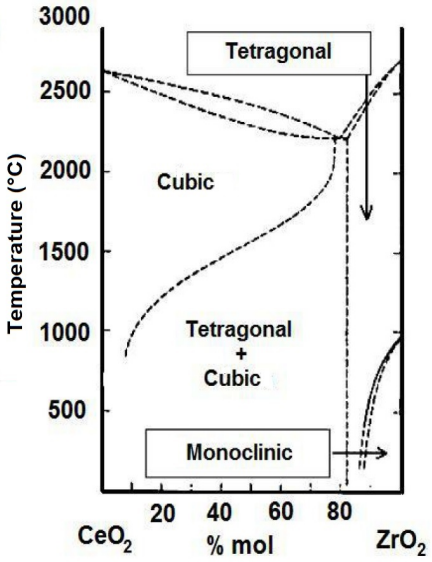

phase. On the other hand, the larger grain size is required to facilitate the tetragonal-to-monoclinic martensitic phase transformation, Y_2O_3 reduces the grain growth rate, slowing the martensitic phase transformation [47].

3.5 Failure mechanism of TBCs

During engine operation, several interrelated thermal cycle-dependent phenomena take place. The wide variation of engine operating conditions is one of the reasons why TBC failure are not entirely understood [32]. However, the main mechanisms have been identified, and they can be classified into Mechanical, Thermo-Mechanical and Thermo-chemical, as is shown in figure 3.14.

Figure 3.14: Failure mechanism of TBCs.

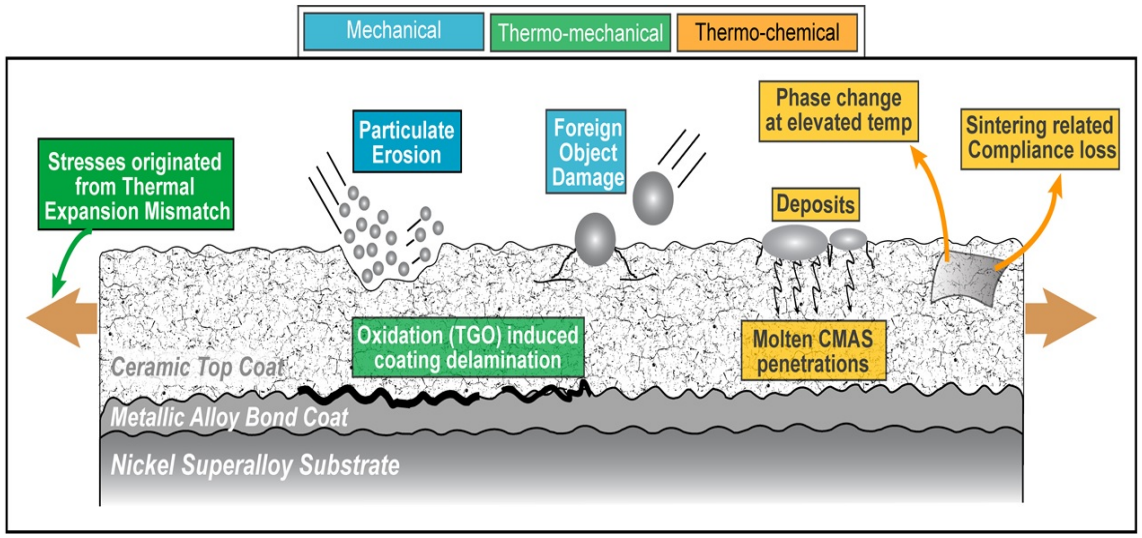

Mechanical failures are extrinsic failures caused by particle impact (erosion and foreign object damage) in the gas turbine environment leading to top layer thinning, densification, cracking, and complete loss/spallation. The damage is assumed to be primarily dependent on the microstructure and properties of the topcoat; moreover, the TBC/TGO and TGO/BC interface properties also play a significant role [32, 43].

Thermo-mechanical is an intrinsic failure, and it is associated to bond coat oxidation and coefficient of thermal expansion (CTE) mismatch between the substrate, bond coat, TGO and, top coat. The oxidation of the bond coat results in the formation and growth of the TGO (where generally the critical thickness is $\sim 6\mu$m), when it thickens with the time at operating temperature resulting in a constrained volume expansion that leads to in-plane compressive growth stress. Additionally, upon cooling, the thermal expansion mismatch with the substrate leads to very high thermal compressive residual stresses in the TGO reaching about 3-6 GPa at ambient temperature. During thermal cycling, TGO seeks to relieve compression, by means of plane displacements, preferentially into the bond coat since it is relatively soft at high temperature, and prone to creep deformation. The continuous repetitions of thermal cycling, and surface imperfections produces roughening (ratchening, rumpling or buckling; see in figure 3.15) of the BC/TGO/TC interfaces due to cyclic creep on the bond coat, once the store energies at the interfaces exceed a threshold value (typically, $U_{TBC}\approx$45 J/m^2 for a TBC thickness of 150 μm), cracks and separation occurs.

Figure 3.15: TGO ratchening during operation at thermal cycles [50].

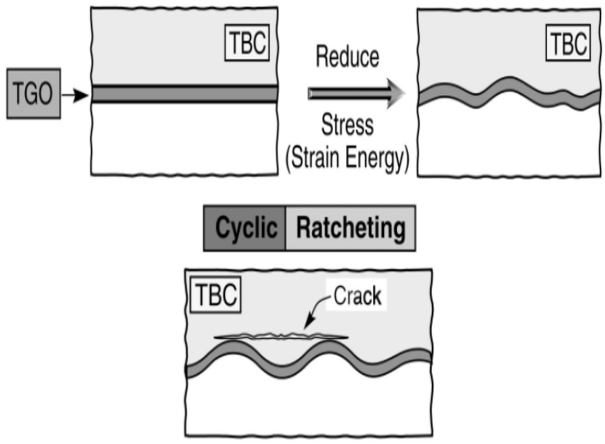

Moreover, TGO growth and interdiffusion between the bond coat and the substrate results in the depletion of Al reservoir in the bond coat, this depletion can promote the formation of other oxides, such as Ni containing spinels, that accelerates localized oxidation by providing oxygen diffusion paths; moreover, Al depletion leads to phase transformations such as β to γ' and/or martensite formation (for a β NiAlPt bond coat). Thus, thermal cycling combined with TGO stresses, strain misfit (due to thermal expansion, and phase transformation), bond coat creep deformation, and initial imperfections lead to TBC failure [32, 43].

Thermo-chemical failures involve intrinsic failures as phase transformations and sintering, and extrinsic failures as the deposition of molten deposits such as CMAS (Calcium-Magnesium-Aluminum-Silicates) and contaminants from the fuel as Na_2SO_4 and V_2O_5.

Phase transformation is an important failure when metastable tetragonal of YSZ decomposes into cubic and monoclinic. This mechanism is caused by the diffusion of yttrium and zirconium forming domains with a cubic structure as well as yttria-depleted tetragonal domains. At some point in the decomposition process, part of the coating can become sufficiently depleted in yttrium to alloy the martensitic tetragonal-monoclinic transition upon cooling, leading a volume change ($\sim 4\%$) of the coating, generating cracks, and then failure [51].

The sintering process in a TBC by APS involves in microcracks healing and changes on pore shape; this modifies mechanical and thermophysical properties of TBC. In particular, the microhardness and the elastic modulus increase with sintering, reducing the strain compliance, and significantly increases the thermal conductivity of TBC, and thus reduce their lifetime. Also, the healing of microcracks, as well as the formation of bridges between splats, promote chemical bondings; however, the drawback of the formation of these bondings is that a crack is allowed to propagate through different grains without being deflected [52].

CMAS damage is generated when particulates of the environment such as sands and dust ingress into the engine, this has a characteristic yellow color associated with transition elements (such as Fe and Mn), in the deposits. The mechanism operates in the presence of a thermal gradient that plays a dual role. (a) It enables the CMAS (once molten) to penetrate to a specified depth into the oxide, (b) it causes the surface to experience residual tensile stress upon cooling. In turn, these stresses provide the energy release rate, that enables internal delamination [43]. In the case of Na_2SO_4 and V_2O_5 fuel contaminants, the mechanism will be discussed in the next section.

3.6 Hot corrosion- HC

Hot corrosion (HC) refers to the interaction between a metal-oxide and a molten salt deposit at solid-gas interface, the salt acts as solvents, preventing the formation of a stable oxide, or they chemically react with the oxide layer. Molten salts are extremely corrosive and their presence increases the rate of corrosion by two orders when compared to high temperature corrosion at similar temperatures and conditions [53]. This type of damage became an important topic in the late 60s as gas turbine engines of military aircraft suffered severe corrosion during the Vietnam conflict during operation over seawater. Metallographic inspection of failed parts often showed sulfides of nickel and chromium, so the mechanism was initially called "sulfidation". However, studies showed that the sulfide formation indeed resulted from the reaction of the metallic substrate with a thin film of fused salt of sodium sulfate base. The name "hot corrosion" is attributed because the corrosion by a thin electrolyte film bears some common features with "atmospheric corrosion" by an aqueous film at room temperature [54].

Additional to sodium sulfate, have been identified another type of salts that produce hot corrosion in different engineering components exposed at high temperature.

- **Halides:** Attack via molten halides is encountered in reactors or pieces of industrial equipment that contains traces of NaCl, KCl, and $BaCl_2$, or other halide salts and operate at temperatures high enough to melt the salts.
- **Sulfates:** Hot corrosion induced by molten sulfates such as (Li, Na, K)SO_4 is extremely corrosive to stainless steels and lower alloy steels. This type of corrosion is

commonly encountered on the fireside of boilers that run on conventional fossil fuels.

- **Carbonates:** Molten carbonates have been receiving attention due to the development of the molten carbonate fuel cell that uses CO_2 as a reactant, it easily reacts with salts and other impurities to form highly corrosive products [53].

The degradation sequence of hot corrosion

Once an alloy surface has been partially or completely wetted by a molten salt deposit, conditions of severe corrosion may develop. Generally, the hot corrosion of all susceptible alloys is observed to occur in two stages:

Initiation stage: During this stage, the alloy and the deposit are being altered to make the alloy susceptible to rapid attack, this alteration may include:

- Depletion of the element responsible for forming the protective scale on the alloy.
- Incorporation of a component from the deposit (e.g. sulfur) into the alloy.
- Dissolution of oxides into the salt.
- Development of cracks or channels through the oxide film and alloy [55].

For example, in the case for Na_2SO_4 melt, elements in the alloy are oxidized, and electrons are transferred from metallic atoms to reducible species in the deposit. Initially the reducible species is oxygen which comes from the Na_2SO_4 and the gas environment (figure 3.16); consequently, the reaction product barrier that forms beneath the deposit on the alloy surface often exhibits features similar to those for the gas-alloy reaction in the absence of the deposit. Nevertheless, there are differences because sulfur also enters the alloy from the deposit. As a result of such reactions with the alloy, the Na_2SO_4 begins to change in composition; therefore, the deposit can become more basic or more acidic compared to its initial condition. These changes in the composition of the deposit begin to affect the reaction-product barrier. This barrier can be compromised whereby the liquid deposit has access to the alloy, and the degradation process proceeds to the propagation stage.

Figure 3.16: Schematic diagram illustrating oxygen consumption by the alloy during the initiation stage of hot corrosion [55].

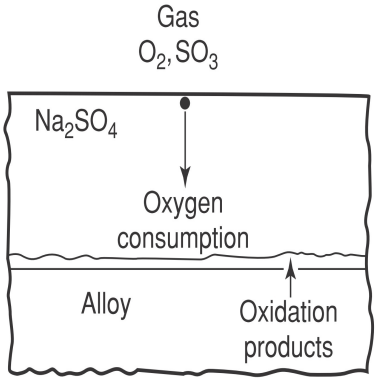

In discussing the composition of Na_2SO_4 (melting point in air, 884 °C), as evident in the figure 3.17, the composition of the Na_2SO_4 at a given temperature is fixed by the oxygen

partial pressure, and by either activity of Na_2O in the melt, a_{Na_2O}, or the SO_3 partial pressure, following the equation 3.1,

$$Na_2SO_4 = SO_3 + Na_2O \tag{3.1}$$

the product $a_{Na_2O}.p_{SO_3}$ is equal to a constant (K1) at a fixed temperature.

Figure 3.17: A thermodynamic stability diagram for the Na–O–S system at a constant temperature in which some possible composition changes of the Na_2SO_4 phase [55].

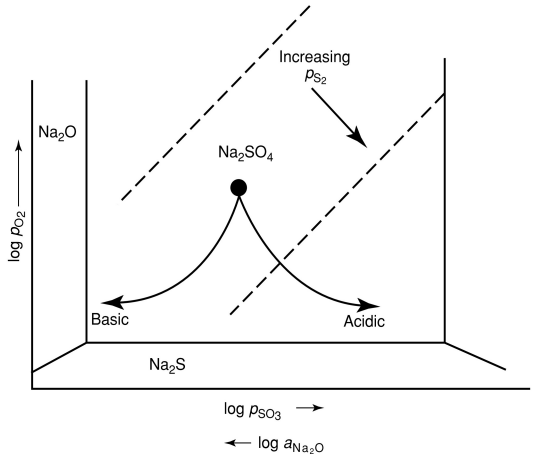

When Na_2SO_4 is in equilibrium with pure Na_2O (the Na_2O-Na_2SO_4 boundary in figure 3.17), a_{Na_2O} can be taken as 1, and $(p_{SO_3})_{eq}$ can be determined. As the SO_3 partial pressure in equilibrium with the melt is increased beyond $(p_{SO_3})_{eq}$, a_{Na_2O} decreases, and the melt becomes less basic. The length of the initiation stage varies from seconds to thousands of hours and depends on a large number of variables including alloy composition and microstructure, deposit composition and thickness, gas composition and flow rate, temperature, and the presence or absence of erosive condition [55].

Propagation stage: Hot corrosion has different propagations modes, and are determined by the mechanisms by which the molten deposits cause the protectiveness of the reaction product-oxide scales to be destroyed. Two possible propagation modes are basic and acidic fluxing of a protective oxide scale. Basic fluxing occurs because oxide ions in the melt react with the oxide to form soluble species, and acidic fluxing involves the dissolution of the oxide by donating its oxide ions to te melt. In discussing the fluxing process, the variation of solubilities of oxides as a function of thickness across the salt is crucial. Rapp and Goto have proposed for continued hot corrosion of a pure metal that the gradient of solubility of the protective oxide (C_{oxide}) in the salt film is negative at the oxide- salt interface, this is shown in figure 3.18.

This condition allows the oxide to dissolve at the oxide-salt interface (x=0) and precipitate out in the salt as discontinuous particles (x>0). When this solubility gradient is positive, the salt becomes saturated with oxide and protective oxide will eventually form al the metal surface. Three specific examples which satisfy the negative solubility gradient condition are illustrated in the figure 3.19a.

Figure 3.18: Re-precipitation of porous MO oxide supported by a negative solubility gradient in the fused salt film [54].

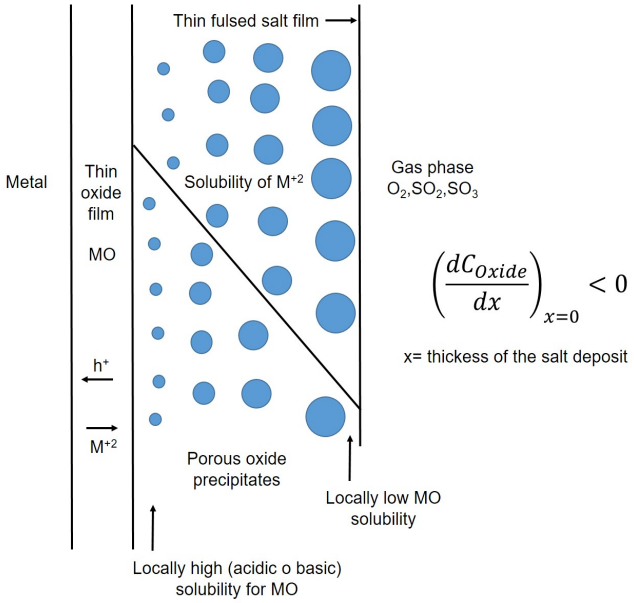

$$\left(\frac{dC_{Oxide}}{dx}\right)_{x=0} < 0$$

In case A, continuing basic fluxing and reprecipitation is favored because a dominant basic solute has a higher solubility at the oxide/salt interface than at the salt/gas interface. In case C, a dominant acidic solute has a higher solubility at the oxide/salt interface than the salt/gas interface. In case B, a negative solubility gradient is realized whenever the local conditions and the corresponding solubilities straddle a minimum. In each case, the protective oxide is favored to dissolve at the oxide/salt interface and precipitate as a non-protective particles within the film [54].

Figure 3.19: Solubilities diagrams, (a) causes of sustained hot corrosion of a pure metal, (b) measured oxide solubilities in fused Na_2SO_4 at 927°C (1200 K) and 1 atm O_2 [54, 55].

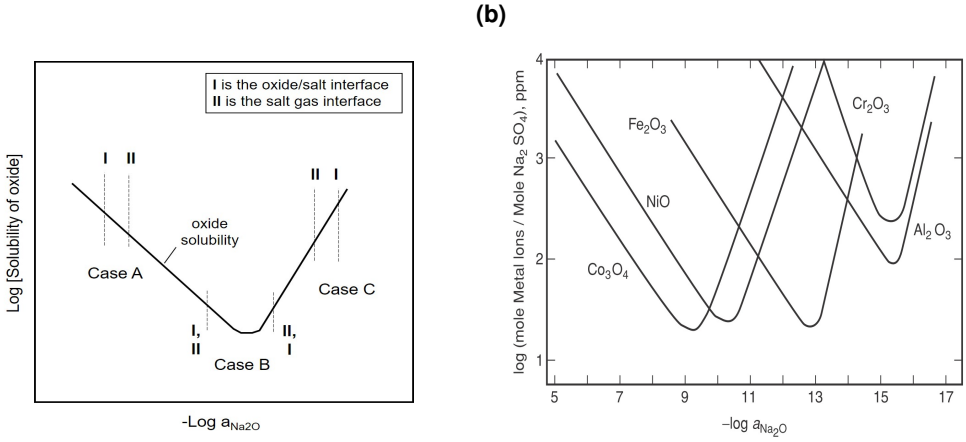

Figure 3.19b shows the solubility curves for a number of oxides in Na_2SO_4 as a function of Na_2O in the melt. Inspection os these curves shows that the solubility of most oxides in molten Na_2SO_4 is a function of the activity of Na_2O in the Na_2SO_4 (or the SO_3 pressure),

and dissolution may occur via basic or acidic reactions. For example, considering NiO, equivalent fluxing reactions in equations 3.2-3.4, where the ion in solution is assumed to be NiO_2^{-2}.

$$NiO + Na_2O = 2Na^+ + NiO_2^{-2}; \tag{3.2}$$

$$NiO + O^{-2} = NiO_2^{-2}; \tag{3.3}$$

$$NiO + Na_2SO_4 = 2Na^+ + NiO_2^{-2} + SO_3; \tag{3.4}$$

whereas equivalent acidic fluxing reactions for NiO with Ni^{+2} ions in solutions are given in equations 3.5 -3.7.

$$NiO + SO_3 = Ni^{+2} + SO_4^{-2}; \tag{3.5}$$

$$NiO = Ni^{+2} + O^{-2}; \tag{3.6}$$

$$NiO + Na_2SO_4 = Ni^{+2} + SO_4^{-2} + Na_2O \tag{3.7}$$

The NiO dissolves by either accepting oxide ions (basic) or by donating oxide ions (acidic). Surface tension effects play a significant role in determining the distribution of the salt. It is reasonable to consider the salt deposit as a continuous layer on the surface of the metal or alloy during the initiation stage of hot corrosion, but as the propagation stage becomes dominant the salt is more likely to be distributed in the pores of the non-protective oxide and consequently the attack may not be uniform over all of the specimen's surface.

3.7 Hot corrosion on Thermal Barrier Coatings

Zirconia Stabilized Yttria (YSZ) has been used as a thermal barrier to increase the operating temperature on gas turbine components. For that reason, the material is exposed to oxides and sulfates that represent the impurities and additives present in gas turbine fuels or impurities in the turbine combustion air as well as the elements of the substrate alloys in contact with zirconia [10]. I. Zaplatynsky in 1978 [56] classified the elements into four groups:

1. Compounds which did not react with zirconia: Na_2SO_4, K_2SO_4, Cr_2O_3, Al_2O_3, and NiO.
2. Compounds that reacted completely with both zirconia phases: CaO, BaO and $BaSO_4$
3. Compounds that reacted preferentially with monoclinic zirconia: Na_2O, K_2O, CoO, Fe_2O_3, MgO, SiO_2, and ZnO
4. Compounds that reacted preferentially with cubic zirconia: V_2O_5, P_2O_5.

Authors such as McKee [57], Nagelberg [58], Rapp [23, 59], and others [60–62] identified that Na_2SO_4 and V_2O_5 are the most aggressive components that produce damage in YSZ, and their origin is the low-grade fuels used for combustion in gas turbines. The vanadium source is the combustion of the fuel, this is oxidized in the combustion chamber and carried

as solid V_2O_4 particles which are deposited on the turbine hardware (e.g., blades). The solid V_2O_4 particles are subsequently oxidized on hardware surfaces to form V_2O_5 with the low melting temperature of 691°C (964 K). When the Na_2SO_4 is also present in the deposit, eutectic solutions can be formed with melting points below 700°C (973 K), as shown in the figure 3.20. One of the reactions was presented in the previous chapter (equation 3.1), showing the formation of Na_2SO_4 by the combustion of fuel. The reaction of Na_2SO_4 and Na_2O with V_2O_5 are shown in equations 3.8 and 3.9 respectively [12, 58, 60].

Figure 3.20: Equilibrium phase diagram of the V_2O_5– Na_2SO_4 system [63, 64].

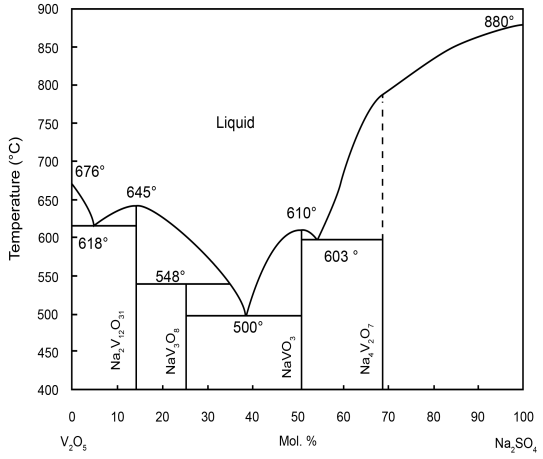

$$Na_2SO_4(l) + V_2O_5(l) = 2NaVO_3(l) + SO_3(g) \tag{3.8}$$

$$Na_2O(l) + V_2O_5(l) = 2NaVO_3(l) \tag{3.9}$$

These solutions combined are highly corrosive and destroy protective oxides.

Initially, the corrosive fused salts can penetrate the entire thickness of YSZ coating through splat boundaries and other coating defects such as micro-cracks and open pores during hot corrosion, then the attack by molten salts can be categorized into two different modes:

1. Chemical reaction: Na_2SO_4 and V_2O_5 molten salts react with the Y_2O_3, generating a depletion of the stabilizer and HC products. These types of reactions with vanadium compounds and ceramic oxides follow a Lewis acid-base mechanism, wherein this case, an acid salt (V_2O_5 and/or $NaVO_3$) react more readily with a ceramic that has stronger basicity (Y_2O_3) [10, 12, 59]. The depletion mechanism is the YSZ in contact with the molten salt dissolves in it, followed by precipitation of YVO_4 and m-ZrO_2 according to with reactions 3.10 and 3.11 [9].

$$t' - ZrO2(Y_2O_3)(s) + 2NaVO_3(l) = 2YVO_4(s) + m - ZrO_2(s) + Na_2O(l) \tag{3.10}$$

$$t' - ZrO_2(Y_2O_3)(s) + V_2O_5(l) = 2YVO_4(s) + m - ZrO_2(s) \tag{3.11}$$

2. Corrosion of the bond coat: In some cases, the molten salts can penetrate the YSZ layer to corroding the bond coat and cause the TBC failure. Figure 3.21 shows the penetration of molten salts through the entire thickness of YSZ layer [10, 65].

Figure 3.21: Salt penetration on YSZ coatings exposed on hot corrosion test, (a) formation of YVO_4 trough the coating thickness, (b) presence of vanadium in the bond coat [66, 67].

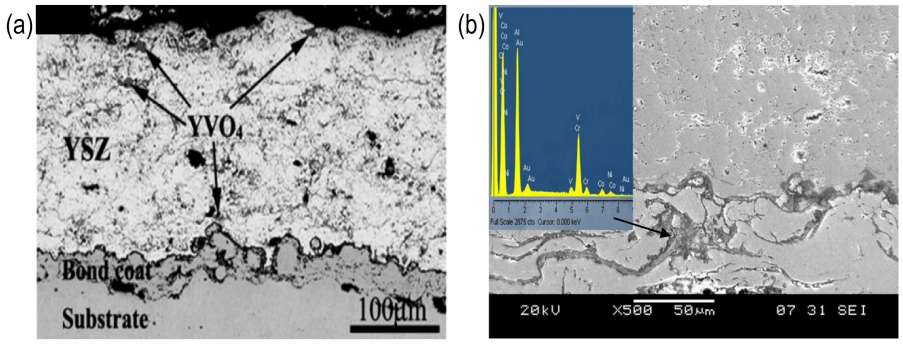

These attacks generate the following types of failure:

1. Phase transformations: The reaction infiltered molten salts with the stabilizer component (Y_2O_3) of the YSZ layer producing a depletion of this stabilizer, followed by tetragonal-to-monoclinic phase transformation [9, 65, 68, 69], changing the topcoat properties such as hardness, stiffness, and thermal conductivity [70].

2. Cracking and physical damage: The phase transformation would lead to the formation of microcracks within the YSZ layer due to 3-5% volume expansion [11, 71]. Moreover, the presence of melt phases and corrosion products (YVO_4 crystals) within the voids, pores, and cracks of the TBC zirconia is likely to reduce the tolerance of the TBC to thermal and physical stress, even if a chemical reaction or extensive sintering does not occur. This case finally leads to the coalescence of microcracks and decomposed the YSZ coating during extended HC test [10, 12, 65]. Figure 3.22 shows the attack and failure of TBC by molten deposits.

Figure 3.22: Illustration of HC process in YSZ layer, (a) penetration corrosive molten salts, (b) depletion of stabilizer (Y_2O_3) in zirconia and followed by the tetragonal-to-monoclinic phase transformation, (c) formation of YVO_4 crystals and microcracks growth, (d) FESEM image of YVO_4 crystals [12].

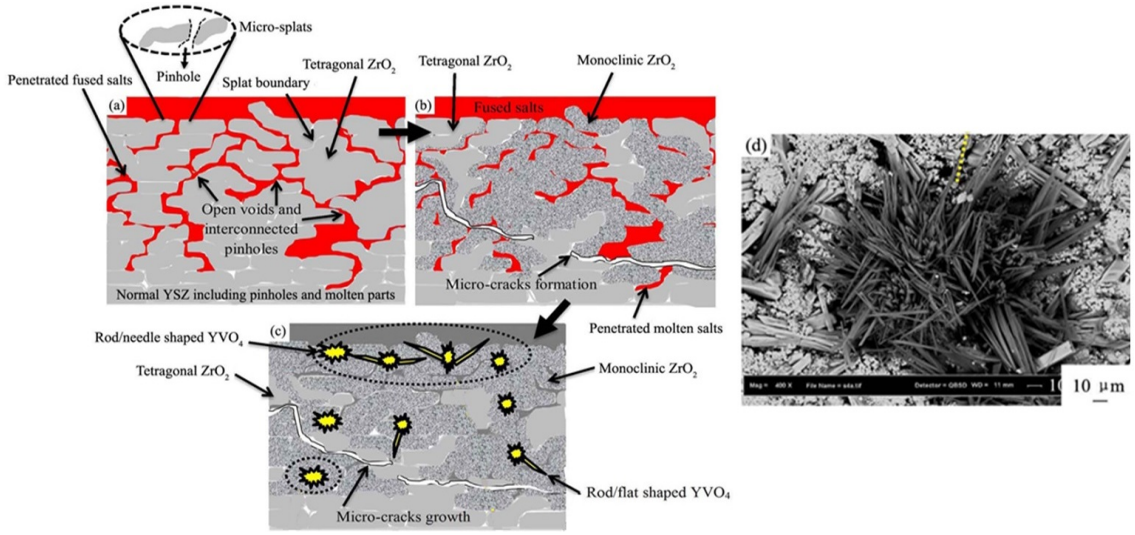

3.8 Methods to increase resistance to Hot corrosion on TBC

3.8.1 Different TBC materials

The use of different insulating materials, YSZ co-stabilizers, and nano-powders have been options of researchers to improve the hot corrosion resistance of TBC systems and increase the operation time of different components exposed to molten salts.

Attempts to **use different insulating materials**, the $A_2B_2O_7$ type rare earths zirconate ceramics as $La_2Zr_2O_7$, $Sm_2Zr_2O_7$ and $Gd_2Zr_2O_7$ have shown to be promising candidates to replace YSZ, because these materials have lower thermal conductivity [7], higher melting points, relatively higher thermal expansion coefficients, and higher phase stability than YSZ [16, 64, 72]. Besides, these materials have shown good resistance to hot corrosion (HC). The HC resistance of $Gd_2Zr_2O_7$ coatings was studied in the work Habibi et al. [16], where compare HC resistance of YSZ, $Gd_2Zr_2O_7$ and $Gd_2Zr_2O_7$+YSZ coatings deposited by APS, against the mixture of Na_2SO_4 and V_2O_5 at 1050°C. Figure 3.23 shows the results of the three systems after HC test.

Figure 3.23: Corrosion resistance of YSZ, $Gd_2Zr_2O_7$+YSZ, $Gd_2Zr_2O_7$ (a) X-Ray diffraction results of as-sprayed coatings after corrosion tests (b) cross-section along the crack of the delaminated YSZ coating [16].

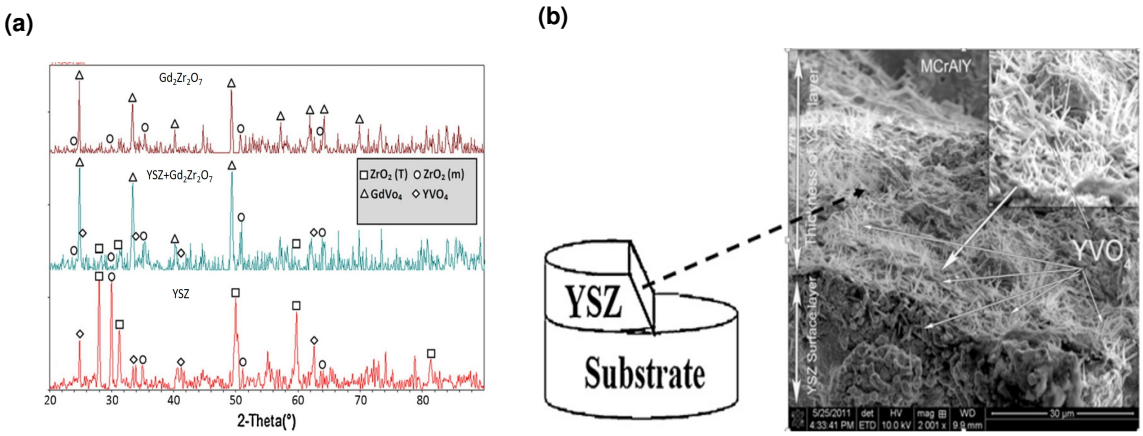

After the corrosion test, most of the tetragonal zirconia in the YSZ sample has changed to the monoclinic phase, and YVO_4 is formed as a corrosion product (figure 3.23a). Moreover, the other two specimens, besides the monoclinic ZrO_2 show the presence of $GdVO_4$. After 20 hours of exposure to hot corrosion at 1050°C, the YSZ coatings showed an extended degradation and spallation started to occur. The infiltration of molten salt into the YSZ coating leads to the formation of dendritic YVO_4 crystals throughout the affected thickness of the coating as is observed in figure 3.23b. The formation of YVO_4 crystals implies the depletion of Y_2O_3 in this region, which leads to the subsequent tetragonal-to-monoclinic ZrO_2 transformation and thus to a large volume changes/stresses within the affected layer. On the other hand, $Gd_2Zr_2O_7$+YSZ composite and $Gd_2Zr_2O_7$ started to degrade after 36 hours of exposure to hot corrosion testing, because Gd_2O_3 have less basicity than Y_2O_3, leading to a low reaction kinetics. Moreover, the presence of fine-grained $Gd_2Zr_2O_7$ around YSZ particles reduces the direct contact of YSZ with molten salt, it react with $Gd_2Zr_2O_7$ producing $GdVO_4$, consuming the salt and thus postpones the formation of YVO_4 crystals

and subsequently less monoclinic ZrO_2 and less YVO_4 crystals were formed. In conclusion, the $Gd_2Zr_2O_7$ and the composite showed a higher HC resistance than YSZ, increasing the degradation time by 40%. A considerable increase in HC resistance was also observed in nano-structured coatings of $Gd_2Zr_2O_7$ [73], where their chemical resistance was combined with the microstructural effect of the nano-zones, these act as a barrier to prevent the penetration of the molten salts through the driver of the TBC.

In order to evaluate other rare earth zirconates, HC test was realized to $La_2Zr_2O_7$ showing a good resistance in V_2O_5 environment and moderate for the Na_2SO_4+V_2O_5 mixture [64]. Moreover, Guo et al. [72] evaluated the HC resistance of $Sm_2Zr_2O_7$ and $(Sm_{0.5}Sc_{0.5})_2Zr_2O_7$ coatings deposited by APS in a mixture of Na_2SO_4 and V_2O_5 at different temperatures, presenting a positive effect in Sc addition to reduce material degradation. Figure 3.24 shows the results after HC test of both materials.

Figure 3.24: Results after hot corrosion test (a) X-Ray diffraction of $Sm_2Zr_2O_7$ and $(Sm_{0.5}Sc_{0.5})_2Zr_2O_7$ at 700, 800 and 900°C, surface morphology after HC test at 800°C of (b) $Sm_2Zr_2O_7$, and (c) $(Sm_{0.5}Sc_{0.5})_2Zr_2O_7$ [72] (*Modified by author*).

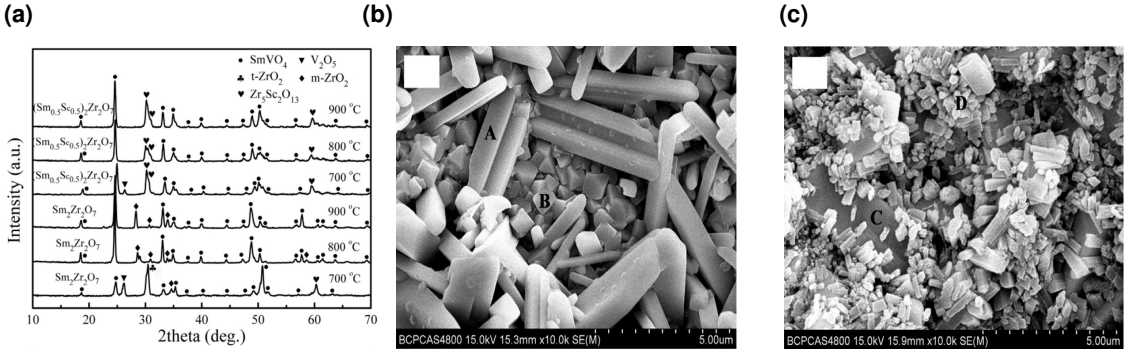

After the corrosion test, well defined peaks from $SmVO_4$ are observed in all test performed (3.24a), presenting the fluxing mechanism of molten salts at different conditions. However, at 700°C V_2O_5 can be observed in both materials, in the case of $Sm_2Zr_2O_7$ indicates that temperature is not high enough, thus some amount of Sm_2O_3 remains in ZrO_2 matrix as a stabilizer. This justifies the presence of ZrO_2 tetragonal and monoclinic phases at this temperature, and above 700°C only the presence of $SmVO_4$ and m-ZrO_2 are observed, where present rod-shaped (A) and bulk-shaped (B) morphologies respectively (figure 3.24b). On the other hand, X-Ray results of the sample $(Sm_{0.5}Sc_{0.5})_2Zr_2O_7$ show high intensity peaks of $SmVO_4$ and $Zr_5Sc_2O_{13}$ for all temperatures, where show rod-shaped (C) and bulk-shaped (D) morphologies respectively, this is observed in figure 3.24c. The molten salt prefers to react with Sm_2O_3 in $(Sm_{0.5}Sc_{0.5})_2Zr_2O_7$ to form $SmVO_4$, leaving Sc_2O_3 in the compound as a stabilizer for ZrO_2, since Sc_2O_3 content in the compound is high, it is reasonable to observe $Zr_5Sc_2O_{13}$, following the reaction:

$$NaVO_3(l) + (Sm_{0.5}Sc_{0.5})_2Zr_2O_7(s) = SmVO_4(s) + Zr_5Sc_2O_{13}(s) + Na_2O(s) \quad (3.12)$$

According to the observed results and making a comparison between the two materials, the presence of m-ZrO_2 after to HC test of $Sm_2Zr_2O_7$ is harmful to the thermal cycling performance of TBC, because during the test m-ZrO_2 undergoes phase transformation accompanied with volume change, resulting in the formation of cracks in the coating. On the other

hand, $Zr_5Sc_2O_{13}$ formed after HC test of $(Sm_{0.5}Sc_{0.5})_2Zr_2O_7$, keeps phase stability during thermal cycling. Therefore, $Zr_5Sc_2O_{13}$ is more desirable than m-ZrO_2 for TBC applications. Hence, $(Sm_{0.5}Sc_{0.5})_2Zr_2O_7$ shows better resistance to Na_2SO_4+V_2O_5 salt corrosion than $Sm_2Zr_2O_7$, and it might be a more promising material for TBC applications.

Using **co-stabilizers** of t'-phase of the zirconia with less basicity than yttria and nano-powders are other methods to increase resistance to molten salt attack. The works of Hajizadeh-Oghaz et al. [74], and Loghman-Estarki et al. [19], combine these procedures to improve the HC resistance of TBC. In the first work, using nano-poeders Ceria-Yttria Stabilized Zirconia (CYSZ) coatings were deposited with APS technique. HC resistance was studied using a salt mixture 45 and 55%wt. of Na_2SO_4 and V_2O_5 respectively at 1000°C during 300 hours. Figure 3.25 shows the X-Ray results at different times, and FE-SEM images after hot corrosion test.

Figure 3.25: Results after hot corrosion test, (a) X-Ray diffraction at 6, 12, 18, 30, 72, 156, and 300 hours, (b) FE-SEM images at 300 hours of corrosion test [74].

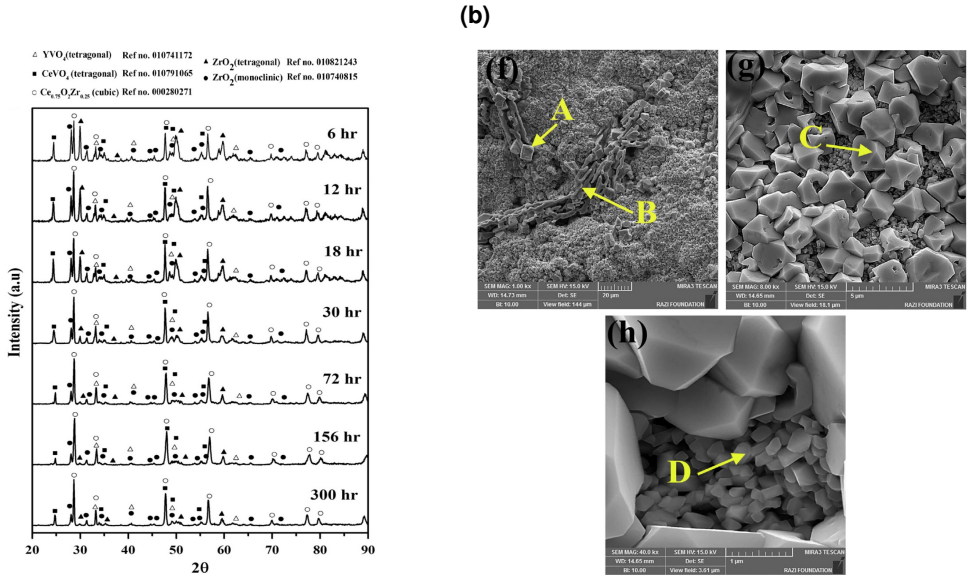

The X-Ray results of the nano-structured CYSZ coatings after corrosion test was found both tetragonal, monoclinic phases of zirconia (up to 72 hours). Furthermore, $Ce_{0.75}O_2Zr_{0.25}$, YVO_4, and $CeVO_4$ formed as HC products on the coating surface during the course of the experiment. FE-SEM images of the top surface of the CYSZ nano-structured coatings show cubic (A), semi-rod-type (B) and semi-cubic crystals (C) could be detected on the coating surface, the elemental analysis on these points show that the cubic (A) and semi-cubic crystals (C) are $Ce_{0.75}O_2Zr_{0.25}$ crystals, (B) is a mixture of rod type of YVO_4 and $CeVO_4$ and (D) is CYSZ.

In this work was determined that nano-structured CYSZ TBCs exhibited superior HC resistance in comparison with that reported for conventional YSZ and CYSZ TBCs. There were two major reasons for this: the first was related to the robust acidity and high content of the stabilizer (Ce_2O_3) in comparison with YSZ, this is also reported by in different publications [10, 22, 23, 59, 60, 75]. The second related to the resulting diffusional resistance in nano-porous CYSZ microstructures, due to the porosity associated with the nano-zones,

offering excellent degradation resistance throughout the hot corrosion investigation, as compared to conventional CYSZ. This result is also presented by Daroonparvar [12], the use of nano-structured YSZ powders generate dense nano-zones into the coating reducing the salt infiltration and oxygen penetration, this increment the hot corrosion resistance and the thickening of TGO to critical values.

The second work [19] studies the corrosion behavior of Scandia-Yttria Stabilized Zirconia (SYSZ) coatings deposited by APS technique. Figure 3.26 shows the X-Ray results after corrosion test into a mixture of 45 and 55% of Na_2SO_4 and V_2O_5 respectively at 910°C during 300 hours.

Figure 3.26: X-Ray diffraction results of the coatings after 6, 12, 18, 30, 100 and 300 hours hot corrosion, (a) full pattern, (b) specific pattern between 27 and 30° [19].

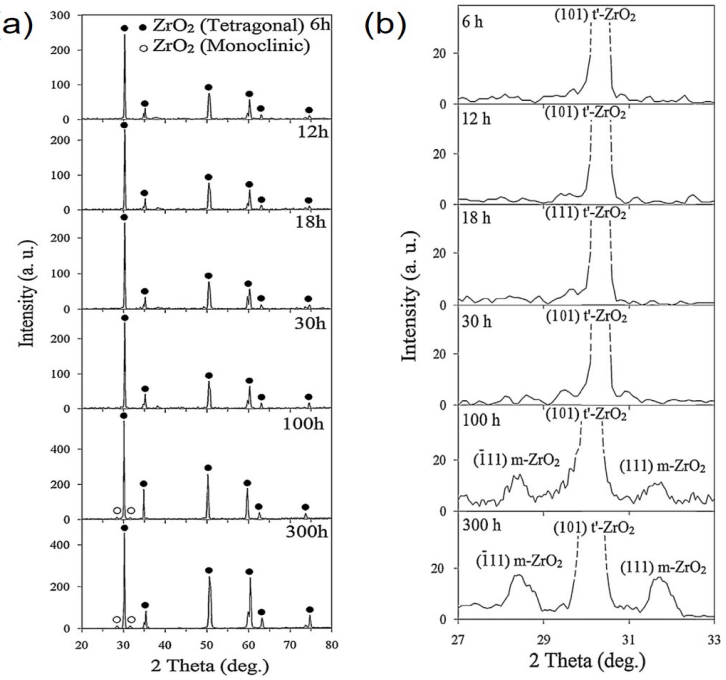

According to these results, upon 30 hours exposure to hot corrosion zirconia was present only in the tetragonal phase, and no destabilization occurred in the coatings. Even after 100 and 300 hours of exposure a little amount of tetragonal phase was transformed to the monoclinic phase. Moreover, no peak corresponding to the hot corrosion products (YVO_4 or $ScVO_4$) is observed after 300 hours of hot corrosion.

In conclusion, change top-coat material with oxides with less basicity that yttria (co-stabilizers) and other insulating materials show as a good methods to increase the hot corrosion resistance of TBC. Moreover, the introduction of coating architectures is other method to improve the HC resistance and thermo-mechanical behavior. The dependence of coating microstructure on thermal cycling resistance is presented in the work of Viswanathan et al. [76], where the top-coats with high toughness achieved through increasing density (reducing microstructural defects) at BC/TC interface show generally improved furnace cycle test durability. On the other hand, the increment in HC resistance using coating architectures is described in the next section.

3.8.2 Coating architectures

Some variations of coatings architecture as a alternative of the standard TBC system (TC/BC/ Ni-base superalloy) to reduce the salt infiltration and oxygen entrance, as spray a second insulating layer, multiple TC layers or a top coat with a bimodal microstructure (porous and dense) were used. These combine with high HC resistant ceramics can be a effective method to increase the resistance against molten salt attack [66, 77–80].

The deposition of a top coat with a controlled porosity can reduce the salt infiltration without increase the thermal conductivity of the ceramic. In the work of Lui et al. [13], APS technique was used to deposit a dual-layered top coat of YSZ composed of a dense layer and a conventional porous layer. The objective of the dense layer is to suppress the infiltration of the molten CMAS into the coating. Figure 3.27 shows the microstructure and elemental distribution of de conventional and dual-layer YSZ TBC after CMAS attack at 1250°C for 20 hours.

Figure 3.27: Coatings microstructures after thermal exposure with CMAS at 1250 °C for 20 hours, (a) conventional porous YSZ, (b) dual-layer YSZ, (c) Si distribution in the coatings [13] (*Modified by author*).

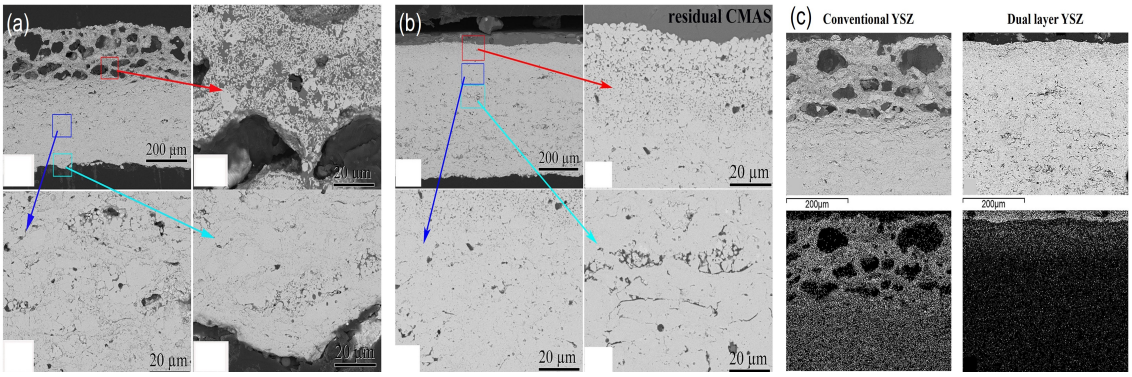

Figure 3.27a shows that molten CMAS has penetrated throughout all the porous coating, and this is divided into two distinct layers. The first is the top layer (red arrow), which exhibits a porous microstructure due to the severe reaction between CMAS and YSZ. Beneath this region, a second layer filled with CMAS (blue and cyan arrows) is observed. In the case of dual-layer YSZ (figure 3.27b), residual CMAS on the surface of the coating after thermal exposure (red arrow) are observed. However, less dissolution of the coating is observed compared with the porous layer (blue and cyan arrows). Silicon (Si) distribution in the EDS of figure 3.27c, high presence of Si across the coating thickness is observed. On the other hand, a fewer Si penetration of CMAS is observed in dual-layer YSZ, due to it was blocked out by the dense layer. Therefore, dense YSZ layer is an effective barrier against HC attack because the reduction of the interconnected porosity in the top coating layer decreases the molten salt infiltration and avoid the retain the dissolution reaction to the surface.

The insertion of a second insulating layer as a molten salt barrier has been an effective method to increase the HC resistance. Materials such as conventional, micro and nano Al_2O_3 [66,81–83] and $Gd_2Zr_2O_7$ [80] have been used as YSZ overlayer due to their excellent mechanical, thermal properties and their high chemical resistance. The work of Keyvani et al. [84] is an example of the effective use of this kind overlayers. Using APS technique to

deposit nano-structured powders of Al_2O_3 over a conventional layer of YSZ. Figure 3.28 shows the microstructure of YSZ and nano-Al_2O_3/YSZ coatings before and after of HC test.

Figure 3.28: Cross-section of the coatings: (a) conventional YSZ coating, (b) nano-structured Al_2O_3/YSZ coating; samples images after HC test: (c), (e) surface and cross-section of conventional YSZ coating; (d), (f) surface and cross-section of Al_2O_3/YSZ coating [84] (*Modified by author*).

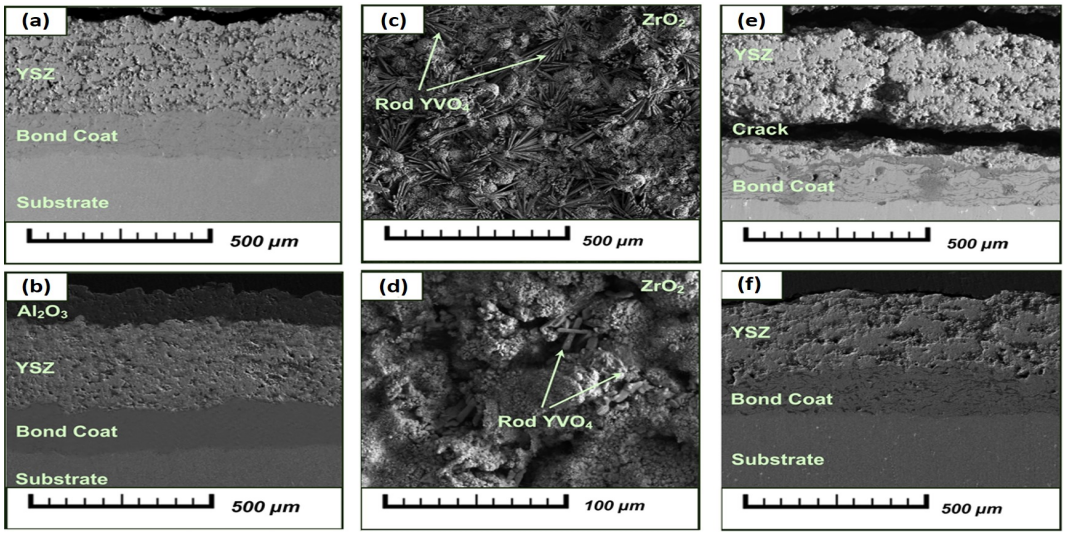

The most important difference in microstructure of conventional YSZ coating and nano-sized Al_2O_3/YSZ composite coating is the size of porosities (Figure 3.28a and 3.28b). In nano-sized Al_2O_3/YSZ the porosities have the same size and are distributed uniformly. However, in conventional coating the porosity have different sizes and a random distribution.

After the HC test, the surface of conventional YSZ coating present ZrO_2 particles and needle type crystals (Rod YVO_4) formed inside the ZrO_2 matrix with length of 50 and 20 μm respectively (3.28c). For Al_2O_3/YSZ system, alumina particles and Rod YVO_4 are also observed. After 16 hours conventional YSZ coating present spallation at BC/TC interface because the difference in physical and mechanical properties of layers (figure 3.28e); on the other hand, spallation occur after 52 hours for Al_2O_3/YSZ system, despite this, the underneath YSZ remained un-attacked (figure 3.28f). Thus, nano-structured Al_2O_3/YSZ system coating is much more resistant to HC than conventional YSZ coating, because the alumina overlay played an important role in decreasing the infiltration of molten materials into zirconia layer.

In conclusion, works Keyvani and Liu show that the coating microstructure and the use of a coating overlay play an important role to improve HC resistance in TBC systems, because if the infiltration of salts through pores and cracks are reduced, then area attacked and the degradation of the coating are lower.

4 | Methodology

4.1 Materials

4.1.1 Substrate

Inconel 625 Nickel-based superalloy was used as a substrate; this alloy exhibits excellent mechanical properties (resistance to creep, rupture and fatigue), and good response against to oxidation, carburization, and hot corrosion at elevated temperatures [85]. 5 millimeter-thick samples were extracted from 1-inch diameter bar. The chemical composition of the bar was measured with Ar Spark OES brand OBLF with a standard of SRM 1245a (Inconel 625), the results are shown in Table 4.1.

Table 4.1: Chemical composition (wt. $\%$) of superalloy bar measured with Ark Spark OES.

Source	Ni	Cr	Mo	Nb	Fe	C	Si	Al	Ti	Mn	Co
Measured	60.7	22.2	8.4	3.38	4.1	0.04	0.19	0.19	0.15	0.18	0.1
Reference [86]	61	21.5	9	3.6	2	0.05	0.2	0.2	0.2	0.2	-

The measured composition agrees with the nominal values reported by INCO ALLOYS INTERNATIONAL in their US patent # 3.160.500 [86]. The difference compared with the patent is the addition of Co, an element used to stabilize the γ phase [35]. The substrate hardness was measured using a Vickers tip and 40 Kgf of load, getting a value of 192 HV. Hu et al. [87] reported a hardness 205 HV for Inconel 625 with a similar composition. Sample metallography is observed in figure 4.1, where the etchant used was 60 ml HCl + 6 g $CuCl_2$ + 3 ml distilled water + 3 ml Ethanol.

Figure 4.1: Microstructure of Inconel 625 alloy. Etching: 60 ml HCl + 6 g CuCl2 + 3 ml distilled water + 3 ml Ethanol. Optical Microscope.

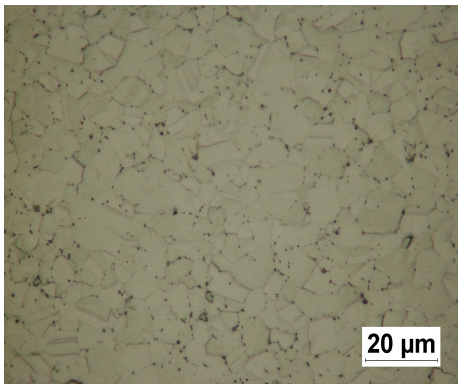

The microstructure of the super alloy shows a matrix composed of γ phase with average grain size 5μm and some twins. The grain boundaries are decorated, presumably with MC and $M_{23}C_6$-type carbides.

4.1.2 Feedstock materials

NiCoCrAlY

Commercial Amdry 386-2.5 NiCoCrAlY powder was used for the bond coat. Figure 4.2a shows the spheroidal morphology of the powder particles with some irregularities characteristic of gas atomized process (satellite particles). Particle size distribution of powder is d(0.1)=28.18 μm, d(0.5)=40.07 μm, and d(0.9)= 56.65μm, which is in agreement with the supplier's specifications (see figure 4.2b).

Figure 4.2: Characterization of Amdry 386-2.5 (a) SEM image, (b) particle size and distribution.

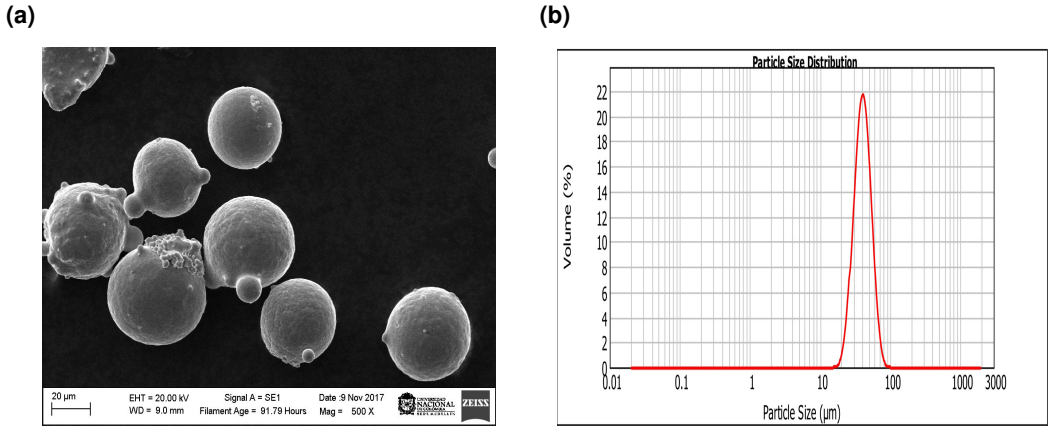

An X-ray diffractogram of the NiCoCrAlY powder is presented in figure 4.3. High-intensity peaks at 2θ = 43.5 and 44.6° that correspond to γ/γ' and β respectively are observed. The first phase is a solid solution of Ni, Co, and Cr, and the second phase is indexed as NiAl [88]. Rietveld adjustment with wRp of 2% shows a major content of β phase with 89.4% and the rest 10.6% correspond to γ/γ'.

Figure 4.3: X-Ray diffractogram and Rietveld adjustment of Amdry 386-2.5.

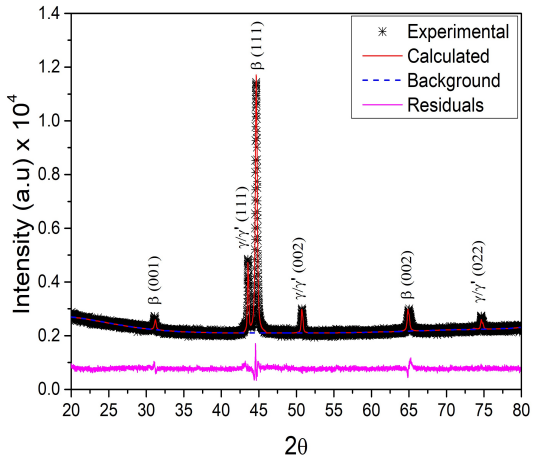

Yttria Stabilized Zirconia (YSZ)

YSZ powder used for the spraying of the coating system was Metco 204NS-G, whose manufacturing method is agglomeration and plasma densification (HOSP). Figure 4.4a shows that the powder particles are composed of smaller particles inside an spherical shell with a distribution of d(0.1)=21.71 μm, d(0.5)=53.31 μm, d(0.9)=94.26 μm, which accomplishes with supplier specifications (see figure 4.4b).

Figure 4.4: Characterization of Metco 204NS-G powder (a) SEM image, and (b) particle size and distribution.

(a) **(b)**

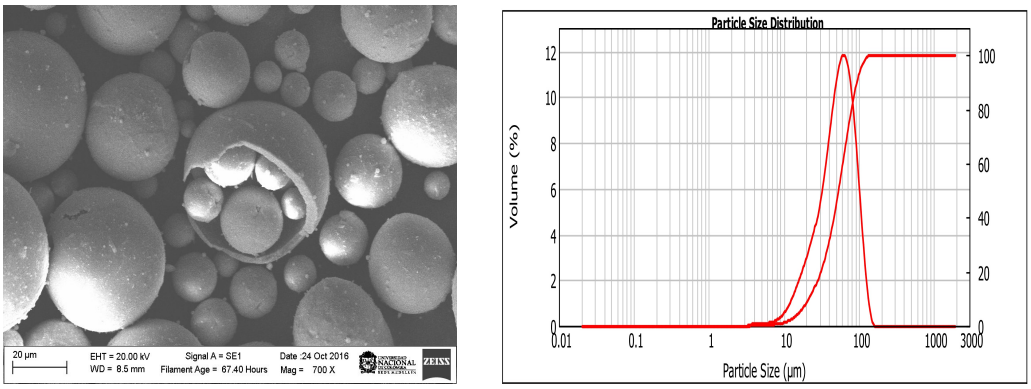

Figure 4.5 shows the structural characterization of YSZ powders, where is observed a high intensity of 2θ =30.1°peak, corresponding to of tetragonal phase of YSZ. Quantification results (wRp = 4.7 %) shows 84.40% of non-transformable tetragonal phase (*t'*) and 4.89% of transformable tetragonal phase (*t*), for a total of 89.29%. The remaining 10.71% corresponds to the monoclinic phase.

Figure 4.5: X-Ray diffraction patter and Rietveld adjustment of Metco 204NS-G.

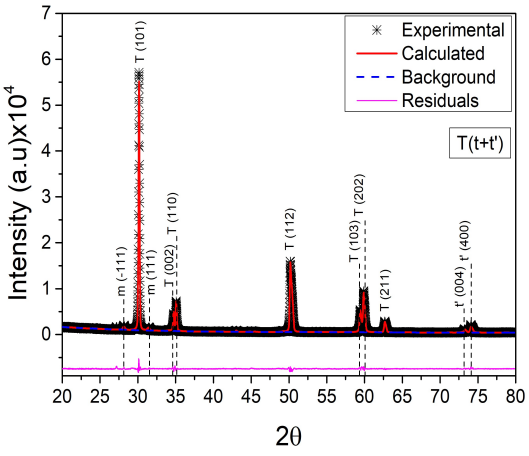

Ceria-Yttria Stabilized Zirconia (CYSZ)

CYSZ powder used for the spraying of the second topcoat was Metco 205NS. Figure 4.6a shows the spherical morphology characteristic powder manufacturing via agglomeration and

HOSP; unlike the 204 NS-G powder, 205 NS is composed by a solid, dense particles instead of small particles inside of larger hollow spheres. Particle size distribution is observed in figure 4.6b where d(0.1)= 24.48 μm, d(0.5)= 46.74μm, and d(0.9)= 82.65 μm, which is in the range of supplier specifications.

Figure 4.6: Characterization of Metco 205NS powder (a) SEM image, and (b) particle size and distribution.

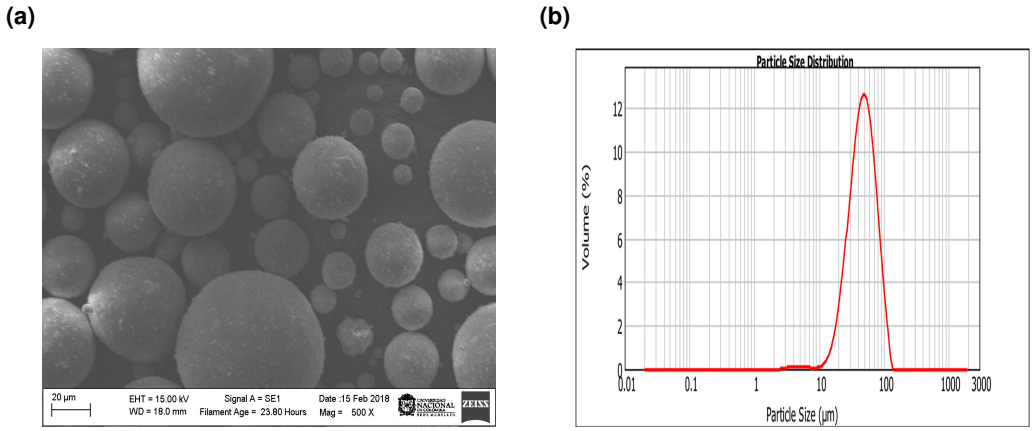

Figure 4.7 shows the X-ray diffractogram of CYSZ powder, where a high intensity of 2θ =29.9°peak of (011) plane, corresponding to CYSZ tetragonal phase (*t'*) can be seen. Characteristic peaks of monoclinic ZrO_2 and cubic CeO_2 phases at 2θ=28.2 for and 28.5° for the planes (-111) and (111) respectively are also observed. Quantification results (wRp = 5.4%) yields 87% of t'-CYSZ, 12% of m-ZrO_2 phase and the remaining 1% corresponding to CeO_2 phase. Results indicate that de powder does not accomplish with data sheet provided by Oerlikon, because it exceeds the maximum quantity of m-ZrO_2 phase (10%) and does not present ZrO_2 cubic phase. However, only the presence of the *t'* phase in CYSZ was reported by Yashima et al. [89, 90], where the mixture between *t'* and cubic phase in the material is present above 65 mol% of CeO_2.

Figure 4.7: X-Ray diffraction patter and Rietveld adjustment of Metco 205NS.

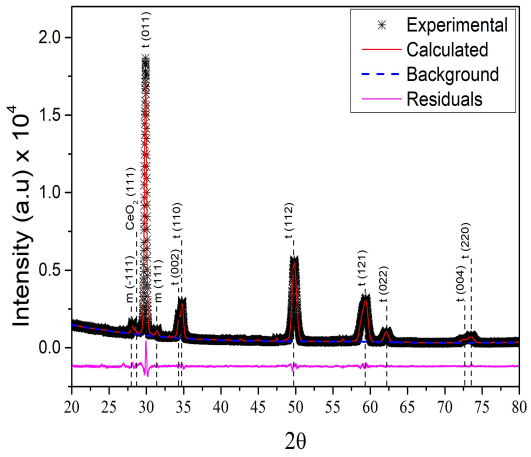

4.2 Coatings deposition

For all coating systems deposited, nickel-based superalloy (Inconel 625) substrates were grit blasted with alumina particles (Corundum F24) obtaining average roughness values of Ra= 4.58$\pm$0.51, Rq= 5.78$\pm$0.73, and Rz= 34.85$\pm$3.43. Subsequently, all the samples were cleaned ultrasonically with isopropyl alcohol during 180 s, and dried with high-pressure air.

4.2.1 Bond Coat

Spray parameters were defined using *AccuraSpray* system in search for a combination that yields the highest particle velocity. The following conditions allowed obtaining particle velocities of 320 m/s, and the coating's microstructure with 13.5$\pm$3.7$\%$ porosity and 4.6$\pm$1.5$\%$ oxide content.

Table 4.2: Spray parameters of bond coat

Parameters	Condition
Current (A)	400
Spray distance (mm)	113
Primary gas- Ar (NLPM)	80
Secondary gas- He (NLPM)	70
Surface speed (mm/seg)	1000
Spray rate (g/min)	25

4.2.2 YSZ topcoat

Due to the importance of obtaining YSZ coatings with suitable characteristics to be used as a thermal barrier, the spray parameters were found varying the current and the hydrogen flow. The particle's temperature and velocity were measured using the *AccuraSpray* system taking as initial point the parameters given by the manufacturer. The constant parameters are listed in table 4.3, the variables used were current and H_2 flow with levels of 400 and 430 Amperes, and 5, 7, 9 NLPM respectively.

Table 4.3: Constant parameters of YSZ spraying

Parameters	Condition
Spray distance (mm)	105
Primary gas- Ar (NLPM)	50
Surface speed (mm/seg)	1000
Spray rate (g/min)	20

Relating the values of temperature and particle velocity with the results of thickness, porosity, crystalline structure, and adhesion (section 5.2.1), it was determined that the best current and H_2 flow for the deposition of YSZ coatings are 430 Amperes and 7 NLPM respectively.

4.2.3 Dense CYSZ (D-CYSZ) topcoat

To obtain low porosity CYSZ coatings, current, spray distance, and H_2 flow was varied to the parameters listed in table 4.4.

Table 4.4: Spray parameters of D-CYSZ

Parameters	Condition
Current (A)	540
Spray distance (mm)	90
Primary gas- Ar (NLPM)	50
Secondary gas- H_2 (NLPM)	5
Surface speed (mm/seg)	1000
Spray rate (g/min)	20

4.2.4 D-CYSZ/YSZ top coat bilayer system

Using the spray parameters of the D-CYSZ (section 4.2.3), YSZ (section 4.2.2), and NiCoCrAlY (section 4.2.1), the D-CYSZ/YSZ bilayers with a total thickness of 300 μm of the topcoat, and 120μm bond coat will be deposited. The dense layer thickness were modified between 0 to 150 μm as shown in figure 4.8.

Figure 4.8: Experimental procedure to spray D-CYSZ/YSZ bilayers.

The use of a low porosity layer of YSZ (high toughness layer) at the TC/BC interface of coating architectures (figure 4.8) aims to increase the thermal fatigue resistance. This fact was demonstrated by V. Viswanathan and S. Sampath [91] in experiments where the thermal fatigue resistance was increased from 450 hours to 1200 hours approximately. The parameters of low porosity YSZ (LP-YSZ) are listed in table 4.5, where the current was increased to reduce the porosity.

After the deposition of each layer of the coatings system described in figure 4.8, the samples were allowed to cool down to ambient temperature; before deposition of the subsequent layers, the pre-deposited coating layers were preheated approximately to 160 °C to ensure good adhesion between the successive layers. The number of passes was calculated to achieve desired layer thicknesses.

Table 4.5: Spray parameters of LP-YSZ topcoat

Parameters	Condition
Current (A)	500
Spray distance (mm)	105
Primary gas- Ar (NLPM)	50
Secondary gas- H_2 (NLPM)	7
Surface speed (mm/seg)	1000
Spray rate (g/min)	20

4.3 Equipment and characterization

4.3.1 Equipment

Spray gun

Spray gun used to spray NiCoCrAY, YSZ and CYSZ coatings was Sinplex Pro of Oerlikon Metco. The gun has a cascading anode design which it can spray with higher efficiency at significantly bigger powder feed rates than traditional single-cathode plasma guns. Figure 4.9 shows the Sinplex pro gun and the efficiency comparison between other spray gun references.

Figure 4.9: (a) Sinplex pro (b) SinplexPro, 9MBM and F4MB-XL throughput comparison (feed rate vs. Deposition efficiency) to achieve similar coatings [92].

(a)

(b)

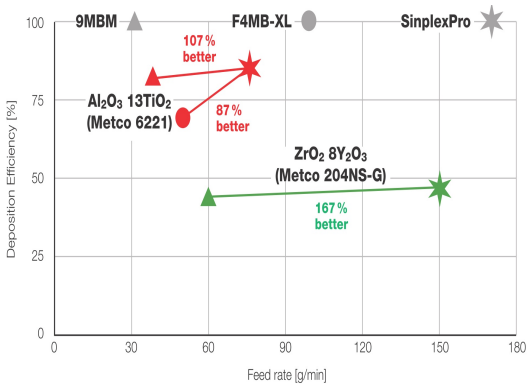

AccuraSpray

The particle temperature and velocity of the projected powder jet were measured with AccuraSpray system of Tecnar for all deposits with a correlation over 95%. This equipment measures particle temperature over 1000°C with a precision of 2.5%, and particle velocity in a range of 5 to 1200 m/s at 0.5 % precision. Figure 4.10 shows equipment position and software interface.

As observed in figure 4.10a, the spray gun was positioned perpendicular to AccuraSpray, and the distance between them was 20cm. The spray distance was adjusted using a laser guide that indicates the location of IR camera and pyrometer of the equipment.

Figure 4.10: AccuraSpray system (a) position during spray and, (b) software interface (*source Author*).

(a) **(b)**

X-ray diffractometer

Structural characterization of all experiments was performed with a Rigaku Smart Lab X-Ray diffractometer (XRD) and X'Pert PANalytical Empyrean serie III – Alpha1 using a Bragg Brentano geometry with Cu-kα radiation (λ=1.5406 Å) between 20° and 80° with steps of 0.01. XRD data identification was performed using PDXL integrated X-ray powder diffraction® and X'Pert HighScore Plus® (Rigaku and PANalytical respectively) softwares with ICDD, COD and ICSD databases. Quantitative Rietveld analysis was achieved with GSAS software using the following Crystallographic Information Files (CIF) for each material:

- YSZ- Tetragonal phase with 8 mol.% YO1.5 (t'-YSZ)- ICDD code: 01-082-1241
- YSZ- Tetragonal phase with 4 mol.% YO1.5 (t-YSZ)- ICDD code: 01-078-1808
- CYSZ- Tetragonal phase (t'-CYSZ) - ICSD code: 98-008-6607
- ZrO_2- Monoclinic phase (m-ZrO_2)- ICDD code: 01-078-0047
- CeO_2 Cubic phase - ICSD code: 98-018-0851
- YVO_4- Tetragonal phase- ICDD code: 01-074-1172
- γ-Ni Cubic phase - COD code: 96-901-3033
- β-AlNi Cubic phase - ICSD code: 98-060-4656

The background was fitted using Chebyschev polynomials with 8 terms, and the peak profiles were fitted using a convolution of a pseudo-Voigt and asymmetry function. In all cases, the data fit was adjusted to wRp values below 7%. The steps followed to make Rietveld adjustment are included in Annex 1.

Microscopes

Optical microscopy and Stereoscope:

Morphological characterization of coatings cross-section was carried out using a Nikon eclipse LV 1000, and the coating's surface after adhesion test was characterized using a

Nikon SMZ 1500 stereoscope; both systems are equipped with digital camera Nikon DS-2Mv. Images was taken with magnifications between 100 to 400x for microscope, and 0.75 and 4x for stereoscope using NIS-Elements software®.

Scanning Electron Microscopy- SEM:

The morphological and chemical characterization of the powders, coatings, and hot corrosion products were made using the followed microscopes:

- JEOL JSM-5910LV scanning electron microscope (SEM) equipped with EDS detector Pentafet 7324 (Oxford Instruments), 133eV (nominal area 10mm^2) with ATW2 window.
- Carl Zeiss EVO MA10 scanning electron microscope (SEM) equipped with EDS detector X-Act (Oxford Instruments) of solid-state analytic silicon ADD, 129eV (nominal area 10mm^2) with SATW window to element detection since Be-Pu.
- Field-Emission SEM (FESEM) Jeol JSM-7100 with EDAX probe and Silicon Drift Detector (SDD) X-MaxN.

Thermo Gravimetrical Analysis- TGA

SETARAM SETSYS Evolution was used to study the hot-corrosion mechanism of YSZ powders at different temperatures. A platinum crucible was employed to avoid any contamination of the samples and any reaction of the crucible with salt mixture. Details about the treatments realized in TGA will be discussed in section 4.4.2.

Raman Spectroscopy

Raman spectroscopy was used to identify the phase changes in coatings cross-section. The equipment used was a Horiba LabRAM HR Evolution μ-Raman microscope, equipped 532-nm Ar laser (green-visible) and Olympus microscope. The spectra were taken in a range between 120 to 200 cm^{-1} with a 50x objective, and acquisition time of 5 seconds.

4.3.2 Characterization

Sample preparation

Sample preparation was performed following the ASTM E1920 standard (Standard Guide for Metallographic Preparation of Thermally Sprayed Coatings), where the following steps were carried out:

1. A resin mounting was carried out in a vacuum impregnation equipment Buehler Cast N 'Vac 1000®. Polyester resin from *Protokimica* was used for mounting. The amount of catalyst (number of drops) was determined according to the following equation:

   Ndrops=(0.51)(Resin Weight)

2. Cross-section cutting was made using a Buehler Isomet 1000® precision cutter at 975 rpm and constant load. Oil-based coolant was used to cut samples subjected to hot corrosion and water coolant for the rest of the samples.

3. Sample polishing was initially done with SiC papers with grit sizes varying from ASTM 200 to 2000 and alcohol as a lubricant. Subsequently, 6, 3 and 1 μm diamond poly-crystalline suspension were used for fine polishing. Moreover, 6 and 3μm oil-based diamond mono-crystalline suspension were used for hot corrosion test samples.

Porosity quantification

Porosity quantification was performed following the ASTM E2109 standard (Standard Test Methods for Determining Area Percentage Porosity in Thermal Sprayed Coatings), where 20 images were taken at 400x using an optical microscope to make the quantification. Image analysis was performed with ImageJ software® using Sauvola algorithm to do threshold as observed in figure 4.11.

Figure 4.11: Image processing using ImageJ.

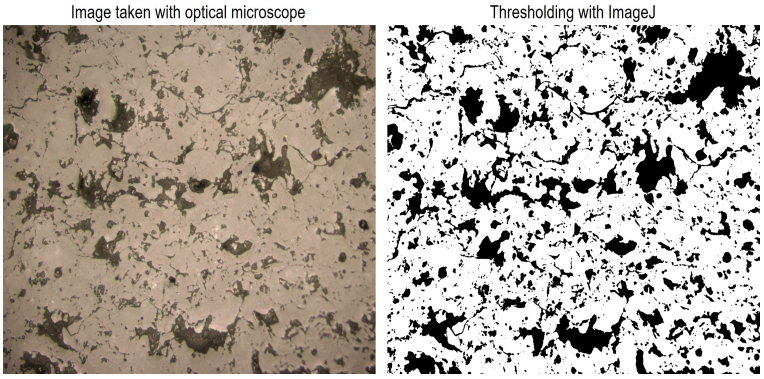

Adhesion-Cohesion test

For the adhesion-cohesion test, Inconel 625 cylinders with 1 inch of diameter and 2 inches of high according to ASTM C-633 (Standard Test Method for Adhesion or Cohesion Strength of Thermal Spray Coatings) were used. The adhesive used was HTK Ultra Bond 100, and sample preparation was made according recommendations of ASM Thermal Spray Society [93], and Thermal Spray Centre (CPT) of the Universidad de Barcelona as follows:

1. A mating cap was sand-blasted with F24 corundum for 30 seconds to obtain a Ra between 5-6μm.
2. The mating cap and bond cap cylinders were cleaned, degreased, and drying before application of adhesive.
3. The adhesive was applied to mating and bond cap
4. A fixture was used to assemble and cure bond test samples. 14 N.m of torque to each sample was applied during curing (see figure 4.12a).
5. Samples were cured into a furnace at 185 °C during 2.5 hours.

The samples were tested using a universal machine Servosis of 10 Ton with a displacement velocity of 0.02 mm/seg (see figure 4.12b). The first test carried was for only the adhesive, where their adhesive-cohesive strength was 76.04$\pm$4.04 MPa.

Figure 4.12: Adhesive-cohesive test (a) fixture (b) universal machine.

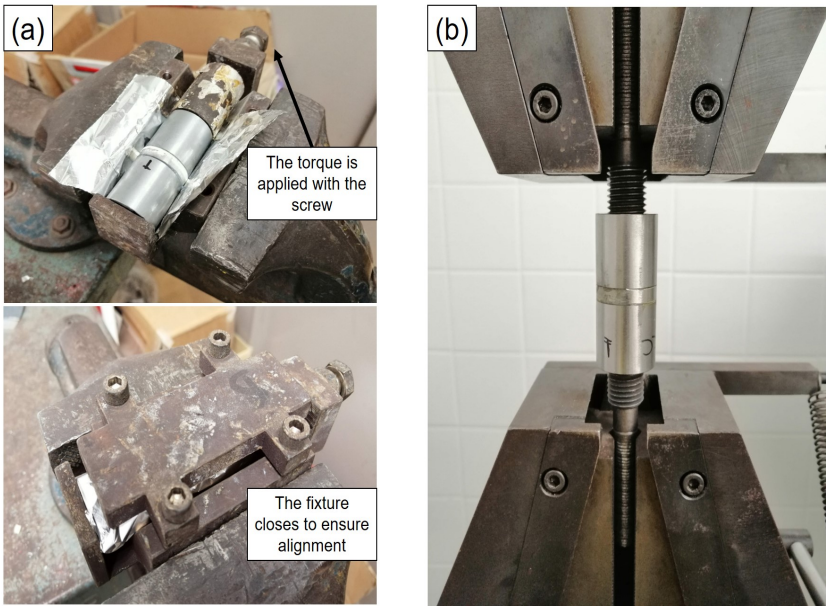

Thermal shock tests

In order to evaluate the thermo-mechanical properties of bilayer systems, thermal shock tests were performed using a muffle furnace. The thermal cycle was defined as follows: The temperature was set at 1020°C for 5 minutes of soaking time. After heating, the samples were directly quenched into water, dried and introduced into furnace. The total number of cycles was 600, where the water temperature throughout the cycling was in between 20 and 30°C. More than 20% of the spalled layer was adopted as a failure criteria for the coating. The performance of the YSZ and bilayer systems was compared with a conventional TBC system (without LP-YSZ layer).

4.4 Hot corrosion tests

4.4.1 Preliminary conditions

In order to define the corrosion tests protocols, some initial experiments were performed onto the cold-pressed 7YSZ powder (Metco 204 NS-G of Oerlikon Metco) with 1/2 inches of diameter and weight of 0.8 g using factorial design 2^k (k=2), where the concentration (wt.$\%$) and salt composition (Fraction of Na_2SO_4 in V_2O_5) of the salt mixture were the experimental factors. Mixtures of high purity vanadium pentoxide (V_2O_5) of Aldrich chemistry and sodium sulfate (Na_2SO_4) of J.T. Baker were used. The experiments were carried in an electrical furnace at 1000 °C with a heating rate of 7 °C/min and 10 hours of exposure time. The levels of the factors were chosen according to the work of Chen et al [68] for the salt concentration, and the V_2O_5-Na_2SO_4 phase diagram (see figure 3.20) for the mixture composition, in such a way that the conditions for the reaction described in Eq. 3.8 are fulfilled [60, 64]. Such levels are shown in Table 4.6.

Each condition was performed in triplicate. A central point was added to observe the behav-

Table 4.6: Factorial design of the hot corrosion experiments.

	Factor	Levels		
		Low	High	Central
A	**Concentration (%)**	0.1	1	0.55
B	**Salt composition (Fraction of Na_2SO_4 in V_2O_5)**	0.2	0.44	0.32

ior within the experimental area, and the experimental sequence was accomplished using randomness criteria. The experimental sequence is shown in table 4.7. The variable response was the percentage of monoclinic phase measured by X-Ray Diffraction, and the DoE analysis was carried using Minitab 17 software®.

Table 4.7: Experimental sequence of the tests

Sequence	Order	Concentration (%)	Composition (Fraction of Na_2SO_4 in V_2O_5)
1	1	0.1	0.2
2	8	1	0.44
3	4	1	0.44
4	7	0.1	0.44
5	13	0.55	0.32
6	6	1	0.2
7	2	1	0.2
8	10	1	0.2
9	3	0.1	0.44
10	14	0.55	0.32
11	11	0.1	0.44
12	12	1	0.44
13	15	0.55	0.32
14	5	0.1	0.2
15	9	0.1	0.2

4.4.2 Temperature influence

Using the conditions of composition and concentration determinate in the section 4.4.1, a second set of experiments were carried out at 490, 700, 900 and 1100 °C for 7YSZ powder with the aid of a Thermal Gravimetric Analysis (TGA) equipment with a heating rate of 7°C/min in air atmosphere during 10 hours and using a Platinum crucible. The samples were characterized by X-ray diffraction to establish the temperature with major tetragonal destabilization.

4.4.3 Tests in coatings

The HC conditions determined in the sections 4.4.1 and 4.4.2 to test the coatings were:

- Salt composition: 32 wt.% Na_2SO_4 and 68 wt.% V_2O_5
- Temperature: 900°C

- Concentration: 1 wt.%
- Exposure time: 10 hours

In order to calculate the salt concentration deposit onto the deposited coatings, the coating was detached to the substrate using a solution of $FeCl_3$, HCl, HNO_3 and deionized water according to the methodology proposed by D. Zambrano [29] and J. Zhang [94]. The detached coating weighed 1g approximately. This solution dissolves the bond coat leaving the topcoat, as observed in figure 4.13.

Figure 4.13: Coating detachment.

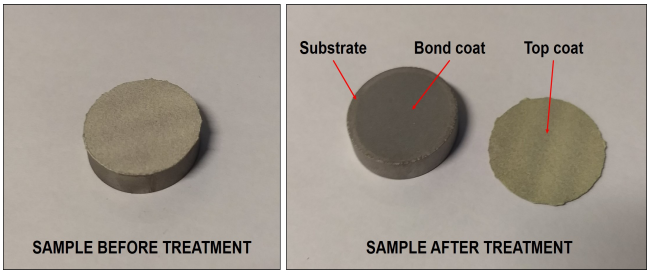

To study the Hot Corrosion resistance of the bilayer systems, 3 types of HC tests were conducted as follows, and each of these was carried out in triplicate:

- **HC- Standard** Using the conditions according to results in sections 4.4.1 and 4.4.2
- **HC- Concentration:** Using 3 different concentrations (1, 3 and 5 wt.%).
- **HC- Cycles:** The samples were taken out after every 10 hours of exposure to hot corrosion followed by re-exposure of the samples to the same conditions replenishing the salts.

5 Results and discussion

5.1 Hot corrosion tests in powders

Experiments described in section 4.4 were focused on developing a laboratory methodology to determine the Hot corrosion conditions used in coatings. Figure 5.1 shows the X-ray diffractograms of the 7YSZ samples exposed to the central and extreme levels of the proposed design of experiments (i.e., sequences 1, 2 and 12 in table 4.6). Identification of the main peaks shows an increase of monoclinic phase with respect to the as-received 7YSZ powder and presence of the YVO_4 phase. Moreover, the intensity of the (101) peak of tetragonal phases (i.e., 2θ=30.1°) is clearly attenuated as result of its transformation to the monoclinic phase. Figure 5.1b confirms the presence of YVO_4 phase with the characteristic rod and needle morphologies [12, 19].

Figure 5.1: (a) X-ray diffraction of untreated, low, medium and high levels of DoE design (see table 4.6 and 5.1) (b) SEM image of YVO_4 crystals after the corrosion test under medium level conditions.

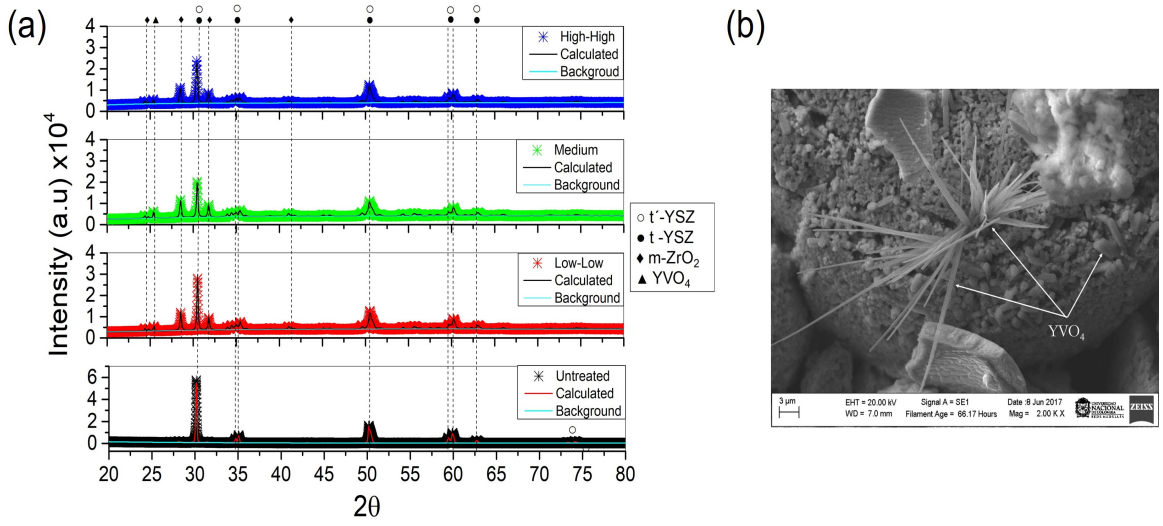

After the Rietveld refinement, the presence of both tetragonal phases (*t* and *t'*) was observed and quantified for all tested conditions. The intensity reduction of tetragonal main peaks shown in figure 5.1a and the formation of HC products are consistent with the fluxing of Y_2O_3 by the molten salt through the Lewis acid-base reactions described in equations 3.10 and 3.11 [10, 16, 60, 68]. Table 5.1 lists the DoE sequence of factorial design and the phase quantification results by Rietveld analysis as well as the data accomplished with Homoscedasticity criteria.

Table 5.1: Experimental sequence of DoE and phase quantification

Sequence	Concentration (%)	Composition (Fraction of Na_2SO_4 in V_2O_5)	% m-ZrO_2	% t'-YSZ	% t- YSZ
1	0.1	0.2	59.11	17.85	23.05
2	1	0.44	58.74	22.32	18.94
3	1	0.44	61.72	22.43	15.86
4	0.1	0.44	30.15	36.00	33.85
5	1	0.2	77.32	12.14	10.53
6	1	0.2	77.70	5.24	17.06
7	1	0.2	86.39	4.51	9.10
8	0.1	0.44	36.70	35.25	28.05
9	0.55	0.32	72.95	8.82	18.23
10	0.1	0.44	31.66	30.09	38.24
11	1	0.44	52.55	19.29	28.16
12	0.55	0.32	70.61	20.62	8.77
13	0.1	0.2	52.21	28.68	16.11
14	0.1	0.2	35.72	40.10	24.17
15	0.55	0.32	66.02	20.01	13.97

Lattice parameters of tetragonal phases showed values of c/$\sqrt{2a}$ ratio of 1.016 and 1.009 for *t* and *t'* phases respectively, which are typical for these phases [95–97]. The results show that the lowest content of the monoclinic phase for all treatments is observed in sequence 4, with circa 30%. In addition, an increment in the Yttria-lean t-YSZ phase is observed in all sequences due to yttria depletion as a result of the reaction of YSZ with the salt mixture, obtaining a maximum value of 38% in sequence 10. As the amount of t-YSZ increases, it is reasonable to expect that the prejudicial tetragonal-to-monoclinic phase transformation occurs as well.

The results of the factorial design are shown in figure 5.2. The Pareto chart in figure 5.2a shows with a confidence of 95% and R^2-adj. of 85.60% that both concentration (A) and composition (B) are relevant to the tetragonal destabilization while the combined effect (AB) is not significant. This implies that composition and concentration are statistically independent factors, and their interaction of the different levels have no influence in the tetragonal phase content.

The Main Effects Plot in figure 5.2b shows the dependence of the response variable (% of monoclinic phase) with the exposure factors, where the highest concentration (i.e., an initially thicker salt melt mixture) and the lowest composition (i.e., a more acidic salt melt mixture) led to a larger destabilization of the tetragonal phase (higher amount of m-ZrO_2). When a higher concentration is used, more salt is available to react with the Y_2O_3 in 7YSZ, increasing the reaction time and therefore the HC products according to equations 3.10 and 3.11 . Conversely, a higher concentration of Na_2SO_4 decreases the melt acidity [17, 60, 98] generating a less aggressive HC attack. It is worth noticing that the central point (red dots in figure 5.2b) shows nonlinear behavior within the experimental region studied and the m-ZrO_2 content is higher than in the corner levels ($\sim$70%). The composition (32 wt.% Na_2SO_4

Figure 5.2: (a) Pareto chart of the effects (b) Main effects plot for monoclinic phase.

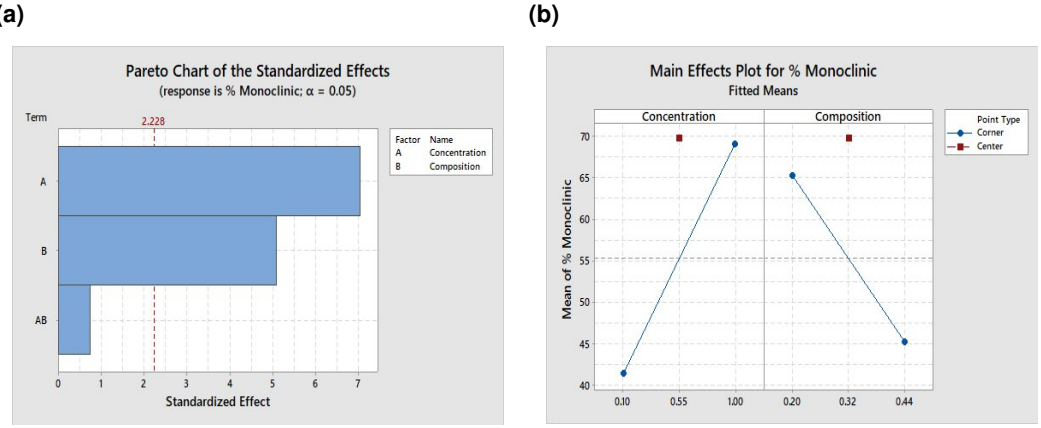

+ 68 wt.% V_2O_5) corresponds to the eutectic mixture, which has an eutectic temperature of 500 °C [64]; therefore, a larger amount of molten salt is formed in the early stages of the test, which increases the quantity of Y_2O_3 that can be fluxed from the 7YSZ in comparison with other salt compositions. In summary, the exposure conditions that promote the larger salt-induced hot corrosion degradation of 7YSZ in the experimental levels used (i.e., lowest tetragonal content) include:

- Salt mixtures with higher acidity (i.e., higher V_2O_5 content).
- Higher salt concentration (i.e., thicker molten salt layer).
- Earlier formation of the molten salt.

In order to investigate the effect that the amount of molten salt has on the 7YSZ degradation, two concentrations were evaluated at the Na_2SO_4-V_2O_5 eutectic composition. Figure 5.3 shows the TGA curves and X-ray diffractograms of 7YSZ powders after HC tests in Na_2SO_4-V_2O_5 eutectic salt mixtures with concentrations of 0.55% and 1% of at 1100°C.

Figure 5.3: Thermal properties during HC test and crystal structure of the powder after HC tests with concentrations of salts of 0.55% and 1% at 1100°C. a) TGA measurements, b) X-ray diffractograms.

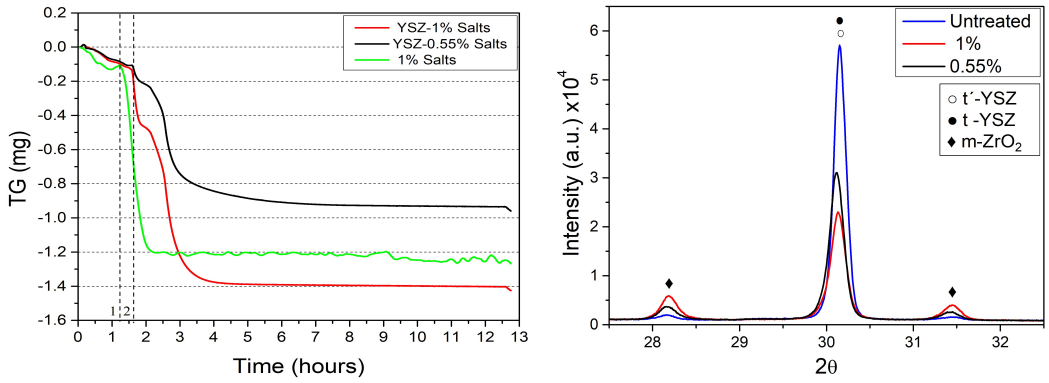

7YSZ powders treated under different salt concentrations have similar tendencies to lose mass during the heating cycle. At 700 °C both curves show an abrupt change of slope

(dashed line 2 in figure 5.3a), followed by a stabilization period after 5 hours of thermal treatment. The total mass loss after the stabilization period is 0.93 mg and 1.40 mg for the concentrations of 0.55 and 1% respectively. Salt mixture Na_2SO_4-V_2O_5 without 7YSZ powder was also tested at 1100°C as a baseline (8 mg that correspond to a concentration of 1 wt.%). Similar behavior to the other curves with a mass loss of 1.22 mg was observed, an amount comparable with 7YSZ with salts; moreover, the sample presented a change of slope in the eutectic temperature (dashed line 1 in figure 5.3a) and stabilization after 2 hours. This behavior is related to salt evaporation since the mass loss is proportional to the amount of Na_2SO_4 tested. X-ray diffraction results (figure 5.3b) show that the concentration 1 wt.%. of salt mixture causes a significant destabilization of the tetragonal phase since its characteristic peak intensity is decreased (2θ= 30.1°C), whereas the peaks intensities of the monoclinic phase (2θ= 28.1°C and 31.4°C) increase. This result confirms that the high amount of m-ZrO_2 observed at the central point of DoE design is due to the proximity of the composition of the mixture to the eutectic composition. Consequently, 1 wt.% of salt concentration and the eutectic composition (32 wt.% Na_2SO_4 + 68 wt.% V_2O_5) were the parameters selected to observe the influence of temperature on the hot corrosion mechanisms.

5.1.1 Temperature influence on HC-attack

Figure 5.4 shows the TGA curves during the Na_2SO_4-V_2O_5-induced HC of 7YSZ powder at different temperatures.

Figure 5.4: TGA measurements at 490, 700, 900 and 1100 °C. Tests performed with 1% of salt concentration and the eutectic composition (0.32 wt.% Na_2SO_4 + 0.68 wt.% V_2O_5).

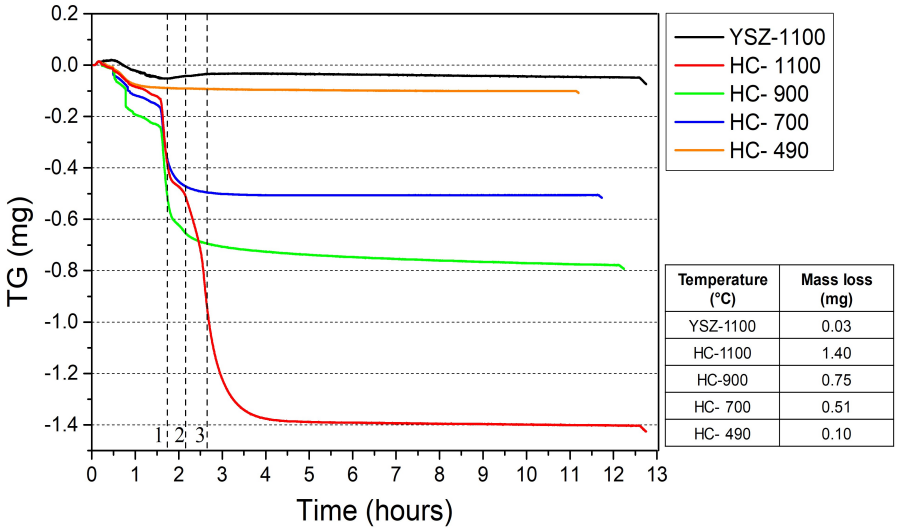

Temperature (°C)	Mass loss (mg)
YSZ-1100	0.03
HC-1100	1.40
HC-900	0.75
HC- 700	0.51
HC- 490	0.10

The mass loss of 7YSZ powder exposed to the eutectic mixture (marked “HC” in the graph) increases as a function of temperature. From the results, it is observed that the test YSZ-1100 (without salt exposure) and HC-490 showed a negligible mass loss. Examining the reaction between Na_2SO_4 and V_2O_5 (equation 3.8), for the salt mixture concentrations used experimentally 1wt.% (8 mg: 2.56 mg Na_2SO_4 + 5.44 mg V_2O_5) and 0.55wt.% (4.4 mg: 1.4 mg Na_2SO_4 + 3 mg V_2O_5), the calculated SO_3 production assuming 100% reaction efficiency was 1.46 mg and 0.83 mg respectively. These values are comparable with the mass loss presented in figure 5.3a. Therefore, the mass loss measured in the samples with salt

treatment can be mainly associated with the SO_3 evaporation and the samples below this temperature have pyrosulfate ($S_2O_7^{-2}$) in their melt. These results are in agreement with the changes observed in the curves HC-700 to HC-1100 of figure 5.4. At 700°C (dashed line 1 in figure 5.4), the curves present an abrupt change in the slope due to an increment of SO_3 production (equation 3.8) followed by mass stability after reaching this temperature. A similar result was previously reported by Seiersten and Kofstad [99] in which SO_3 formation at temperatures from 650°C and higher were observed for a mixture of Na_2SO_4 and V_2O_5. For the HC-1100 curve, an abrupt mass decrease was observed after 900°C (dashed line 2) followed by a mass stability region after 1100°C (dashed line 3).

X-ray diffractograms of the samples after TGA analysis are presented in figure 5.5. For the samples treated with salt mixture, tetragonal (*t'* and *t*), monoclinic (m-ZrO_2) and YVO_4 phases are clearly observed. Figure 5.5a shows that the sample HC-900 presents a low intensity of the characteristic tetragonal peak at 2θ=30.1°, (101) plane. Higher intensity is observed for characteristic monoclinic peaks at 2θ=28° and 2θ=31.5°, (-111) and (111) planes respectively, and YVO_4 peak at 2θ=24.9°, (200) plane, compared with samples treated at other temperatures. At higher angles (figure 5.5b) the reduction of peaks intensities at 2θ= 73.2° and 74.2°, corresponding to (004), (400) planes of t'-YSZ, and 74.4° corresponding to the (400) plane of t-YSZ [51, 97], indicate a greater destabilization of non-transformable and tetragonal phase of the sample at 900°C.

Figure 5.5: X-Ray diffractograms of the samples submitted to TGA (with and without salts) at different ranges a) 27.5-32.5°, b) 72-76°, c) 20-27°.

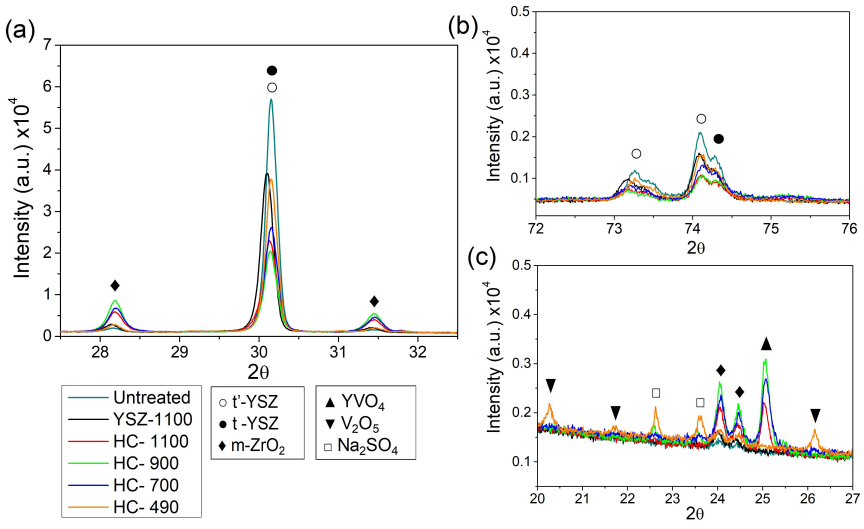

The samples HC-490 and YSZ-1100 have a significant reduction of the intensity of the peak located at 2θ=30.1° compared with the untreated sample. Moreover, the HC-490 sample present peaks corresponding to Na_2SO_4 and V_2O_5 with no evidence of YVO_4 phase presence (see figure 5.5c). Therefore, $NaVO_3$ and YVO_4 formation reactions (equations 3.8, 3.10, 3.11) are sluggish or may not take place at this temperature (confirming the results of figure 5.4), in which case thermal effects produce the observed destabilization of the tetragonal phase. In our case, a more severe degradation is expected because the particles have a large surface area, which enhances diffusion mechanisms of Yttria reported in the literature [51, 97].

Figure 5.6 presents the results of the Rietveld quantitative phase analysis, where the amount of tetragonal-to-monoclinic phase transformation increased with the temperature, reaching a maximum of m-ZrO_2 at 900°C. A greater amount of YVO_4 phase was observed in the samples treated at 900°C in comparison to the samples treated at ones temperatures.

Figure 5.6: Phase content of the samples after hot corrosion tests at different temperatures.

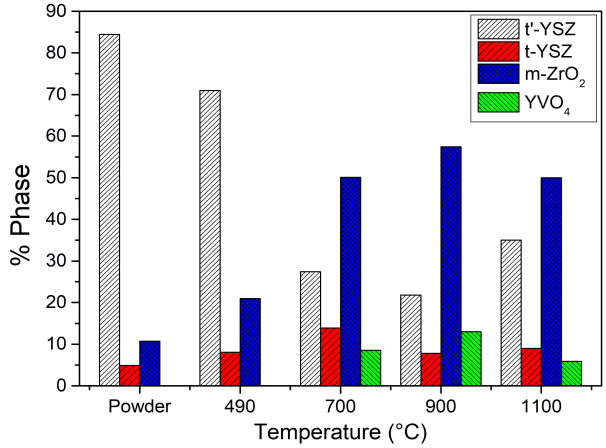

The sample treated at 1100°C presents amounts of m-ZrO_2 and YVO_4 phases similar to those found in the sample treated at 700°C but lower than those of the sample treated at 900°C. This behavior is attributed to elevated SO_3 evaporation at 1100°C (see figure 5.4) [9, 58].

$$k = \frac{(aNaVO_3)^2.PSO_3}{aNa_2SO_4.aV_2O_5} \tag{5.1}$$

Equation 5.1 shows that the partial pressure of sulfur trioxide (PSO_3) and the sodium metavanadate activity ($aNaVO_3$) have a prime influence on V_2O_5 activity [58]. According to TGA results (figure 5.4), the sample HC-1100 may have lower V_2O_5 activity in the melt, so the chemical reaction showed in equation 3.11 would not control the hot corrosion attack. Instead, the 7YSZ degradation would be better described by equation 3.10, with $NaVO_3$ being the limiting reagent. Conversely, the HC- 900 and HC-700 treatments do not show complete SO_3 evaporation (the excess SO_3 in the form of pyrosulfate anion ($S_2O_7^{-2}$) in the melt [98]), so the V_2O_5 activity is greater in these cases and the degradation can be driven by the reactions given in equation 3.10 and 3.11 simultaneously. As a result, the HC- 900 and HC-700 degradation is greater compared with HC-1100, and the reaction kinetics depend on their temperature.

Figure 5.7 shows the 7YSZ powder after Na_2SO_4-V_2O_5 HC at 700, 900 and 1100°C where rod-type and needle-shaped structures on the particle surface are observed. These are characteristic of YVO_4 crystals, where changes in salt composition affect the type of structure that grows [100]. As a result, salt evaporation at temperatures above 900°C could promote the formation of needle-shaped crystals perpendicular to the surface of the powder particles, as seen in the sample treated at 1100°C where needles of 7 μm of length can be observed. In the case of the samples treated at 700°C, changes in the salt due to evaporation seem to favor a rod-type morphology of the crystals.

Figure 5.7: Powder morphology after hot corrosion test at 700, 900 and 1100°C.

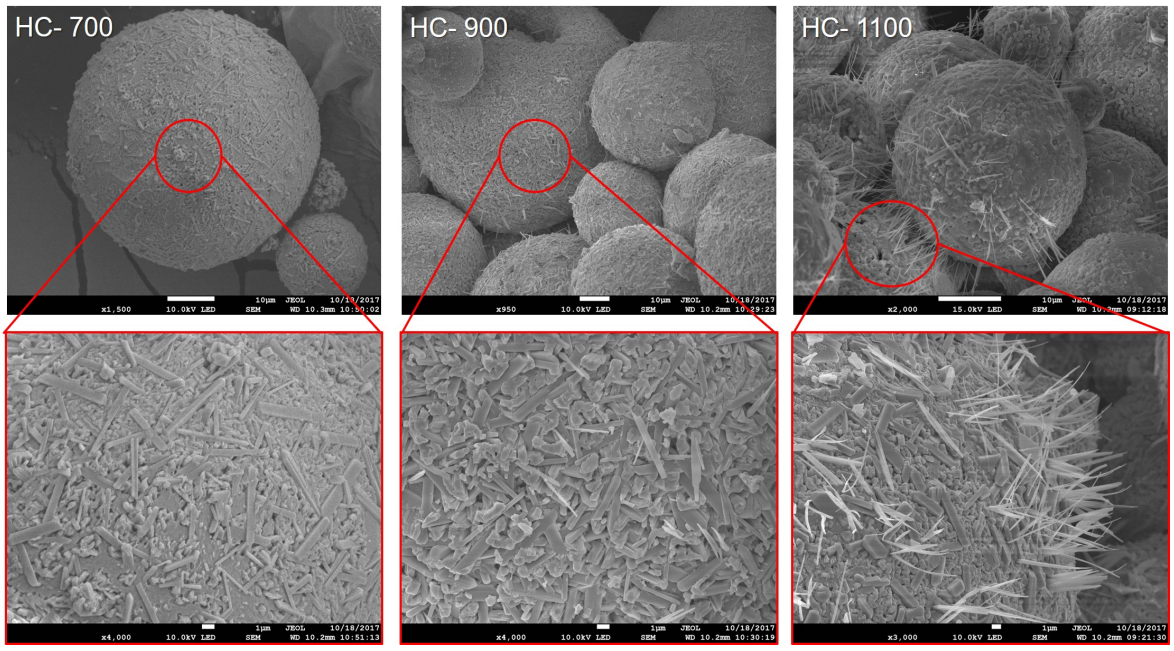

The EDS elemental distribution of rod-type microstructures shown in figure 5.8a confirms the presence of Y and V with residual Zr and Na signals. Backscattered electron imaging of the particle cross section (figure 5.8b) shows variations of chemical composition as local EDS analyses confirm the increase in Na and V contents towards the surface. These results support the fluxing mechanism proposed by Reddy and Gandhi [9], according to which the salt melt dissolves a surface layer with a thickness on the order of a few micrometers. This layer precipitates into YVO_4 (rod and needle type structures) and m-ZrO_2 during cooling.

Figure 5.8: EDS analysis of sample treated with salts at 1100°C. (a) Elemental maps, (b) Local analysis of particle cross-section.

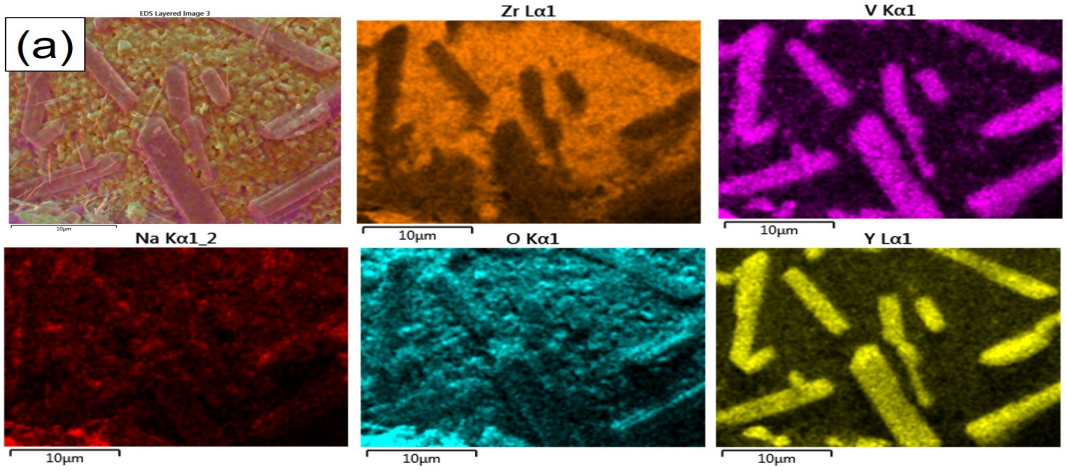

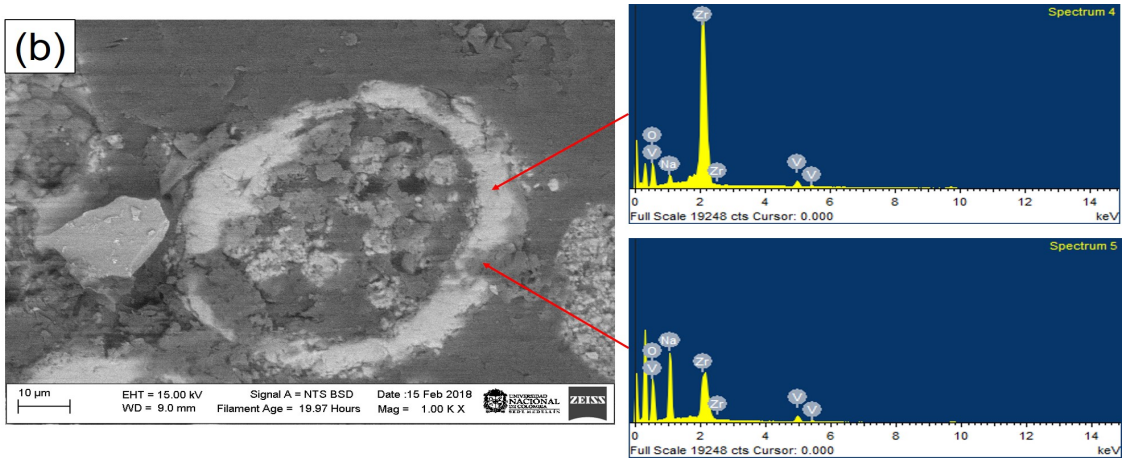

The surface morphology of the sample with salt treatment at 490°C is shown in figure 5.9. No significant changes are evident at the 7YSZ surface morphology although some elongated and irregular salt particles are observed. EDS mapping shows that these particles are rich in either V or Na and S, which is consistent with the results from X-ray diffractograms (see figure 5.5a and 5.5c), where peaks of Na_2SO_4 and V_2O_5 are observed but no HC products are detected. In consequence, it is argued that the intensity reduction of 2θ=30.1° peak in the sample at 1100°C treated without salts is due to thermal effect.

Figure 5.9: SEM/EDS analysis of 7YSZ powder after hot corrosion test at 490°C.

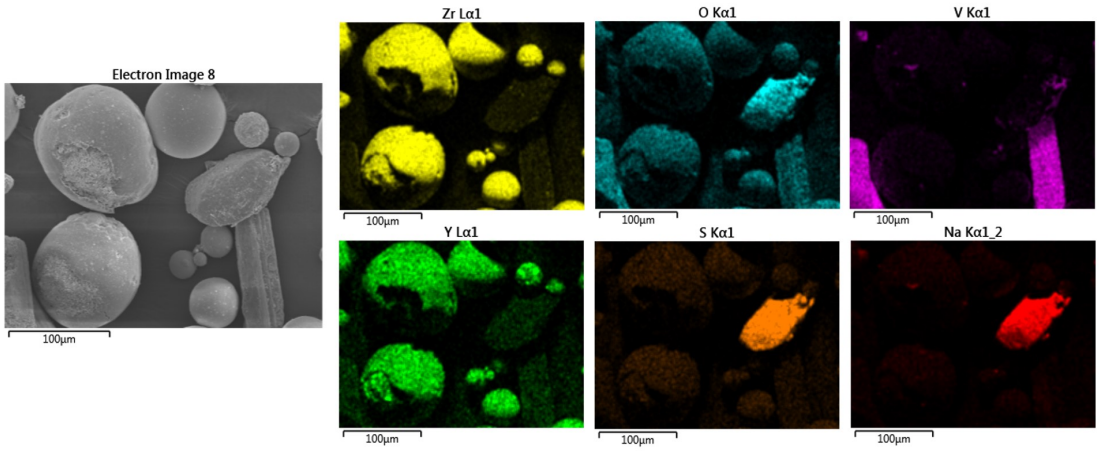

In conclusion, 1% salt concentration, temperature of 900°C and salt composition 32 wt.% Na_2SO_4 + 68 wt.% V_2O_5 were the most aggressive parameters to destabilize the tetragonal phase of 7YSZ. Therefore, these parameters were used to test the HC resistance of APS-deposited CYSZ/YSZ systems.

5.2 Spraying parameters of the Thermal Barrier Coatings

5.2.1 YSZ layer

Measurements of particles temperature and velocity obtained from AccuraSpray system are shown in figure 5.10. An increment in the current and H_2 gas flow increases the particle

temperature, presenting a higher value of 2463 $\pm$ 5°C for the combination of 430 Amperes and 9 NLPM (figure 5.10a).

Figure 5.10: Influence of H_2 flow and current on particle's (a) temperature, and (b) velocity.

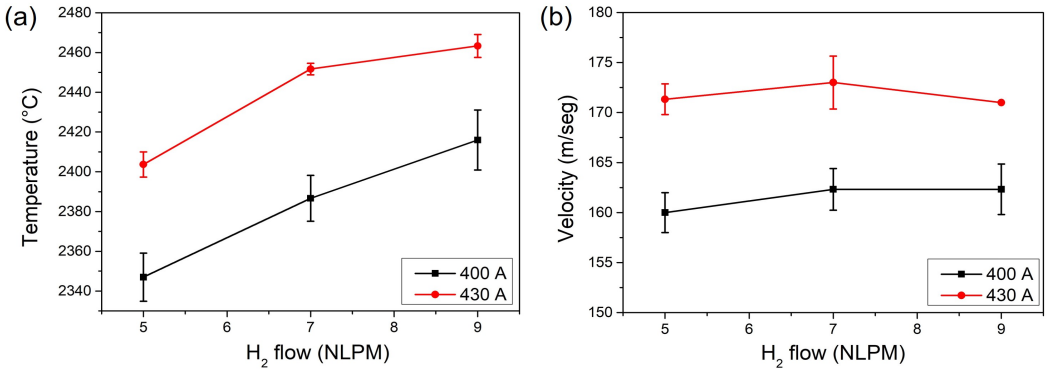

The current increases the enthalpy due to a major ionization. In the case of H_2, due to their diatomic state, their dissociation produces higher energy in the form of heat [25, 26]. Moreover, an increment of hydrogen content causes a reduction of plasma's electrical conductivity, increasing voltage and consequently increases gun power [26]. On the other hand, the experimental levels used of H_2 flow do not present great influence on the particle velocity (figure 5.10b). However, the current increases their velocity by 10 m/s due to a reduction of plasma density with an increment of enthalpy [26].

Coating microstructures obtained with the different spraying parameters are observed in figure 5.11. YSZ microstructure varies drastically by changing the spraying parameters. Nevertheless, the bond coat (BC) had the same amount of defects and maintained a constant thickness of about 120 μm in all tests, ensuring repeatability its deposition.

Figure 5.11: Microstructure of YSZ Top Coat with different spraying parameters.

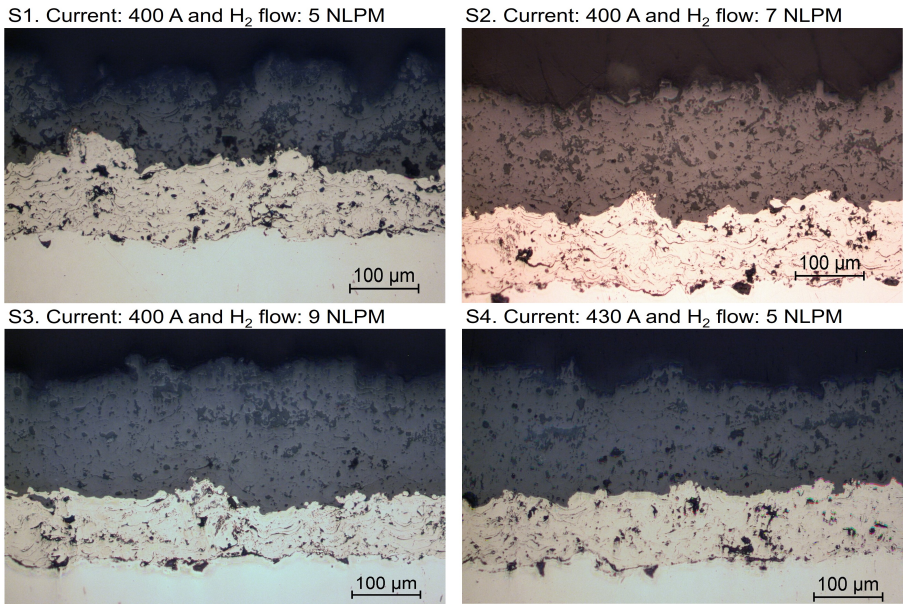

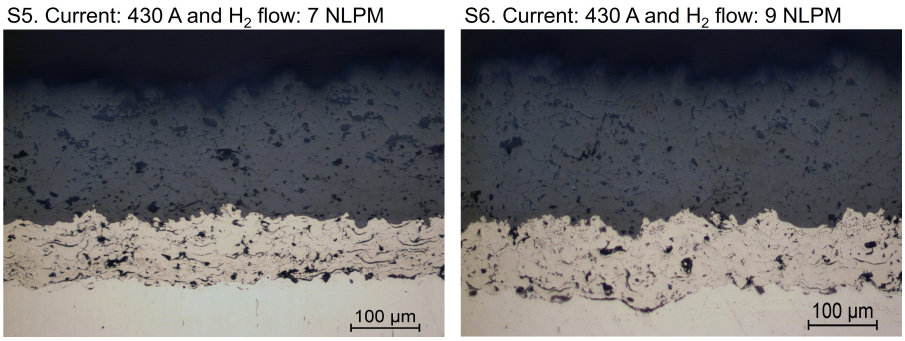

Results of porosity and thickness of the coatings are observed in figure 5.12. Samples S1 to S3 present an average porosity over 20% (S3 has large error bars) because of the low temperature of the particles; therefore, these spray parameters were discarded. The average porosity of samples S4 to S6 is within in the desired range since the particle's temperature and velocity are higher than those of samples S1 to S3. Moreover, the samples S5 and S6 have the major deposition efficiency with coating thickness values 190μm for the same number of passes.

Figure 5.12: Porosity and thickness results of the different spraying parameters. S1: 400 A - 5 NLPM H_2, S2: 400 NLPM A - 7 H_2, S3: 400 A - 9 NLPM H_2, S4: 430 A - 5 NLPM H_2, S5: 430 A - 7 NLPM H_2, S6: 430 A - 9 NLPM H_2.

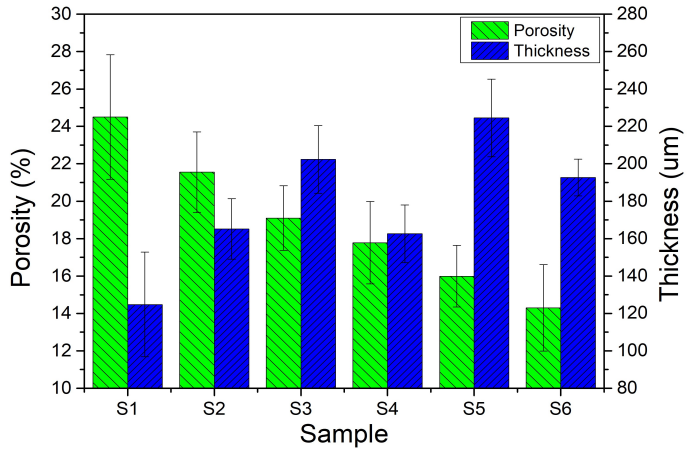

Accordingly, the samples S5 and S6 were chosen for microstructural characterization using X-ray diffraction, whose results are shown in figure 5.13. The diffractograms of the different spraying conditions show the same pattern and peak intensities, hence the H_2 flow in the levels studied have no influence on the crystal structure of as-sprayed YSZ.

The analysis of the X-ray diffraction data reveals the presence of tetragonal phases (*t'* and *t*), plane (101) at 2θ= 30.1°. In addition, main peaks are observed at 2θ= 73.2° and 74.1° which correspond to (004) and (400) planes respectively of the *t'* phase, as well as (004) plane of *t* phase at 2θ=74.4° [97]. Phase quantification results show that the samples S5 and S6 have a *t'* phase content of 87% with c/$\sqrt{2}$a ratio of 1.009 and yttria content of 8.4%. For the case of the *t* phase, c/$\sqrt{2}$a is 1.017 and the yttria content is 3.6%. This result shows that the microstructure did not present significant changes for the spraying parameters. In

Figure 5.13: X-ray diffraction of samples at different spray parameters.

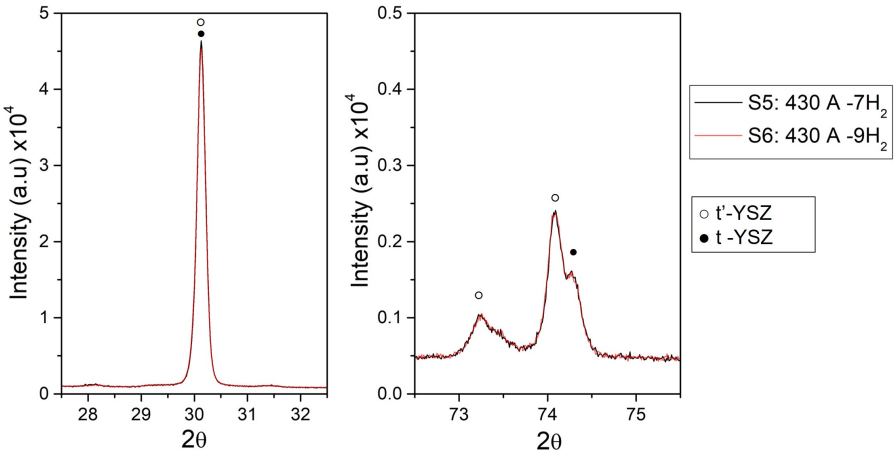

conclusion, the phase content was not distinct enough to select a spray parameter. Therefore, the conditions of the sample S5 (430 amperes and 7 NLPM of H_2) will be used for the deposition of the D-CYSZ/YSZ system. These parameters have major deposition efficiency (thickness per pass), and the porosity is in the range established by the literature, which makes it appropriate to be used as thermal barrier coating.

Finally, adhesion-cohesion test to this sample was carried out showing a strength of 26.98$\pm$ 9.24, where the failure was into substrate/BC interface (figure 5.14). The reported value is within the range for a TBC system [8, 101–104]; therefore, the deposition protocols are adequate for spraying the bilayer systems, and the possible application in a component. The high data dispersion is associated mainly to sample preparation, glue selection, and sample alignment into the fixture [93, 103].

Figure 5.14: Surface analysis of the mating cap (a) surface failure, (b) cross-section.

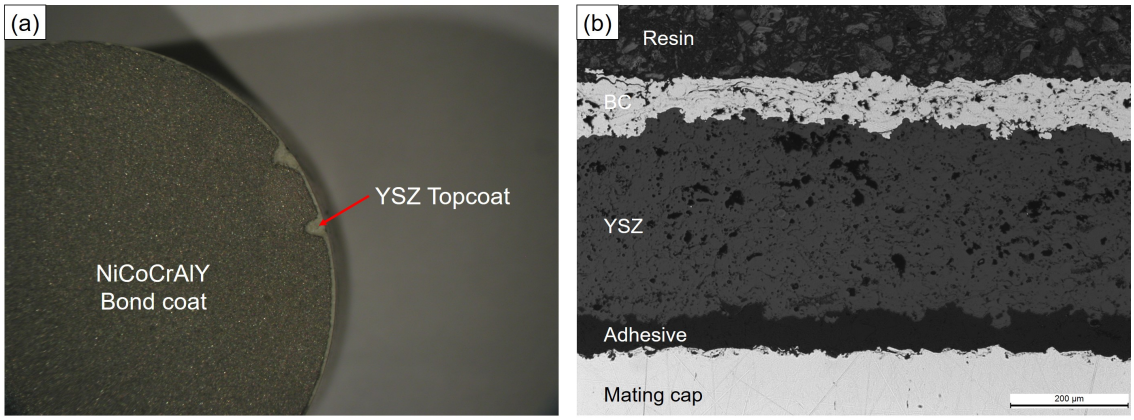

All the surface of the samples tested presented an adhesive failure at substrate/BC interface. Figure 5.14a shows the surface of mating cap, where the bond coat is observed with a slight detachment in the borders due to a *"border effect"* [25], where the coating microstructure is different than in the center or the sample. The cross-section of the mating cap (figure 5.14b) the detachment of the TBC system in observed, verifying that it is an adhesive failure and

that the value of the adhesive-cohesive strength corresponds to the substrate/BC interface. Moreover, the BC, TC, and the BC/TC interface have greater adhesive-cohesive resistance.

5.2.2 D-CYSZ layer

To determine the spraying conditions for dense CYSZ coatings, parameters such as current, spraying distance, and H_2 flow were modified. For the powder used, increasing the current and reducing the distance (low dwell time) increase significantly the density of the coatings, where the changes on the microstructure were apparent from 500 Amperes and 90mm. Figure 5.15 presents the different microstructures obtained at 500, 520 and 540 Amperes with 90mm of spraying distance.

Figure 5.15: Porosity and microstructure of D-CYSZ Top coat at 500, 520 and 540 amperes.

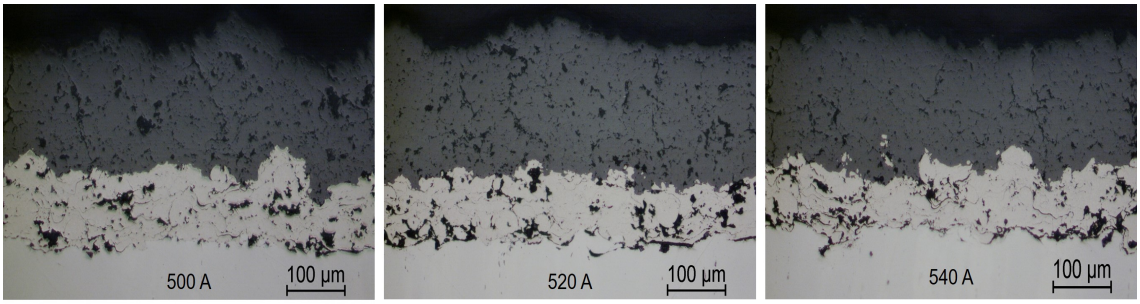

The porosity of the samples was of 9.52±1.53, 8.53±1.32, 5.08±1.20% for depositions at 500, 520 and 540 amperes respectively. The sample deposited at 540 reached the lowest value that can be obtained with this spray technique [25]. The microstructural changes are evident in the coatings cross-section, where a reduction of large and medium pores are observed when increases the current [105].

Figure 5.16 shows the X-ray diffractogram result of as-sprayed CYSZ coating in which the presence of t'-CYSZ as the only phase in the microstructure.

Figure 5.16: X-ray diffractograms of CYSZ powder and as-sprayed D-CYSZ coating deposited at 540 amperes.

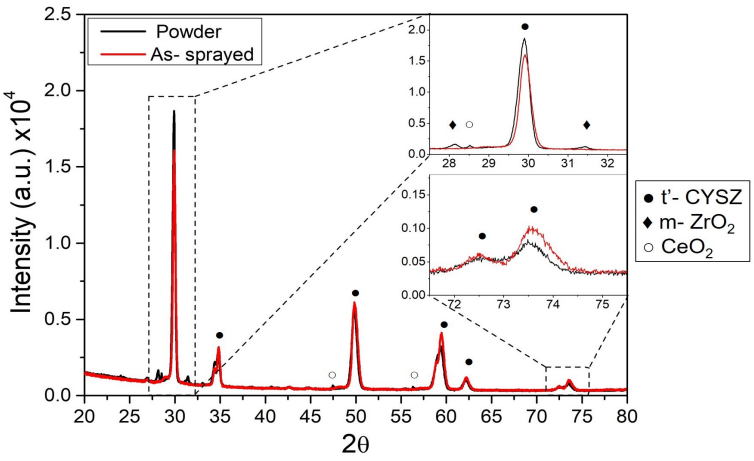

Comparing this result with the diffractogram obtained for the powder, the latter shows peaks

of the m-ZrO_2 and CeO_2 phases that no are present in the coating. After the spraying process, these phases disappear, indicating solubilization of remaining CeO_2 into ZrO_2 during the plasma process allowing the monoclinic-to-tetragonal transformation. Experimental data of particle temperature and velocity could not be obtained because the spraying distance used (90 mm) was too short, and the plasma plume saturated the *AccuraSpray* sensors. With the results obtained in this section, 540 amperes and 90 mm are the parameters that will be used for the dense layer in the deposition of the bilayer systems.

5.2.3 LP-YSZ layer

Based on the spraying parameters of the YSZ and the experimental results obtained with the D-CYSZ layers, current values of 500, 520, and 540 Amperes were used to obtain the Low Porosity YSZ coatings. The temperature and velocity of the particles increased from 2756 to 2830 °C and 237 to 259 m/s for 500 and 540 amperes respectively. Figure 5.17 shows the microstructure obtained on each of the layers.

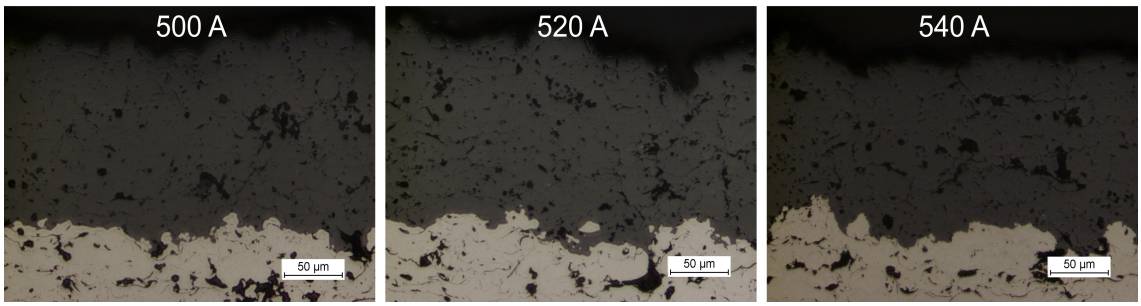

Figure 5.17: Microstructure of low porosity YSZ at 500, 520, and 540 amperes.

Despite the increase in the speed and temperature of the particles no significant changes are observed in the microstructure, which present an average value of porosity of 6%. With this result and considering the electrode lifetime, 500 amperes was chosen as a parameter for the spraying of low porosity YSZ layers.

5.3 Characterization of D-CYSZ/YSZ bilayer coatings

5.3.1 D-CYSZ/YSZ microstructure

The BC and LP-YSZ layers presented average thicknesses of 120.38 $\pm$12.86 μm y 46.75$\pm$6.36 μm respectively. The thickness YSZ and D-CYSZ layers of the different systems are listed in table 5.2, where the values targeted in the experimental plot (see figure 4.8) were accomplished, maintaining a total of 300 μm of TC with low dispersion.

Table 5.2: Thickness of TBC bilayers systems.

System	YSZ thickness(μm)	D-CYSZ thickness (μm)	Total thickness (μm)
YSZ	277.50$\pm$6.61	-	324.25$\pm$6.44
CYSZ50	210.75$\pm$12.26	52.25$\pm$7.89	309.75$\pm$8.57
CYSZ100	151.50$\pm$5.45	99 $\pm$8.91	297.25$\pm$6.89
CYSZ150	101.50$\pm$8.70	159 $\pm$9.06	307.25$\pm$7.72

Figure 5.18 shows the microstructure of the bilayer systems obtained, where the labels YSZ, CYSZ50, CYSZ100, and CYSZ150 stand for the systems without CYSZ layer, 50, 100, and 150 μm thickness of D-CYSZ layer respectively. In all the systems a LP-YSZ layer with 50 μm in thickness was applied onto the NiCoCrAlY bond coat.

Figure 5.18: Microstructures of TBC bilayers system (a) YSZ, (b) CYSZ50, (c) CYSZ100, (d) CYSZ150.

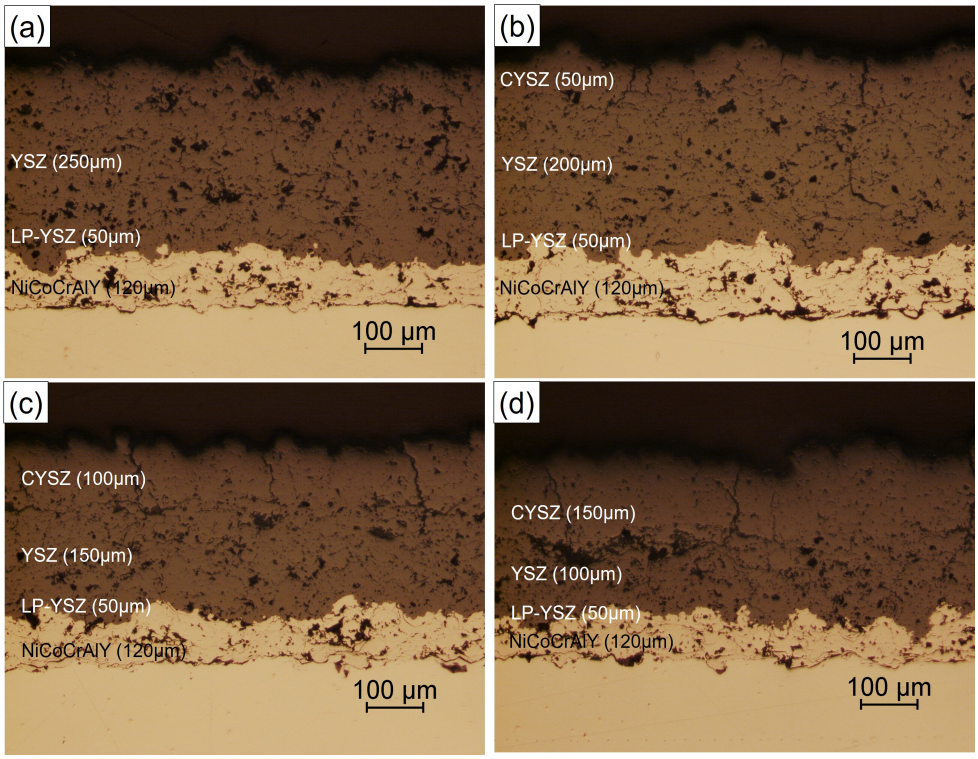

Figure 5.19 shows that the YSZ system presents high density of inter- and intra-splat cracks, as well as large (>16μm), medium (6-16μm) and fine (1-6μm) globular porosity [105], with high inter-connectivity between them. These also is observed in the YSZ layer deposited in the CYSZ systems.

Figure 5.19: Microstructures of TBC bilayers system with higher magnifications. LOM.

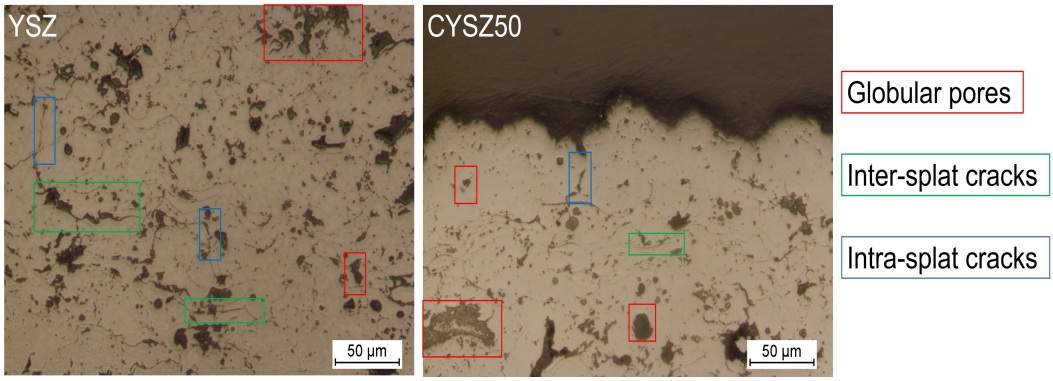

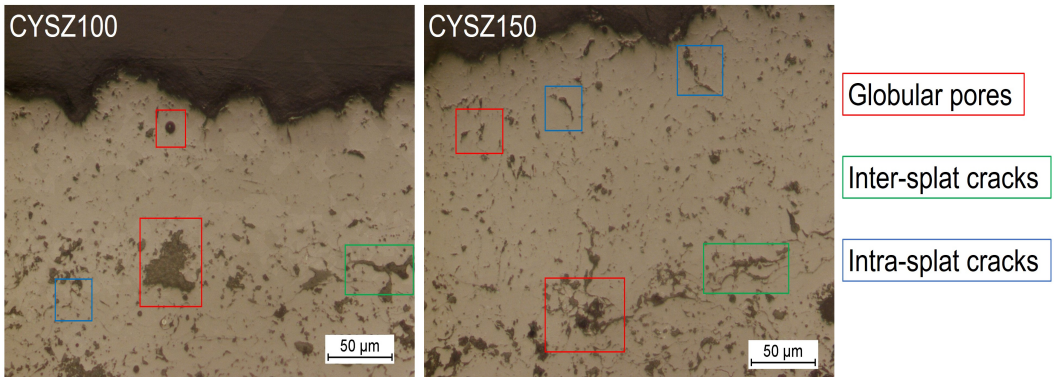

In the dense layers, the absence of inter-splat cracks indicates good wettability between them due to the high energy supplied in the process. However, the presence of fine globular pores indicates that the large particles did not achieve complete fusion [106]. Moreover, these layers present intra-splat cracks and unexpected vertical cracks (figure 5.20) with crack densities of 4.32, 3.87, and 3.19 cracks/mm for the samples CYSZ50, CYSZ100 and CYSZ150 respectively. Due to the insulating nature of the porous YSZ, the heat produced during pre-heat and the spraying (hot particles and plasma plume) causes the thermal expansion of the porous layer, whose thermal expansion coefficient can reach 19.87x10^6 K^{-1} at temperatures between 600 and 900°C [107] (higher than CYSZ (higher than 13x10^6 K^{-1} reported for CYSZ [24]). This generates stresses in the CYSZ layer that are oriented mainly parallel to the free surface of the coating, which, together with the splat boundaries, constitute preferential paths for vertical cracks growth with further temperature changes [108,109]. Although the vertical cracks were not planned in the experimental design, it has been reported in the literature that they improve the thermomechanical performance of D-CYSZ layers. Crack densities up to 3.5 cracks/mm can increase the strain tolerance, relieve the thermal mismatch stresses, and reduce the coating's tensile stiffness, therefore reducing the tendency of the ceramic to crack and buckle [108–111].

Figure 5.20: Vertical cracks formed during coating cooling. LOM.

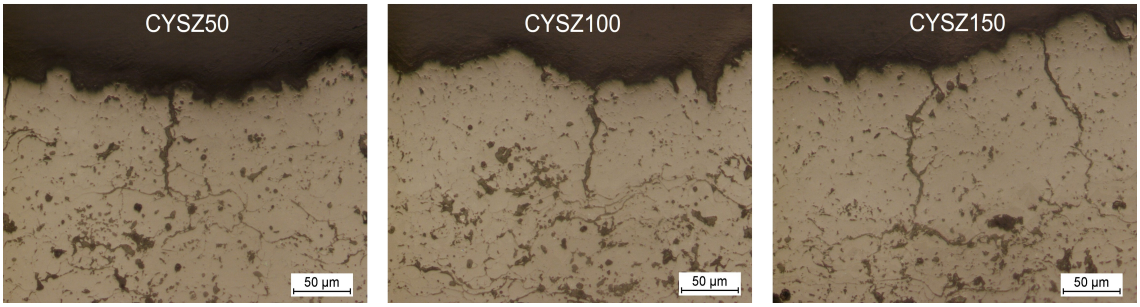

Figure 5.21 shows the BC/TC interface of as-sprayed bilayer systems. All systems present β-phase (NiAl) precipitates, pores and cracks (defects) in the BC, as well as the absence of TGO layer at the interface. In addition, the TC presents inter-and intra-splat cracks and fine globular porosity.

Figure 5.22 presents the SEM images of the bilayers surface. YSZ system present splats with splashing morphology, where large ($\sim$90μm) and medium (30-40μm) diameter ranges

Figure 5.21: BC/TC interface of bilayer systems (a) YSZ, (b) CYSZ50, (c) CYSZ100, (d) CYSZ150.

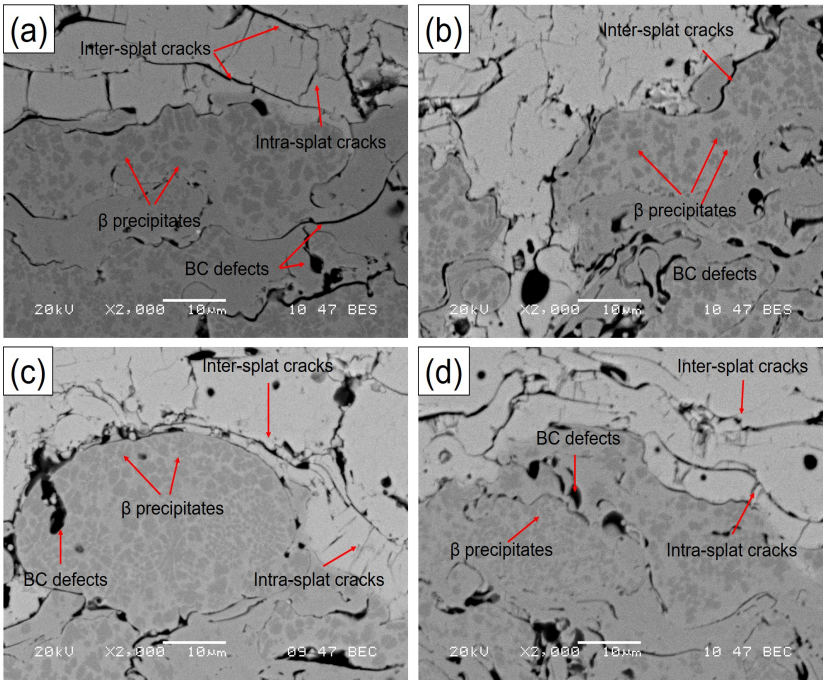

are identified, which are consistent with the particle size distribution of the YSZ powder (section 4.1.2).

Figure 5.22: Surface analysis of YSZ system.

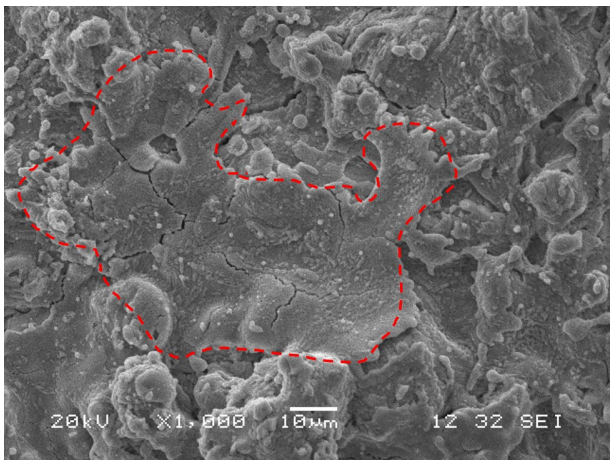

This type of morphology is also observed in D-CYSZ systems (figure 5.23), with major spreading of jagged splats than in YSZ system due to the high temperature difference between the substrate and the particles coming from the plasma [112, 113]. In addition, these systems present a path of interconnected cracks (figure 5.23b to 5.23d), which configure the vertical cracks pattern observed in figures 5.18 and 5.20.

Figure 5.23: Surface analysis of CYSZ (a) CYSZ (b) CYSZ50; higher magnifications (3500x), (c) CYSZ100, (d) CYSZ150.

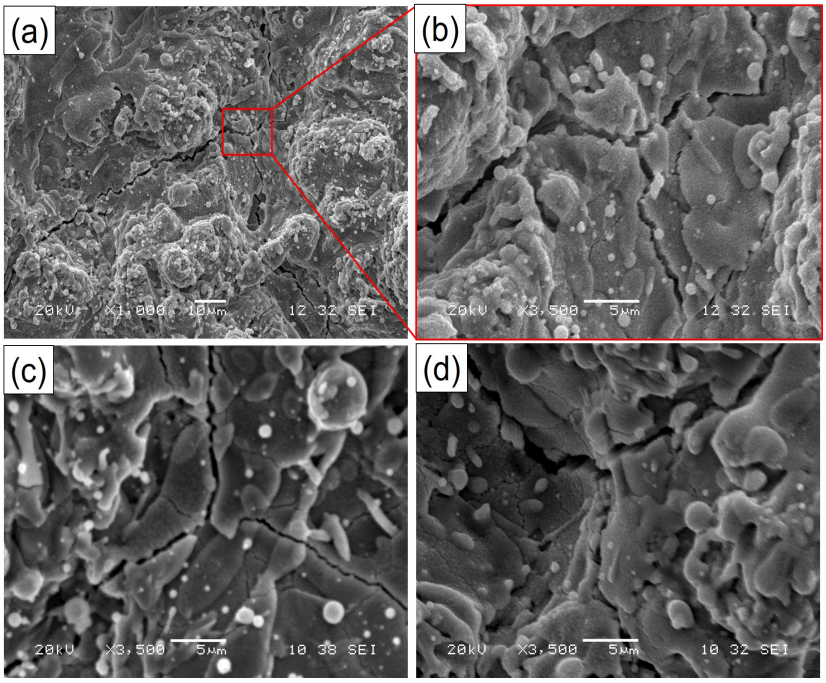

5.3.2 Adhesive-Cohesive strength of D-CYSZ/YSZ systems

Figure 5.24 shows the adhesive-cohesive strength of the TBC bilayer systems tested.

Figure 5.24: Adhesive-cohesive strength of D-CYSZ/YSZ systems.

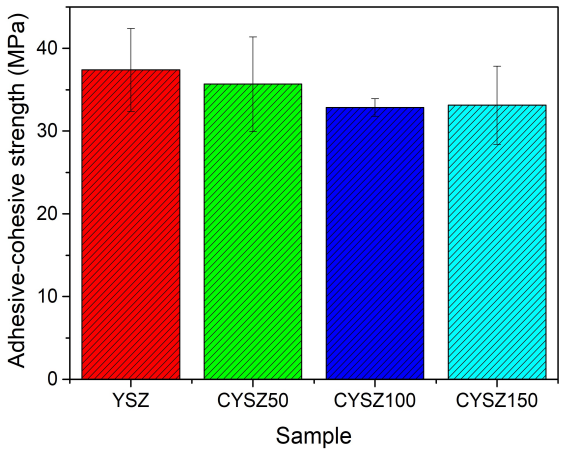

Results show that the adhesive-cohesive resistance of bilayer systems has an average value above 32MPa, which is in the range reported for TBC. Besides, all the bilayer systems presented adhesive failure in the substrate/BC interface with some detachments due to the border effect as shown in Figure 5.25. This indicates that all the adhesive-cohesive strength values obtained for the conventional YSZ layer (section 5.2.1), and the bilayer systems are from the substrate/BC interface. Moreover, the layers (NiCoCrAlY, YSZ, and CYSZ) have high cohesion, the interfaces have high adhesion, and the spray protocol established for

deposition of CYSZ layers on YSZ is suitable to produce TBC coatings in samples and can be scaled for gas turbine components.

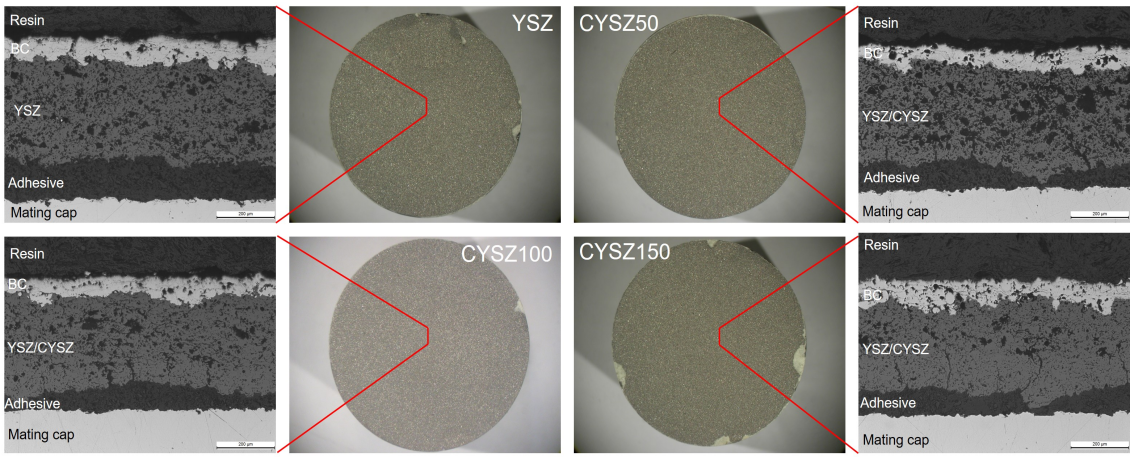

Figure 5.25: Surface failure and cross-section of mating cap of D-CYSZ/YSZ systems.

5.3.3 Thermal shock resistance

Changes in the mass of each sample with a number of cycles of the test can be observed in figure 5.26. Initially, an increment the mass of the samples is evidenced due to the oxidation of the substrate and the BC [114]. As the test goes on, all the samples show mass losses, initially by coating spallation on the surface and by delamination of the layers at the edges until approximately 330 cycles, where the most affected samples were conventional YSZ, CYSZ100, and CYSZ150.

Figure 5.26: Weight gain/loss of the YSZ and CYSZ systems during thermal shock.

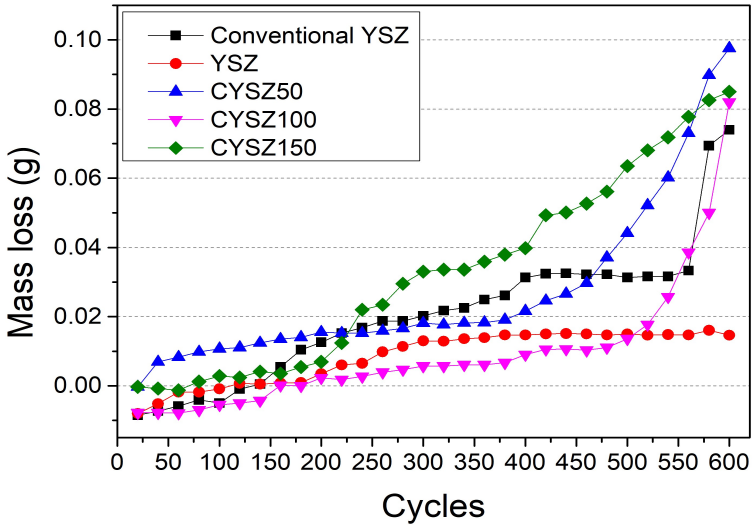

Subsequently, D-CYSZ systems showed a progressive delamination on the CYSZ layer after 350 cycles approximately (figure 5.27). This was evident in the mass loss, where samples CYSZ50 and CYSZ150 showed higher losses. On the other hand, after 600 cycles the

YSZ system does not present failure, indicating that the addition of LP-YSZ increases the thermo-mechanical resistance of the system. Conventional YSZ shows coating delamination of 6.6%, and greater mass loss than YSZ system. On the other hand, delamination of the D-CYSZ layer of 38.10%, 27.22% and 20% for the samples CYSZ50, CYSZ100, and CYSZ150 respectively were measured. This tendency is attributed to the density of vertical cracks, because the presence of inter-splat cracks at the beginning of the vertical crack (see figure 5.20). Therefore, a higher crack density is more likely to interconnect under stresses, generating a greater propagation and subsequent delamination of the coating. However, these systems are not discarded, because the YSZ layer remains intact and can provide thermal protection to the substrate.

Figure 5.27: Surface of TBC system after 600 cycles. (A) total delamination, (B) spallation, (C) edge delamination, (D) CYSZ layer delamination.

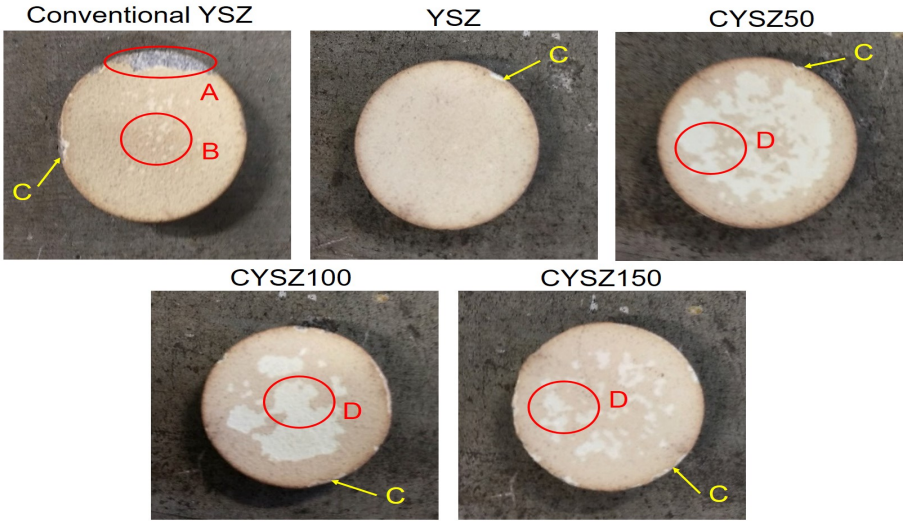

Figure 5.28 shows the cross-section of conventional YSZ after 600 cycles. Coating delamination observed in figure 5.27 was generated close to the bond coat. Moreover, coating surface was continuously spalled during the thermal cycling, producing a removed thickness above 40μm (figure 5.28).

Figure 5.28: Cross-section of conventional YSZ coating at different magnifications (a) 180x, (b) 500, 1000, and 2000x. SEM.

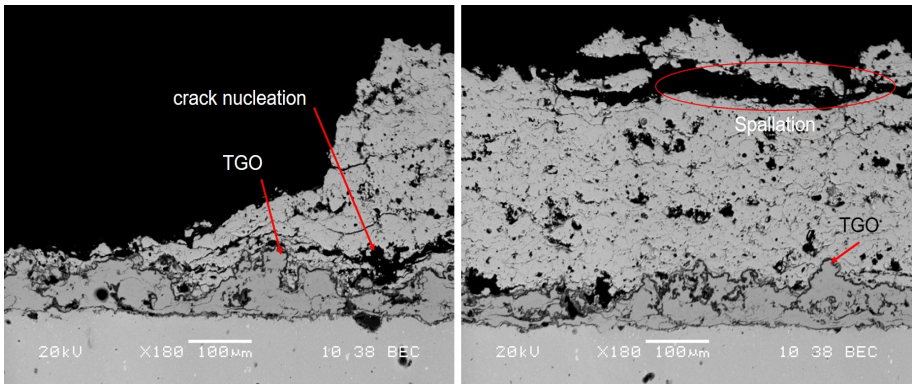

Highly undulated TGO with an average thickness of 2.62$\pm$0.57μm and radial cracks are observed (figure 5.29). This type of TGO together with thermal expansion misfit upon cooling generates the radial cracks [50,115]. These combined with bond and top coat imperfections produce TGO rupture, crack coalescence, coating delamination, and failure.

Figure 5.29: BC/TC interface of YSZ system at 500, 1000, and 2000x. SEM.

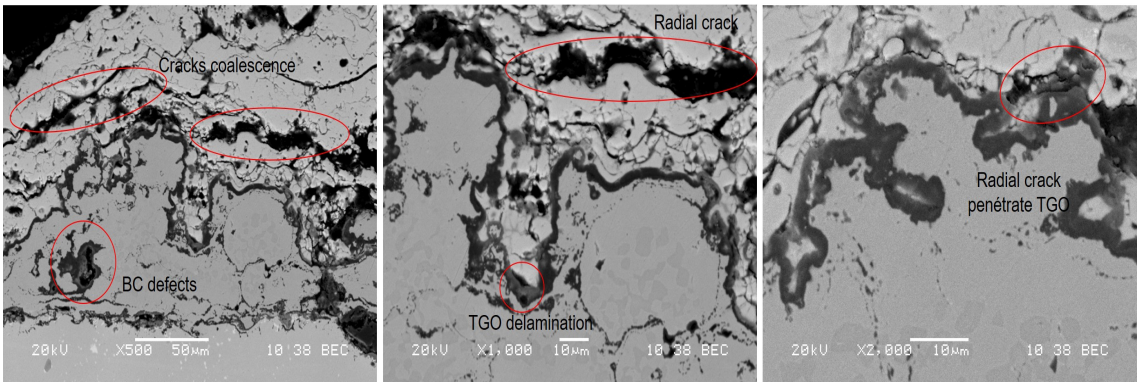

The YSZ system does not present significant changes in its microstructure, where generation of small cracks close to BC and TGO growth are observed (figure 5.30a), these are also evidenced in the systems with D-CYSZ layer. Finally, in figures 5.30b and 5.30c D-CYSZ layers delamination is observed, which was produced by the connection of the vertical cracks and the inter-splat cracks observed in the interface YSZ/D-CYSZ. On the other hand, figure 5.30d shows the CYSZ150 system, where spallation and delamination of D-CYSZ layer occurred. YSZ layers of the systems with D-CYSZ do not present changes in their microstructure, indicating the non-failure of the system.

Figure 5.30: Cross-section of bilayer system after 600 cycles (a) YSZ, (b) CYSZ50, (c) CYSZ100, (d) CYSZ150.

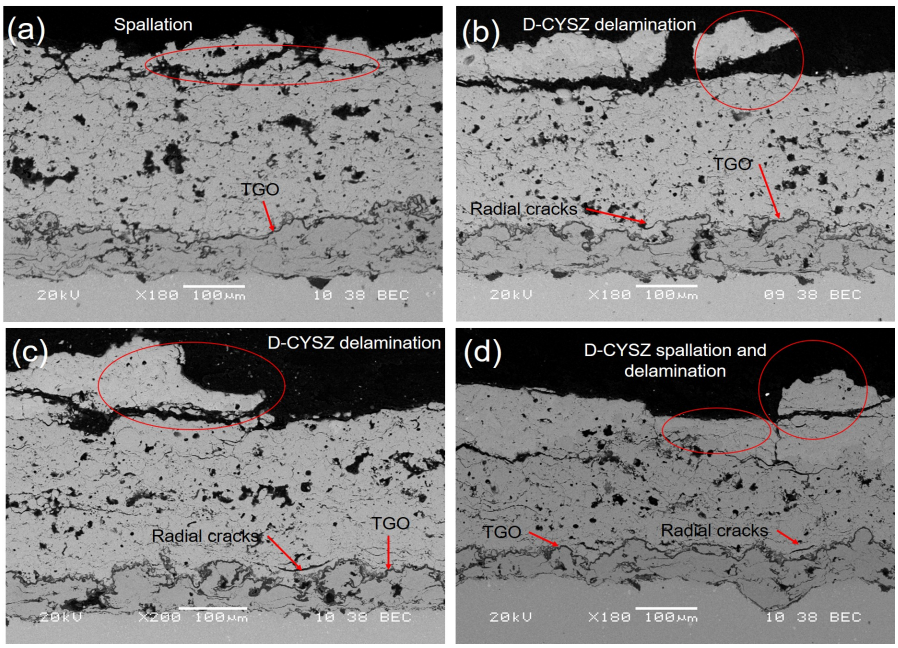

The Analysis of the the BC/TC interface (figure 5.31) reveals that highly undulated TGO is formed in all samples, presenting a thickness of 2.49$\pm$0.75μm, 2.56$\pm$0.42μm, 2.58$\pm$0.48μm, and 2.40$\pm$0.55μm for the samples YSZ, CYSZ50, CYSZ100, and CYSZ150 respectively, which supports the hypothesis that CYSZ layers had no influence on reducing the oxidation of the BC. Radial cracks, TGO rupture and penetration are observed due to stresses generated during thermal shock. Moreover, high oxidation of BC and formation of Ni/Co/Cr oxides (spinels), often associated with internal porosity are observed. Figure 5.31 also shows the reduction of the amount of β-phase (AlNi) precipitates close to TGO, leaving only the presence of γ phase in these zones. Aluminum diffusion in this phase is produced towards TC during thermal exposure, which allows it to react with incoming oxygen to form the TGO [115].

Figure 5.31: TGO analysis of the bilayer systems after 600 cycles (a) YSZ, (b) CYSZ50, (c) CYSZ100, (d) CYSZ150. SEM.

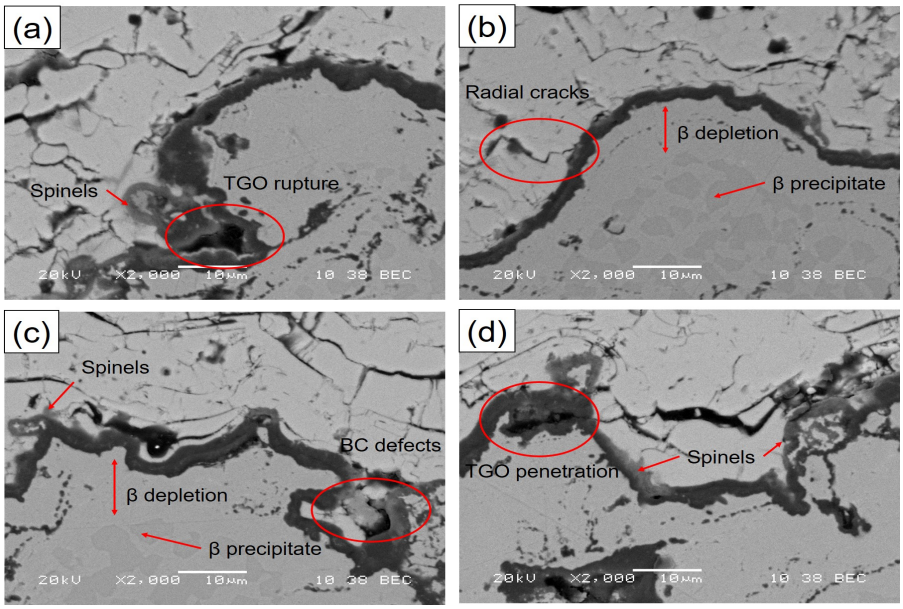

5.4 Hot corrosion (HC) resistance of the D-CYSZ/YSZ systems

5.4.1 HC- Standard

According to the results obtained in section 5.1, it was found that 1 wt.% salt concentration, temperature of 900°C, eutectic salt composition (32 wt.% Na_2SO_4 + 68 wt.% V_2O_5), and 10 hours of exposure were the most aggressive parameters to destabilize the tetragonal phase of YSZ. Figure 5.32 shows the X-Ray diffraction results of the bilayer systems in the as-sprayed condition and after the HC test.

A reduction of the intensity of the main peaks of (101) and (011) planes of the tetragonal phases in the 2θ angles 30.1° and 29.9° for YSZ and CYSZ respectively were observed. The YSZ system presents a bigger intensity reduction compared with CYSZ systems. Moreover, the YSZ system shows the presence of the m-ZrO_2 and YVO_4 phases as a result of

Figure 5.32: X-Ray diffractograms of different D-CYSZ/YSZ system after and before HC test.

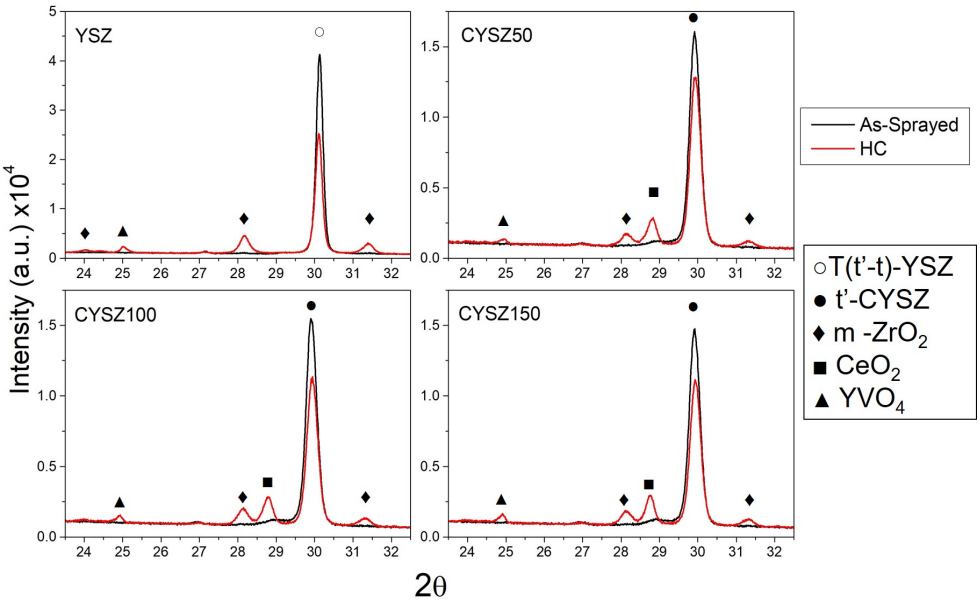

fluxing mechanism that produces yttria depletion (YVO_4 formation) and then tetragonal-to-monoclinic phase transformation. On the other hand, the CeO_2 phase was found in CYSZ systems after HC testing. The interaction of molten salt with CYSZ produces dissolution and then CeO_2 precipitation without chemical reaction, this is called mineralization [10, 22]. Finally, the HC product associated with the ceria ($CeVO_4$) [22, 75] is not observed, because the high ceria's acidity compared with yttria [59, 60] generates a preference of the molten salts to react with the co-stabilizing element, forming the YVO_4 product observed in the diffractograms.

Rietveld quantitative tetragonal phase results of figure 5.33 show a considerable reduction of t'-YSZ phase after the HC test due to yttria depletion.

Figure 5.33: Tetragonal phase content of the samples after hot corrosion tests.

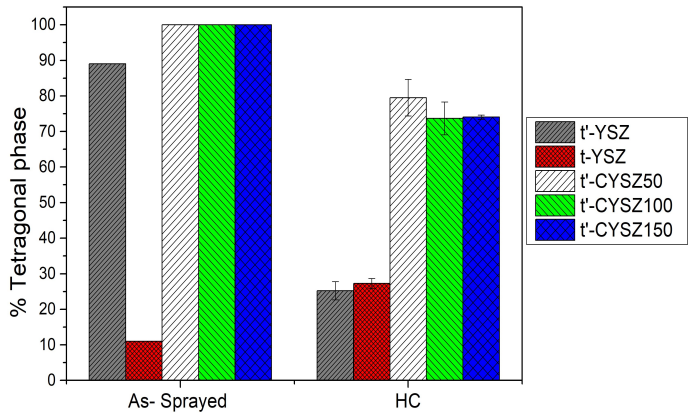

An increment of non-transformable tetragonal (t-YSZ) phase was observed, increasing the possibility to tetragonal-to-monoclinic phase transformation in a subsequent thermal expo-

sure or HC. t'-CYSZ of the bilayer systems present a mild reduction of content compared with YSZ, proving the high HC resistance of this material.

Surface characterization of the bilayers systems is shown in figure 5.34. Rod-type YVO_4 crystals with an average length of 2 μm are observed in the YSZ system. The regions labelled with the letter B in figure 5.8a correspond to monoclinic zirconia.

Figure 5.34: Surface characterization of samples after HC test with 10 hours of exposure (a) YSZ, (b) CYSZ50, (c) CYSZ100, (d) CYSZ150. Rod-type morphology (A), monoclinic zirconia (B), semi-cubic crystals (C).

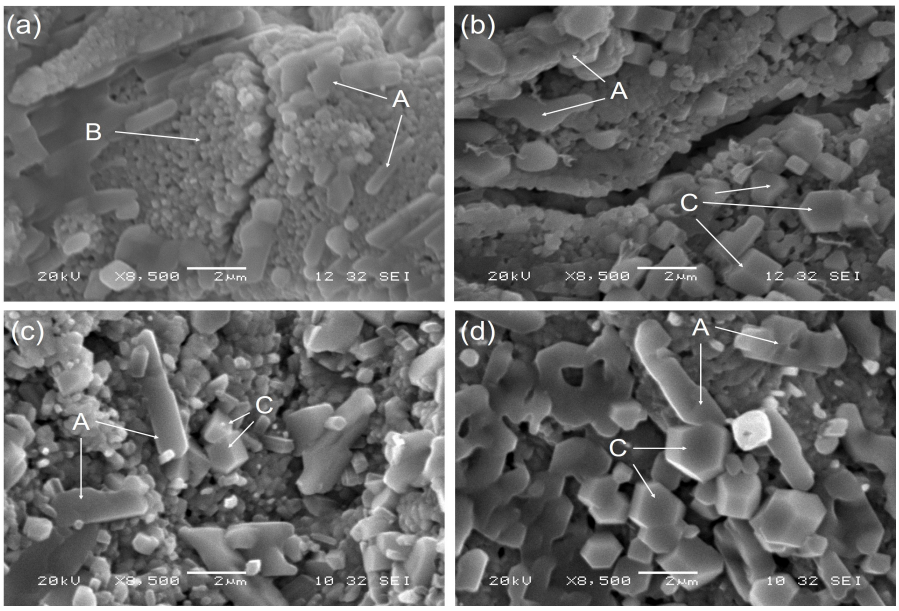

The surface of CYSZ systems (figure 5.34b to 5.34d) also shows the presence of rod-type YVO_4 crystals and semi-cubic CeO_2 crystals (see EDS of figure 5.35), where inside of the crack some of these structures are observed (figure 5.34b) indicating a penetration and interaction of the salt with the coating.

Figure 5.35: EDS spectra of Rod-type and cubic and semi-cubic crystals formed during HC test.

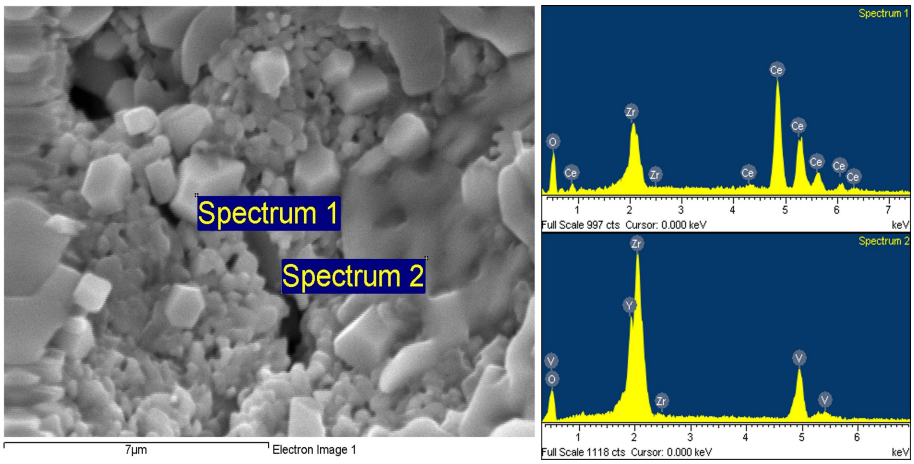

SEM-EDS analysis of the cross-section of the bilayer systems is shown in figure 5.36. Molten salt penetrated the coating thickness using the surface defects (pores and cracks) and vertical cracks for the case of YSZ and CYSZ systems respectively (figure 5.36a).

Figure 5.36: SEM-EDS results of the cross-section of bilayer system (a) salt penetration of YSZ and CYSZ systems, (b) salt penetration close to BC/TC interface.

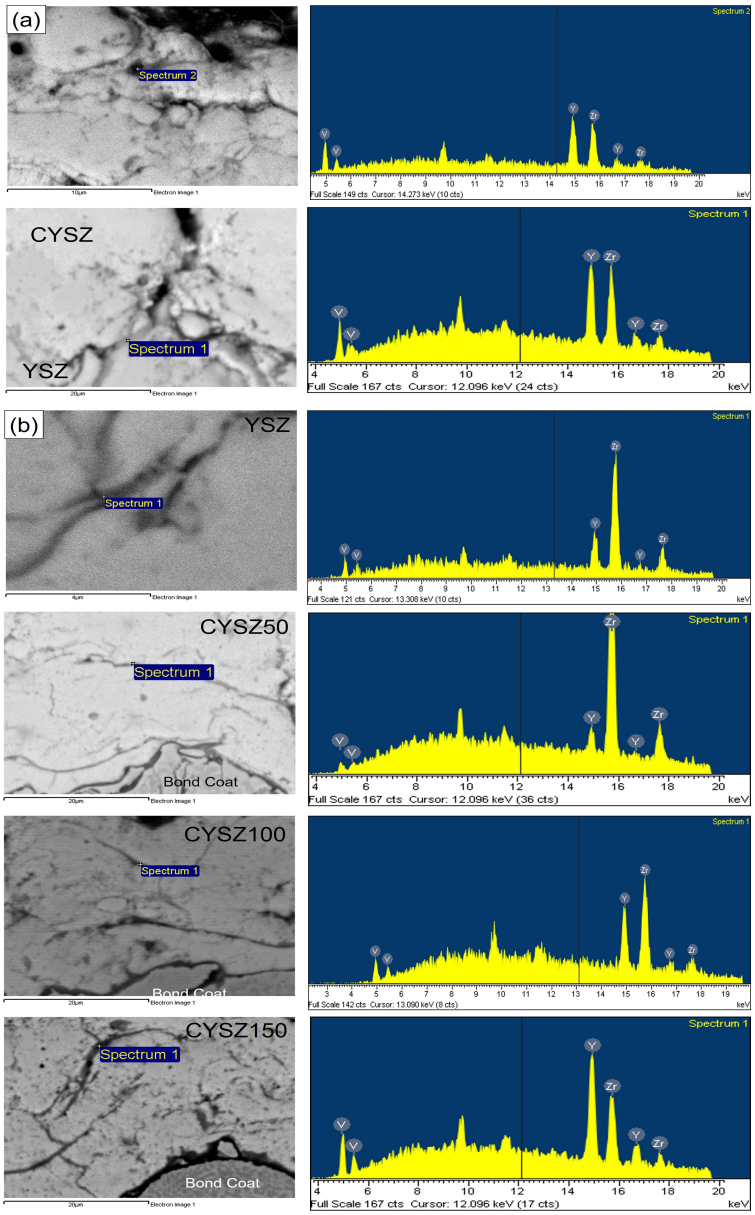

The presence of vanadium and yttrium are observed in the inter-splat cracks and pores close to bond coat (figure 5.36b), indicating penetration of the salts along the entire thickness of the coating. The path of the molten salt was determined by the inter-connectivity between pores and cracks given that no vanadium was detected in the dense areas of the coating. Another evidence of salt penetration is the growth of TGO layer with a thickness of 1 μm approximately, as protection of bond coat against the molten salt attack.

The microstructure of each system is observed in figure 5.37, an evident increment in the porosity as a result of the dissolution of the molten salt in the YSZ layers is observed in all systems, presenting higher damage in the YSZ system. Therefore, the addition of a dense layer offers protection against the HC attack despite the salt penetration that takes place through the top coat.

Figure 5.37: Microstructure of the TBC systems after the hot corrosion test (a) YSZ, (b) CYSZ50, (c) CYSZ100, (d) CYSZ150. LOM.

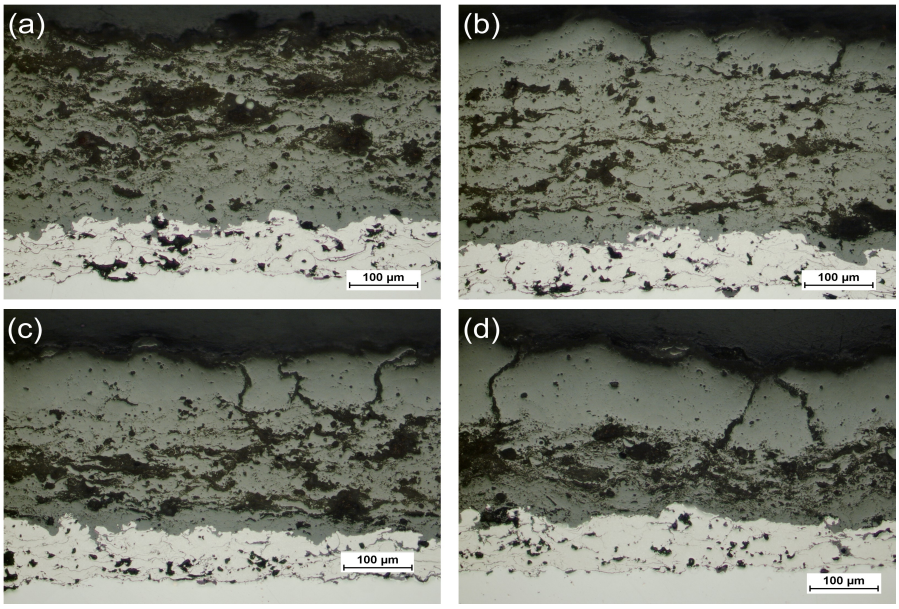

Figure 5.38 shows the Raman spectra of each bilayer system studied in this work.

Figure 5.38: Raman spectroscopy of the bilayer cross-section after HC test.

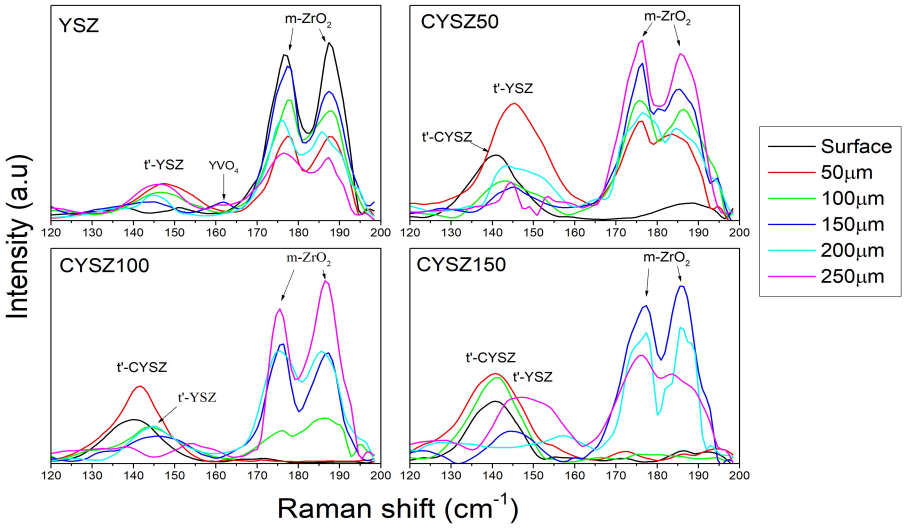

Vibrations of the tetragonal YSZ (145 cm^{-1}) and CYSZ (140 cm^{-1}), monoclinic (182 and 191 cm^{-1}) and YVO_4 (158cm^{-1}) phases for all systems are observed [71,97,116]. Although the molten salt penetrated all the thickness of the bilayer systems, no tendency in phase

intensity was observed. Molten salt penetration through the coating thickness may not be homogeneous and therefore the corrosive attack. However, D-CYSZ layers of the different systems present on the surface and throughout its thickness only the tetragonal phase, so that the layer maintains its phase stability before HC attack.

5.4.2 HC-Concentration

In order to increase the HC attack produced in the previous section, samples were subjected to 3 and 5 wt.% of salt concentration, keeping the rest of the parameters constant. Figure 5.39 shows the X-Ray diffraction results of the bilayer systems with different salt concentration.

Figure 5.39: X-Ray diffractograms of different D-CYSZ/YSZ systems after HC tests with 1, 3 and 5 wt.% of salt concentrations.

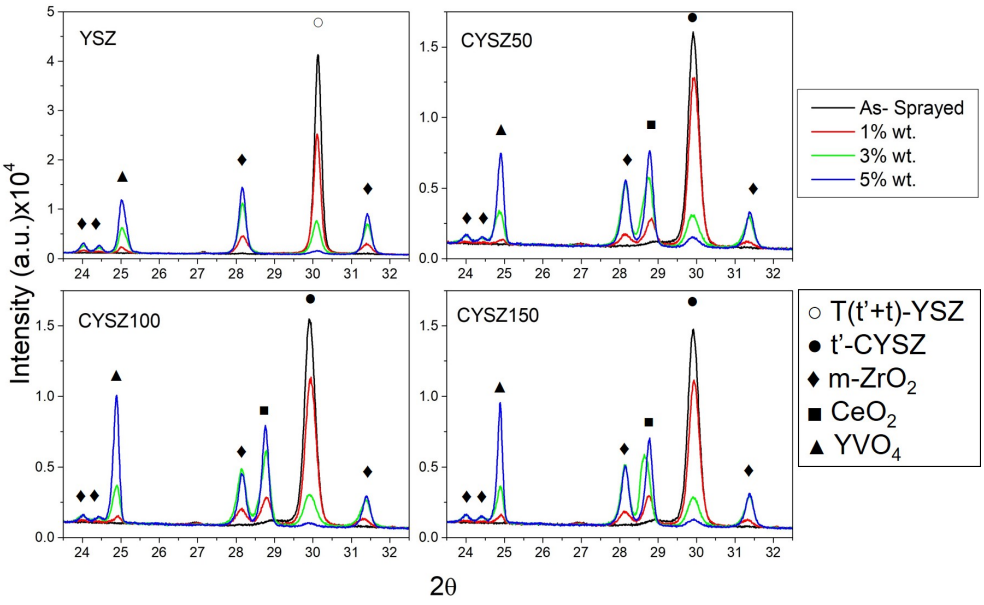

The results show that increasing the salt concentration up to 5 wt.% promotes the tetragonal-to-monoclinic phase transformation. This can be observed with the intensity reduction of the (101) and (011) peaks (2θ= 30.1 and 29.9° for YSZ and CYSZ respectively) of the tetragonal phases, high intensity of the m-ZrO_2 phase characteristic peaks (2θ=28 and 31.5°), and the appearance of new peaks at 2θ=24 and 24.4° of the m-ZrO_2 phase when the salt concentration increases. The transformation occurs because more salt is available to react with the stabilizing compounds (Y_2O_3 and CeO_2), which increases the amount of HC products, as be verified by observing the higher intensity of YVO_4 (2θ=24.9°) and CeO_2 (2θ=28.5°) peaks when the salt concentration is increased.

Quantification results are presented in figure 5.40. A reduction in the content of the tetragonal phases (*t'* and *t* of YSZ and t'-CYSZ) are shown with the increase in salt concentration. For the YSZ sample, *t'* phase disappears when the salt content is up to 3 wt.%, as can be seen in figure 5.40a. Moreover, the protection of the CYSZ layer is observed where the content of the m-ZrO_2 phase (low content of tetragonal phase) of the YSZ system is higher in comparison with CYSZ systems. However, no differences are observed among the systems

Figure 5.40: Phase quantification results of salt concentration tests, (a) tetragonal, (b) HC products.

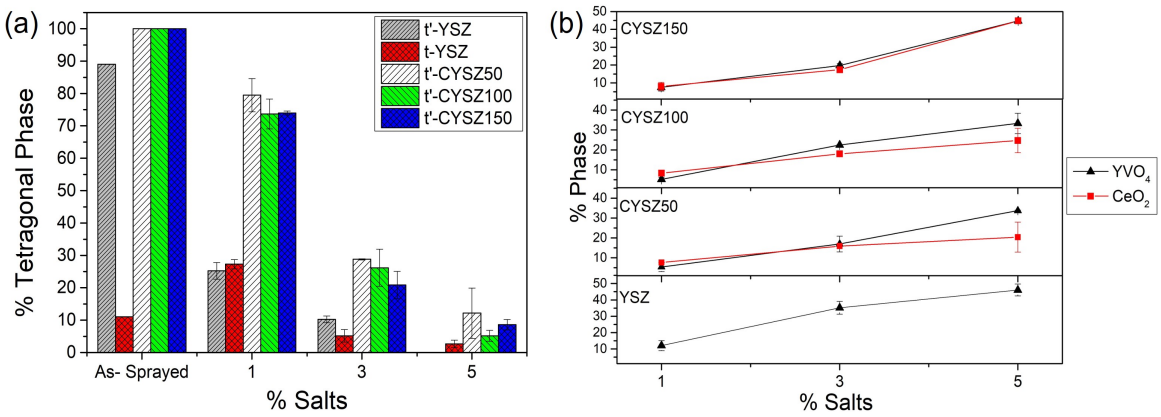

studied with 5 wt.% salt concentration, condition at which all the samples fail. On the other hand, the amount of HC products increase with salt concentration reaching up to 40% for concentration of 5 wt.% as shown in figure 5.40b.

Surface analysis of the bilayer coatings submitted HC tests with 3 wt.% salt concentration is observed in figure 5.41. The YSZ system presents an evident detachment at the edges, which was not observed in CYSZ systems.

Figure 5.41: Morphological analysis of the samples with 3 wt.% salt concentration (a) YSZ, (b) CYSZ50, (c) CYSZ100, (d) CYSZ150. (A) Rod-type, (B) Needle-type, (C) Rods with cubic and semi-cubic crystals, (D) Cubic and semi-cubic crystals, (E) Thick rods.

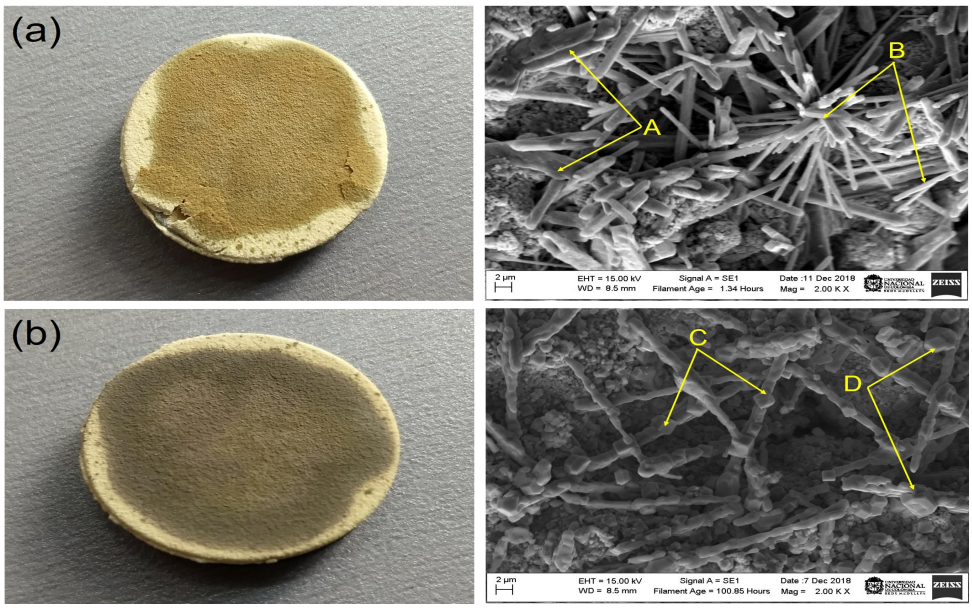

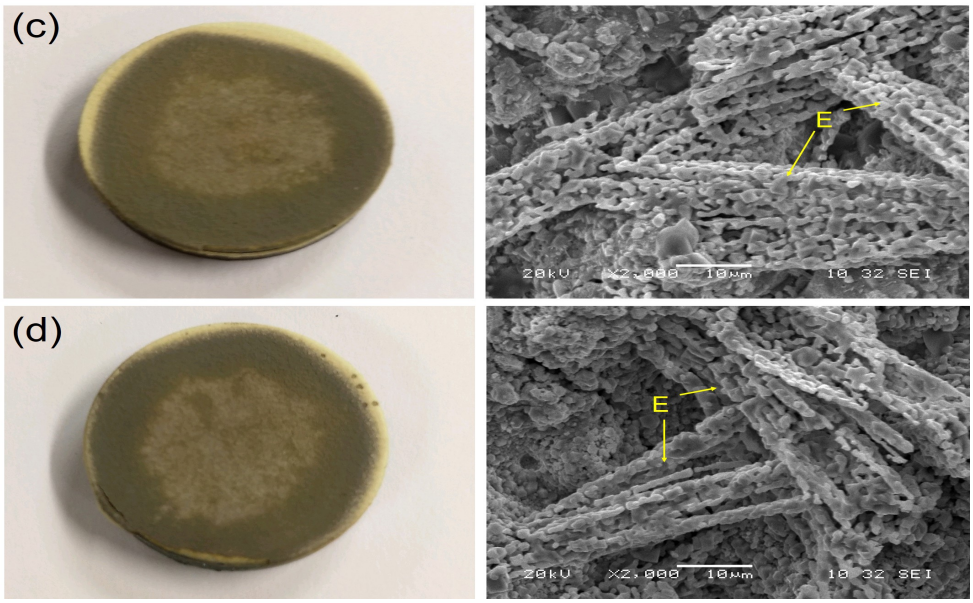

SEM images of the figure 5.41a shows Rod-type and Needle-type morphologies characteristic of YVO_4 crystals with an average length of 13.63$\pm$5.92μm and 7.86$\pm$2.30μm respectively are observed in the YSZ system. On the other hand, the surface of CYSZ systems (figure 5.41b) shows rods held together with cubic and semi-cubic crystals with a average length of 20.29$\pm$3.73μm, and "free" cubic and semi-cubic crystals with a average length of 3.39$\pm$0.58μm. Another rod-type morphology is observed in samples CYSZ100, and CYSZ150, this morphology is a mixture of CeO_2 and YVO_4 phases [74].

EDS mapping of CYSZ surface (figure 5.42) confirm the presence of V, Ce and Y in the rod-type microstructures, indicating that they are a mixture of YVO_4 and CeO_2 crystals, where the cubic and semi-cubic crystals (C and D) are composed of CeO_2 produced by CYSZ mineralization, and the rest are YVO_4 by fluxing mechanism of CYSZ.

Figure 5.42: EDS mapping of the CYSZ surface with 3 wt. % of salt concentration.

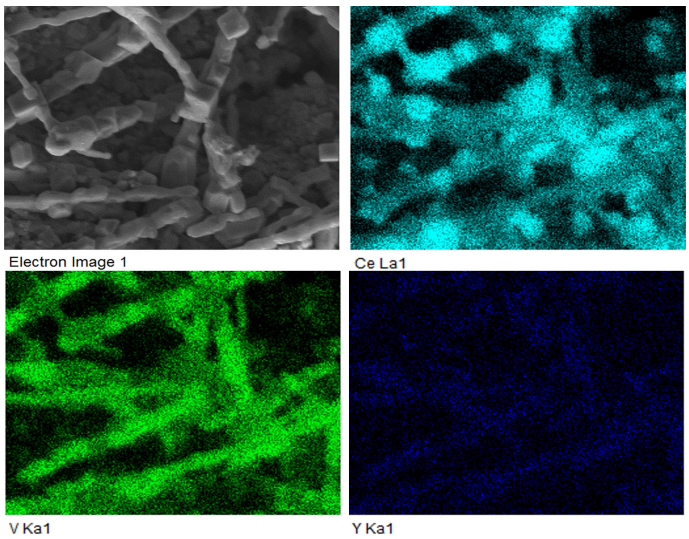

The cross-sectional view of the bilayers tested with to 3 wt.% concentration of salts is shown in figure 5.43.

Figure 5.43: Cross-section and EDS analysis of the samples tested with 3 wt.% of salt concentration (a) YSZ, (b) CYSZ50, (c) CYSZ100, (d) CYSZ150.

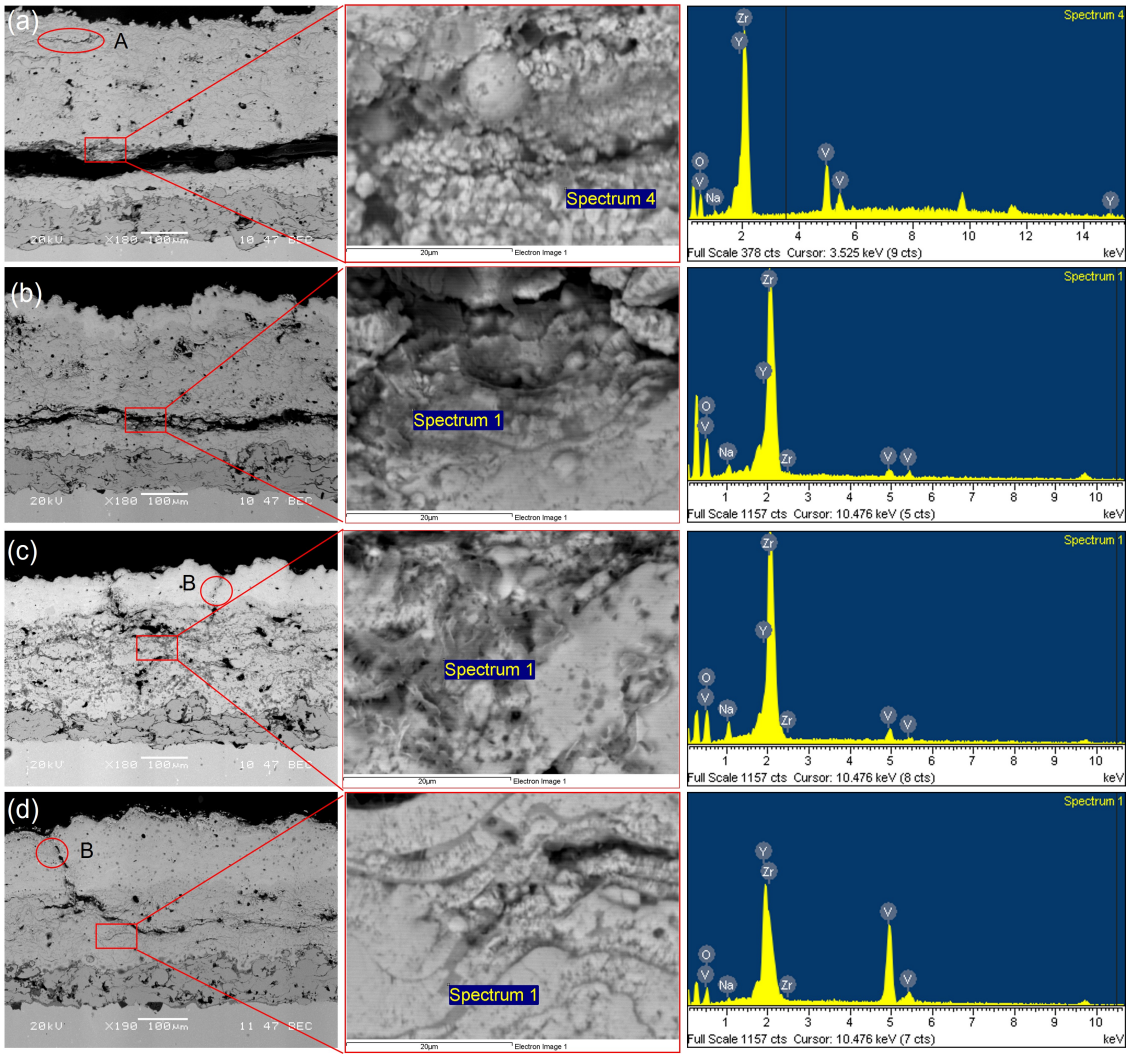

The YSZ system presents a reduction of porosity and inter- and intra-splat cracks. Large cracks (A) close to the coating surface, and total coating delamination mainly at the LP-YSZ/YSZ interface are observed due to the action of molten salts (figure 5.43a). The dark gray areas inside the cracks are rich in vanadium and sodium as observed in the EDS spectra, which confirm the HC mechanisms discussed in the literature [10, 12]. CYSZ systems subjected to this salt concentration (figure 5.43b to figure 5.43d) did not exhibit delamination, spalling, or severe changes in their microstructure. However, the CYSZ50 sample presents cracks inside of the YSZ layer indicating lack of cohesive strength in this layer (which was also observed in the YSZ system) due to attack by salts. In addition, vertical cracks sealing (B) of the D-CYSZ layers product of the dissolution was observed. EDS spectra shows that the cracks and surfaces adjacent to the detachment are rich in V and Y, which indicates the possible formation of HC products in the crack network. These products promote cracking

by phase transformation and increase the levels of internal stresses due to obstruction of the coating's defects (pores and cracks) [12].

Figure 5.44 shows the surface analysis of the bilayer coatings tested with 5 wt.% salt concentration. D-CYSZ layer delamination above 20% of the CYSZ systems and coating spallation and delamination of the YSZ system mainly at the edges are observed. This salt concentration produced a severe attack on the systems tested, generating failure at the interfaces as well as within coating.

Figure 5.44: Surface images of the samples tested with 5 wt.% salt concentration (a) YSZ, (b) CYSZ50, (c) CYSZ100, (d) CYSZ150.

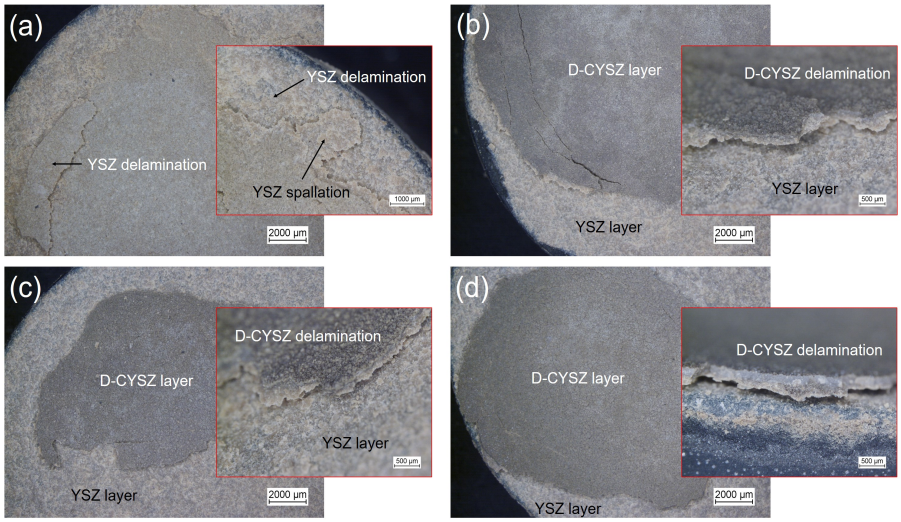

Figure 5.45 shows YSZ system after HC test with a concentration of 5 wt.%.

Figure 5.45: Morphological analysis of bilayer system with 5 wt.% of salt concentration (a) YSZ, (b) CYSZ50, (c) CYSZ100, (d) CYSZ150. (A) Needle-type, (B) Rod-type, (C) Rods mixed cubic and semi-cubic crystals, (D) Cubic and semi-cubic crystals.

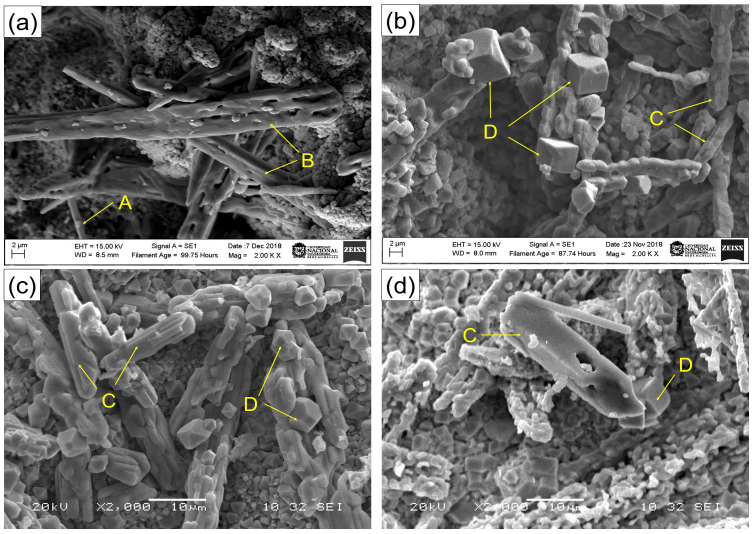

YVO_4 phase shows rod-type with some needle-type morphologies with average length of 49.21$\pm$ 6.37μm. On the other hand, CYSZ systems (figure 5.45) presented rod-type morphologies mixed with cubic and semi-cubic crystals. Rod morphologies characteristic of the YVO_4 phase has a length of 48.75$\pm$10.97μm, and the cubic and semi-cubic crystals characteristic of the CeO_2 phase have average sizes of 7.42$\pm$1.03μm. Elemental analysis (figure 5.46) confirm the composition of the morphologies found. Comparing with the results obtained with the coatings exposed to 3 wt.% concentration, HC products (CeO_2 and YVO_4) in all the systems tested have greater length and thickness, validating the trend presented in the quantification results of X-ray diffraction of figure 5.40.

Figure 5.46: EDS spectra of Rod-type and cubic and semi-cubic crystals.

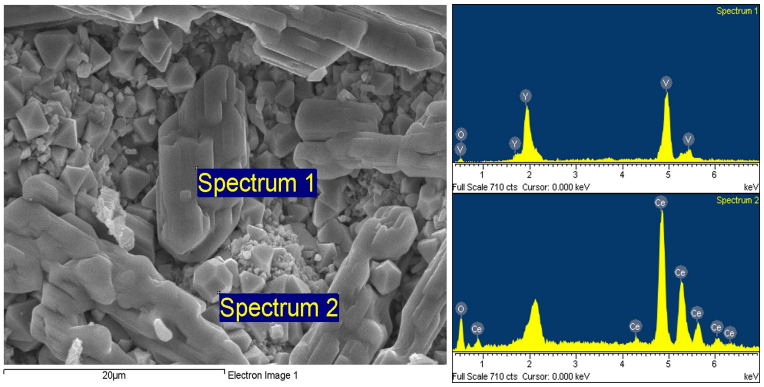

Cross-sections shown in figure 5.47 confirms the delamination and spallation observed at the surface.

Figure 5.47: Cross-section of the samples with 5 wt.% of salt concentration (a) YSZ, (b) CYSZ50, (c) CYSZ100, (d) CYSZ150.

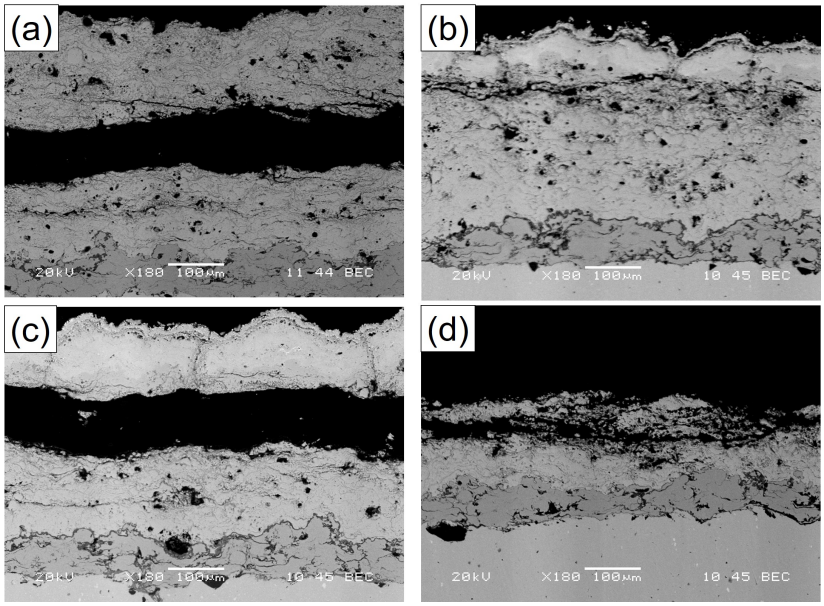

All systems tested shows several changes in their microstructure, even in areas where the system did not fail, as observed in CYSZ50 sample (figure 5.47b). Delamination in YSZ

system is observed close to the LP-YSZ/YSZ interface. On the other hand, in the bilayers system the delamination is presented in the D-CYSZ layer. In addition, the sealing of vertical cracks is more severe than in the samples tested with 3 wt.% salt concentration, indicating more intense coating dissolution and formation of HC products (figure 5.47b and c).

EDS spectra of the figure 5.48a confirms the presence of Y and V in the gray areas within the vertical cracks, indicating a preference to form YVO_4 crystals in the D-CYSZ layer. Finally, the detachment of the bond coat at the edges of the samples was observed in all the tests (figure 5.48b) 5.47b) as a consequence of the dissolution produced by the molten salt [10, 54, 117].

Figure 5.48: Cross-section of the samples tested with 5 wt. % salt concentration (a) vertical crack sealing, (b) BC detachment.

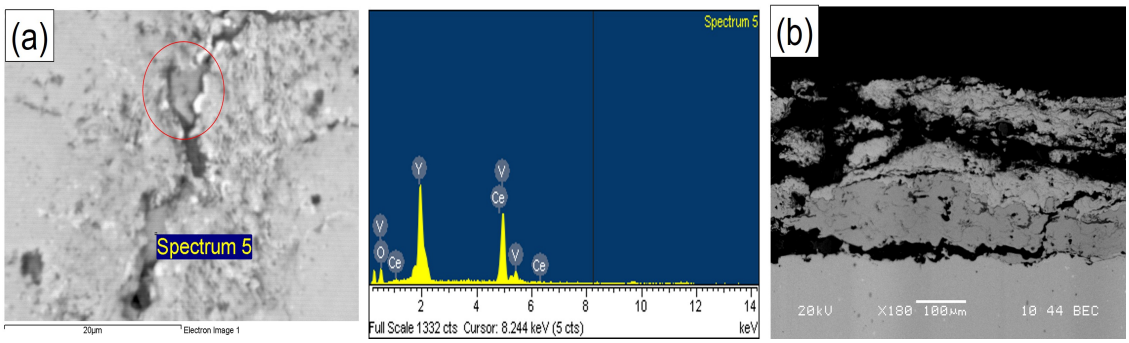

Salt penetration was also observed close to BC/TC interface, where above 3% corrosive processes were generated in the bond coat, as shown in figure 5.49.

Figure 5.49: TGO and BC corrosion after tests with different salt concentrations (a) 3 wt.%, (b) 5 wt.%.

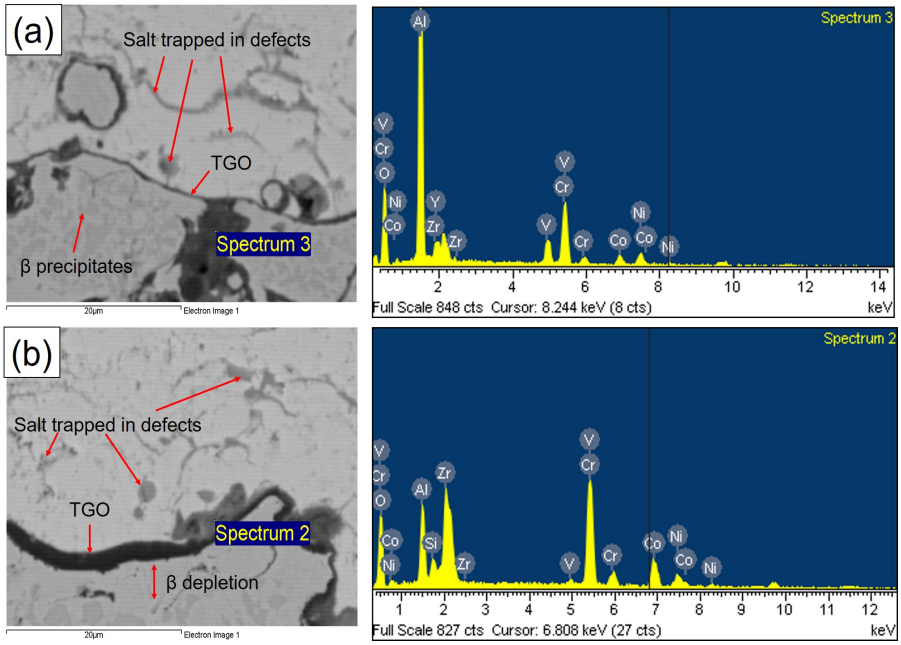

The penetration of the molten salt at the BC/TC interface produced corrosion of the bond coat and accelerated growth of heterogeneous TGO in different areas of the coating, while depletion of β precipitates was observed when thicker TGO was formed. The EDS spectra show the presence of vanadium in the TGO, which promotes the coating failures observed in previous results (figures 5.43 and 5.47).

The analysis of the back-side of the detached layers (figure 5.50) revealed the typical morphology of corrosion products. Cubic and semi-cubic crystals (figure 5.50a) of CeO_2 phase and characteristic rod-type morphology of YVO_4 phase (figure 5.50b) were observed and their chemical composition was confirmed by EDS. This agrees with reports by Jones, Levi, Park, Daroonpavar [10,12,22,65], among others, where the corrosion products are formed in the coating defects, decreasing the compliance and generating mechanical stresses, which promote cracking and delamination of the coating.

Figure 5.50: Hot corrosion products found in the back-side of detached layer (a) CeO_2, (b) YVO_4.

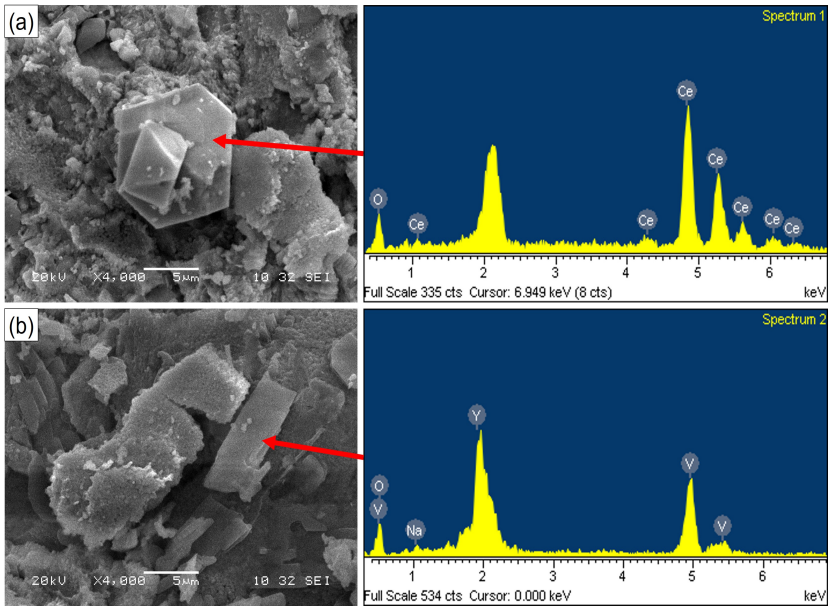

5.4.3 HC-Cycles

In this test, the samples were taken out of the furnace after every 10 hours of exposure to hot corrosion in order to add fresh salts to keep the kinetics of the corrosive attack. Figure 5.51 shows the X-ray diffractograms of the D-CYSZ/YSZ system after every cycle.

A progressive reduction of the main peak intensity of the planes (101) and (011) at 2θ=30.1 and 29.9° of the tetragonal phases (YSZ and CYSZ respectively) and an increment in the peak intensities of the HC products (YVO_4 and CeO_2), and m-ZrO_2 phase are observed when increases the cycles. YSZ system shows larger destabilization compared with CYSZ systems in each cycle, showing the greater resistance of D-CYSZ layer against HC attack. In addition, no coating detachment in cycle 5 was observed even with the salt concentration of 5 wt.% and after the complete destabilization of the tetragonal phases occurred. Quantitative analysis of figure 5.52 yields the presence of 100% tetragonal phases (*t'*+*t* for

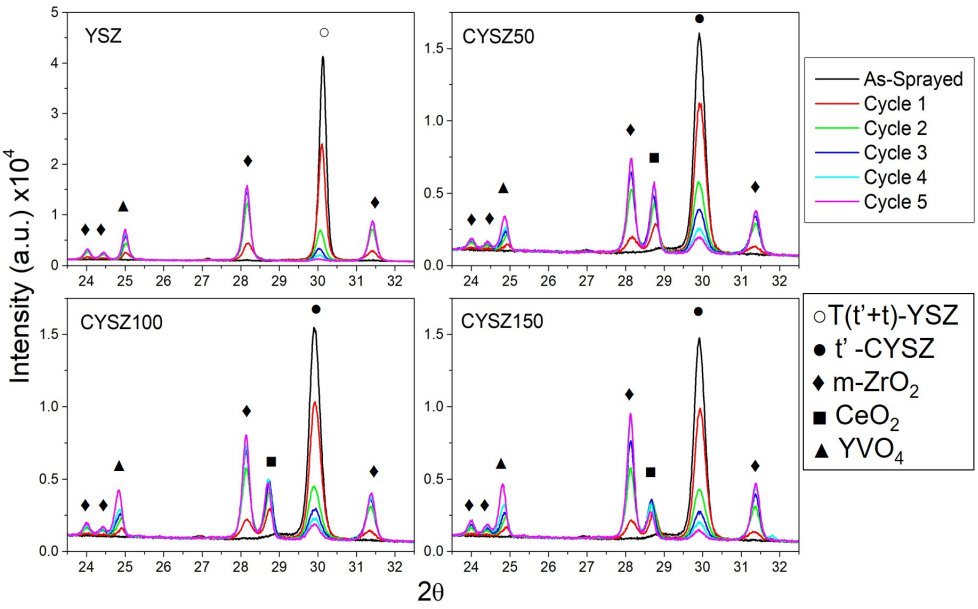

Figure 5.51: X-Ray diffractograms of the D-CYSZ/YSZ system submitted to Hot corrosion cycles.

YSZ and *t'* for CYSZ) for the as-sprayed samples. By increasing the number of cycles, the tetragonal phase content of the different systems decrease because of the coating dissolution and depletion of stabilizing elements, where the CYSZ50 system has better resistance in the first cycles (figure 5.52a). For the YSZ system, the *t'* phase disappears from cycle 4 leaving only phase *t*, being the material more prone to tetragonal-to-monoclinic phase transformation. From cycle 4 on, the amount of tetragonal phase is less than 20% indicating failure in all samples.

Figure 5.52: Phase quantification results of hot corrosion cycles, (a) tetragonal, (b) HC products.

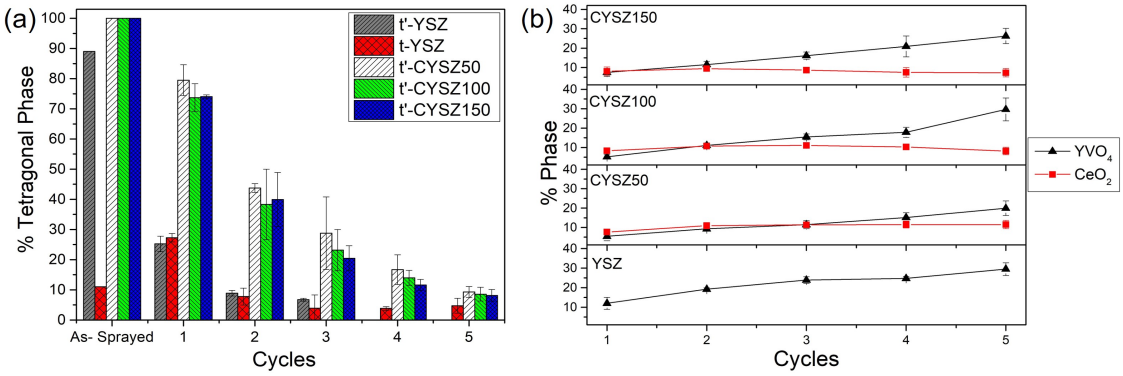

Figure 5.52b shows that the amount of YVO_4 increases linearly with the cycles for the YSZ system. CYSZ systems show an increase in the CeO_2 percentage with the number of cycles up to 11% (CYSZ50), then it remains constant. This behavior can be attributed to a "stand-still effect" during each exposure. In the first cycle, the molten salt penetrates the coating, interacts with the material and produces HC products and m-ZrO_2. At the beginning of cycle 2, the freshly added salt interacts with a system composed by corrosion products (with a high melting point), monoclinic zirconia, and a coating with a depletion of stabilizing com-

pounds (Y_2O_3 and CeO_2), becoming a dynamic system where the chemistry is different in each cycle. The low availability of stabilizing elements and the presence of other compounds on the surface, change the morphology and quantity of the corrosion products, where the amount of YVO_4 phase increases linearly and CeO_2 phase remains constant with the cycles.

Figure 5.53 shows the surface of the bilayer systems after HC-Cycles test. YSZ system presents needle-type morphology (A) with sizes from 10 to 90 μm approximately. Compare the results observed in figure 5.44, where the samples (cycles and concentration) have the same salt concentration (5 wt.%), YVO_4 crystals of the cycle tests have a smaller thickness, but greater quantity and length. On the other hand, CYSZ systems have needle-like morphology with an average length of 13.98$\pm$3.82μm dispersed throughout the surface of the coating (figures 5.53b to 5.53d). In addition, some cubic and semi-cubic crystals (B) are distinguished from the CeO_2 phase at high magnifications (figures 5.53c and d), confirming the results of XRD and the stagnation of the CYSZ mineralization mechanism.

Figure 5.53: Surface characterization of bilayer systems after 5 cycles (a) YSZ, (b) CYSZ50, (c) CYSZ100, (d) CYSZ150.

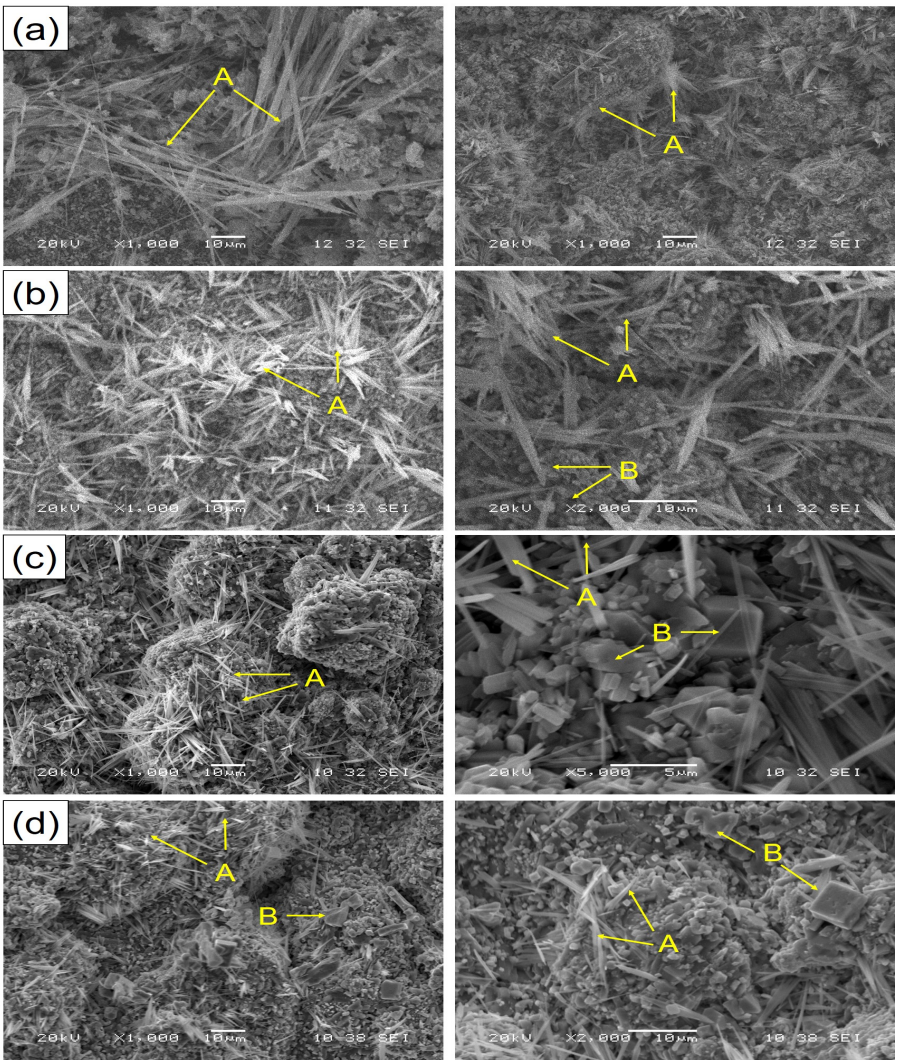

SEM-EDS mapping of the cross-section of the bilayer systems are observed in the figure 5.54. Mapping shows the presence of vanadium over to approximately 200μm of the thickness of all systems, indicating penetration of the molten salt.

Figure 5.54: SEM/EDS results of the cross-section of bilayer system after HC test (a) YSZ, (b) CYSZ50, (c) CYSZ100, (d) CYSZ150.

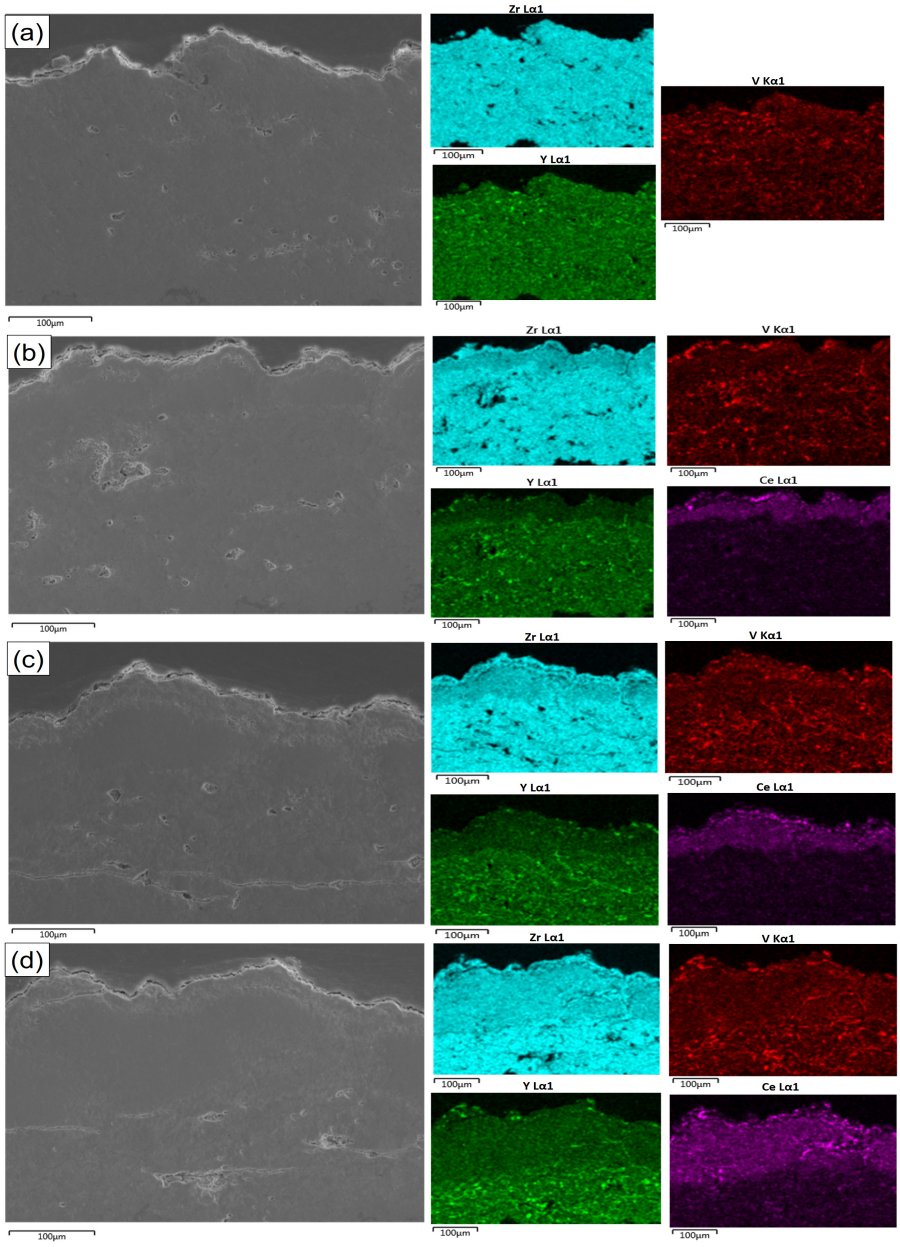

As observed in previous results, the path used by the salt to penetrate the bilayer was the pores and cracks of the different layers. Defects are observed in dark points of Zr map, which coincide with higher concentration of V, Y and Ce points suggesting a formation of HC-products (YVO_4 and CeO_2) and possible phase destabilization, this can be observed in figure 5.55. In addition, the presence of cerium of to the dense layer is observed, corroborating the thickness of the different systems (50, 100 and 150μm respectively).

Figure 5.55: EDS maps with higher magnifications of the cross-section of CYSZ systems.

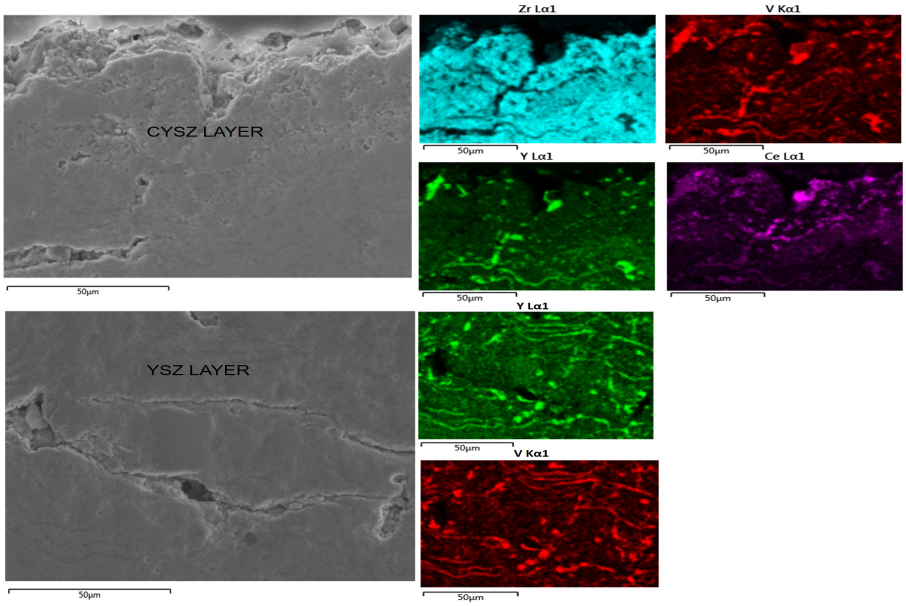

Figure 5.56 shows the microstructure of the bilayer systems after HC-cycles test. In some areas, YSZ system presents severe cracking without delamination or spallation. Moreover, this system loses its characteristic microstructure (observed in figure 5.18), where only some pores are observed along the thickness, this is also showed in the YSZ layers of CYSZ systems. D-CYSZ layers present a loss of thickness and sealing of vertical cracks. The change in the bilayer microstructure is produced by the fluxing (dissolution) of coating by the reaction with the salts [9] and solidification of the molten salts and formation of HC products in the coating defects.

Figure 5.56: Microstructure of the bilayer systems submitted to HC cycles.

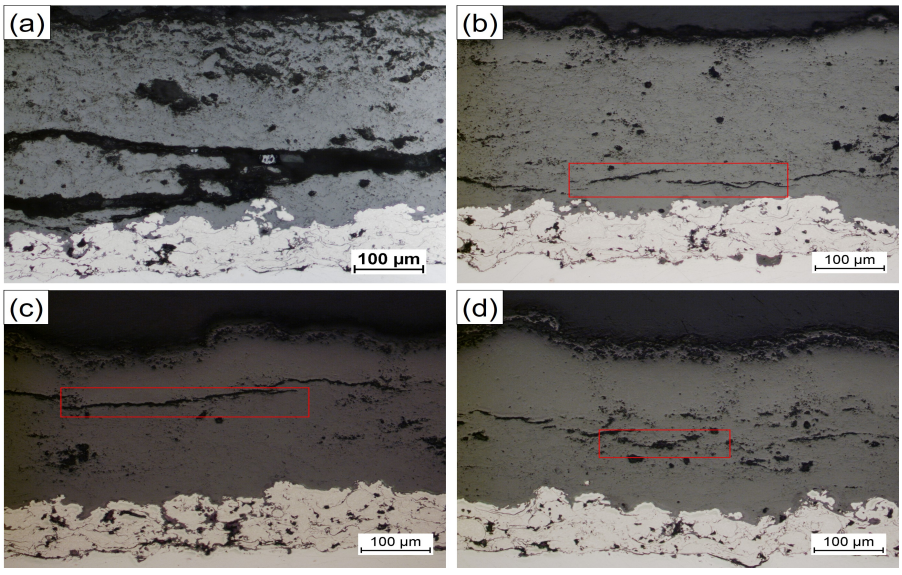

As observed in previous results, the path used by the molten salt was the pores and cracks

to penetrate the coating, sealing the defects and dissolved the material. Moreover, despite having the same salt concentration of the test of the previous section (HC-concentration 5 wt.%), coating delamination and spallation were no observed in all systems. Only cracks were observed throughout the coating thickness (see red box in figure 5.56) being more severe in the YSZ system (figure 5.56a). The fact of not observing any detachment of the coatings is due to the "stagnation effect". At the beginning of the test, the incoming molten salt reacted inside of the coating and started with the sealing of the defects (salt and HC products trapped into defects), preventing the ingress of new molten salt in the subsequent cycles, avoiding new reactions and generation more corrosion products. However, the presence of salt into coating defects generate a cohesive weakness which is reflected in the cracking of the YSZ system. This indicates that the addition of the D-CYSZ layer provides protection against salt attack, since cohesive weakness is less than the YSZ system. Unlike the HC-concentration test, a large amount entered the system generating the processes of dissolution, the formation of corrosion products and phase transformation described above, which produced a failure of the coating with a concentration of 3 wt.%.

Figure 5.57: TGO and BC corrosion of the bilayer systems after HC-Cycles (a) YSZ, (b) CYSZ50, (c) CYSZ100, (d) CYSZ150.

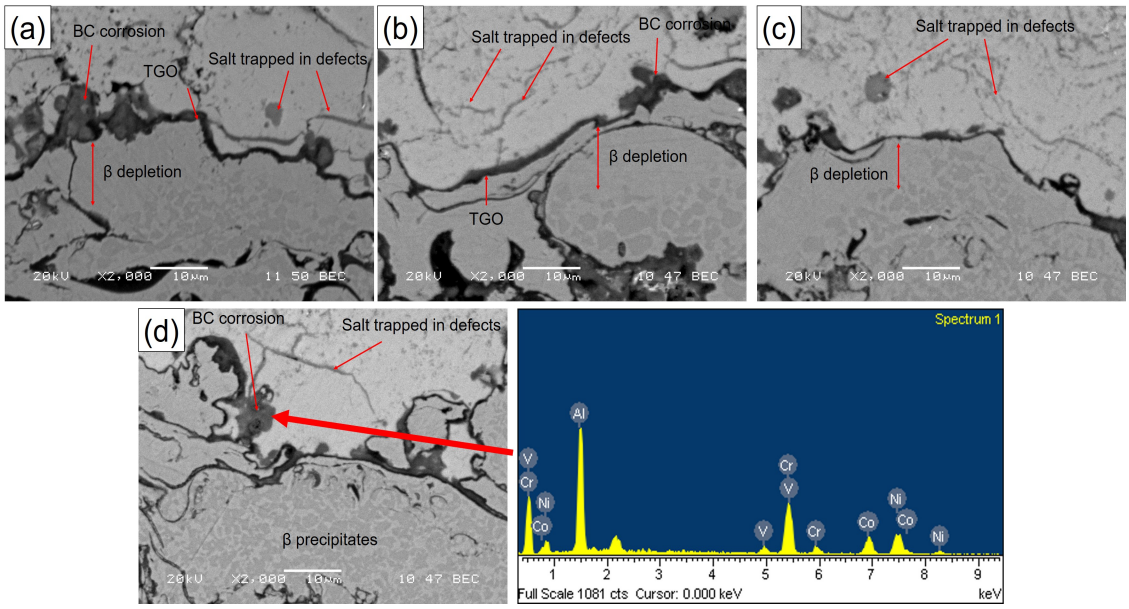

Figure 5.57 shows the BC/TC interface of the systems tested after the HC-Cycles test. TGO growth with different thicknesses can be observed together with the β-depletion in some areas. The presence of salt induces the TGO growth and BC corrosion as shown in figure 5.57d. EDS spectrum confirms the presence of vanadium in the gray areas of the back-scattered image, where TGO and other oxides formation is accelerated and irregular. These are fragile points that under a mechanical or thermo-mechanical stress, can produce delamination and failure of the coating.

Figure 5.58 shows the Raman spectra of the cross-section of the systems studied. YSZ system shows the vibrations of m-ZrO_2 and YVO_4 phases on the surface and along with the thickness. These are decreasing as it is approached to the BC, where there is the presence vibration at 148cm^{-1} of the tetragonal phase [71, 97].

Figure 5.58: Raman cross-section of bilayer systems after 5 cycles (a) YSZ, (b) CYSZ50, (c) CYSZ100, (d) CYSZ150.

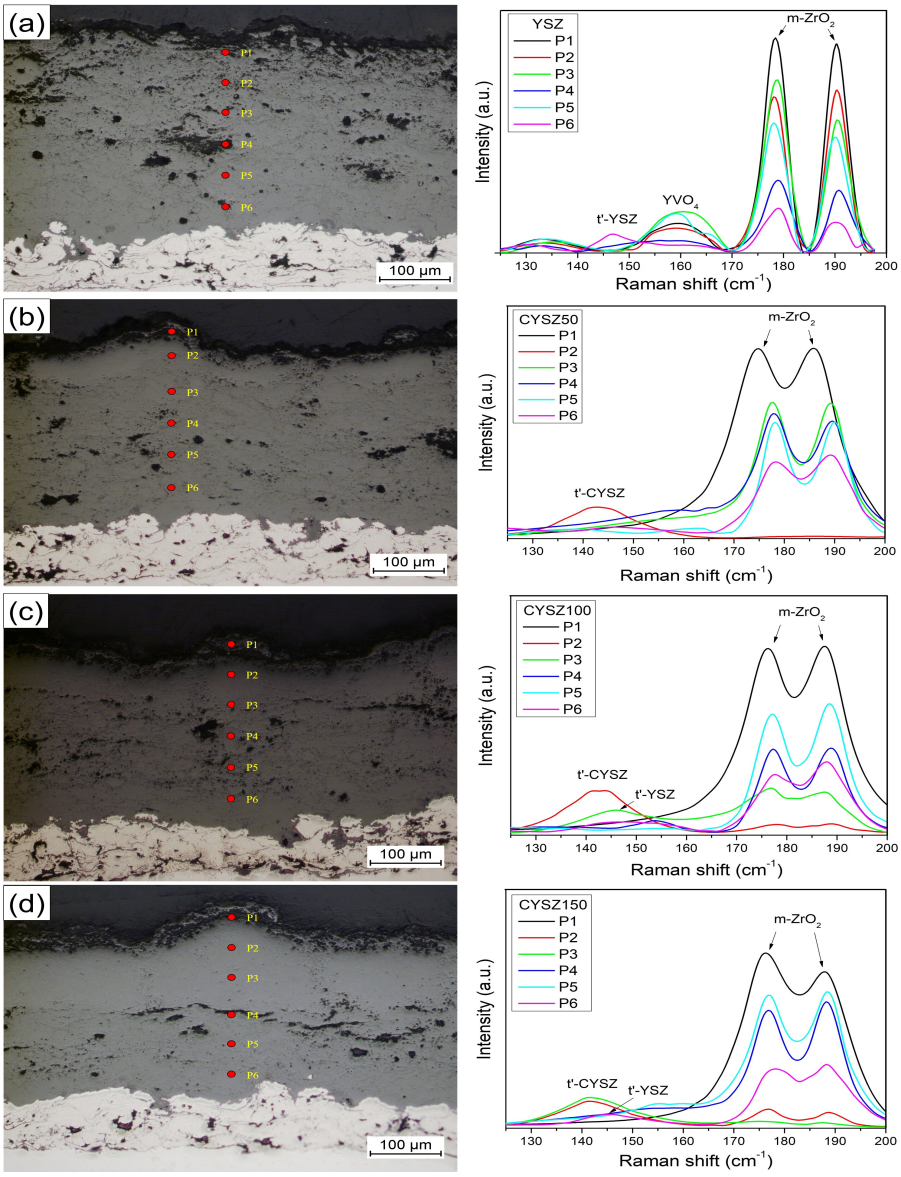

CYSZ systems present a high phase destabilization in the surface due to the reaction with the salts (as was observed in the XRD results). However, no phase transformation is observed inside of the coating, since they present vibrations of the tetragonal phase. On the other hand, YSZ layers of the CYSZ systems do not present vibrations corresponding to HC products at 158cm^{-1} [71]. In addition, samples CYSZ100 and CYSZ150 showed vibrations of the tetragonal phase, indicating that the CYSZ layers offered protection against attack by molten salts.

6 | Conclusions

Molten salt attack experiments performed on yttria-stabilized zirconia powders show that the use of the eutectic composition of the salt mixture (32 wt.% Na_2SO_4 + 68 wt.% V_2O_5) and 1 wt.% of salt concentration led to the most aggressive HC conditions at 1000°C. This is because higher amounts of Na_2SO_4 reduce melt acidity and its capacity to react with yttria, according to the Lewis mechanism. SO_3 evaporation is responsible for the dissolution of the samples in HC tests at different temperatures, because it reduces V_2O_5 activity and promotes less HC attack at higher temperatures.

The protocols and conditions for plasma spraying the NiCoCrAlY, YSZ, LP-YSZ, D-CYSZ layers were properly defined. The variation of the H_2 flow at the tested levels had no influence on the crystal structure of the YSZ coatings. On the other hand, the current has a strong influence to reduce the porosity of the deposited coatings (LP-YSZ and D-CYSZ), due to the larger enthalpy that is provided to the particles. The systems studied showed an adhesive-cohesive strength within the values reported in the literature and required in the industry. This indicates that a good spay protocol was developed, which is suitable for the production of TBC coatings and with the possibility to be scaled for gas turbine components.

A D-CYSZ/YSZ bilayer system was obtained with the desired thicknesses and the proposed microstructure. The D-CYSZ layer showed vertical cracks due to the stresses generated by the YSZ layer during the spraying process. The crack density of the layers was 4.32, 3.87, 3.19 cracks/mm for samples CYSZ50, CYSZ100 and CYSZ150 respectively, values that provide good thermal shock resistance of the coatings.

The addition of a Low Porosity- YSZ layer (LP-YSZ) layer in a TBC system increased the thermal shock resistance, due to a major cohesion between splats that increases the stiffness in the BC/TC interface, providing resistance against stresses produced by external factors, thermal expansion misfit, and irregular growth of TGO.

The hot corrosion (HC) results of the D-CYSZ/YSZ bilayer systems showed that increase the salt concentration promotes a higher corrosive attack, where from 3 wt.% salt concentration delamination of the coating and severe microstructural changes were observed. On the other hand, a progressive increment in the salt concentration (cycling test) led to changes in the HC products morphology generated on the surface, and the systems do not presented coating delamination. This is attributed to a "stagnation effect" due to the chemical dynamics generated by each cycle, which produces gradual damage to the TBC system. Moreover, the D-CYSZ layer provides protection against HC attack despite the formation of vertical cracks. This protection was observed in the HC-concentration and HC-cycles tests,

in which the YSZ system presented coating delamination from 3 wt.% salt concentration, and greater cohesive weakness after 5 cycles.

According to the results obtained in this work, introducing a dense layer with a thickness between 100 to 150μm over a YSZ coating increases the HC resistance without reducing its performance as thermal barrier. These samples showed less infiltration of molten salts and less cohesive weakness in the YSZ coating than the system without a dense layer. Besides, dense coatings exhibited competitive thermal shock resistance compared to porous YSZ coatings, indicating that the layer can resist typical operating demands other than HC.

Bibliography

[1] Revista Dinero. ¿Qué tan competitiva es la energía colombiana?, 2015.

[2] David R Clarke and Simon R Phillpot. Thermal barrier coating materials. *Materials Today*, 8(6):22–29, 2005.

[3] Canan U Hardwicke and Yuk-Chiu Lau. Advances in thermal spray coatings for gas turbines and energy generation: a review. *Journal of Thermal Spray Technology*, 22(5):564–576, 2013.

[4] David R Clarke, Matthias Oechsner, and Nitin P Padture. Thermal-barrier coatings for more efficient gas-turbine engines. *MRS bulletin*, 37(10):891–898, 2012.

[5] Nitin P Padture, Maurice Gell, and Eric H Jordan. Thermal barrier coatings for gas-turbine engine applications. *Science*, 296(5566):280–284, 2002.

[6] Nitin P Padture. Advanced structural ceramics in aerospace propulsion. *Nature materials*, 15(8):804–809, 2016.

[7] Wei Pan, Simon R Phillpot, Chunlei Wan, Aleksandr Chernatynskiy, and Zhixue Qu. Low thermal conductivity oxides. *MRS bulletin*, 37(10):917–922, 2012.

[8] LB Chen. Yttria-stabilized zirconia thermal barrier coatings—a review. *Surface Review and Letters*, 13(05):535–544, 2006.

[9] Narender Reddy and Ashutosh S Gandhi. Molten salt attack on t' yttria-stabilised zirconia by dissolution and precipitation. *Journal of the European Ceramic Society*, 33(10):1867–1874, 2013.

[10] Robert L Jones. Some aspects of the hot corrosion of thermal barrier coatings. *Journal of Thermal Spray Technology*, 6(1):77–84, 1997.

[11] Imran Nazir Qureshi, Muhammad Shahid, and A Nusair Khan. Hot Corrosion of Yttria-Stabilized Zirconia Coating, in a Mixture of Sodium Sulfate and Vanadium Oxide at 950 °C. *Journal of Thermal Spray Technology*, 25(3):567–579, 2016.

[12] Mohammadreza Daroonparvar, Muhamad Azizi Mat Yajid, Noordin Mohd Yusof, Hamid Reza Bakhsheshi-Rad, Esah Hamzah, and Mohsen Nazoktabar. Investigation of three steps of hot corrosion process in Y_2O_3 stabilized ZrO_2 coatings including nano zones. *Journal of Rare Earths*, 32(10):989–1002, 2014.

[13] Tao Liu, Shu-Wei Yao, Li-Shuang Wang, Guan-Jun Yang, Cheng-Xin Li, and Chang-Jiu Li. Plasma-sprayed thermal barrier coatings with enhanced splat bonding for CMAS and corrosion protection. *Journal of Thermal Spray Technology*, 25(1-2):213–221, 2016.

[14] Pablo Carpio, M Dolores Salvador, Amparo Borrell, Lucia Navarro, and Enrique Sánchez. Molten salt attack on multilayer and functionally-graded YSZ coatings. *Ceramics International*, 44(11):12634–12641, 2018.

[15] M Mohammadi, A Kobayashi, S Javadpour, and SAJ Jahromi. Evaluation of hot corrosion behaviors of Al_2O_3-YSZ composite TBC on gradient MCrAlY coatings in the presence of Na_2SO_4-$NaVO_3$ salt. *Vacuum*, 167:547–553, 2019.

[16] MH Habibi, Li Wang, and SM Guo. Evolution of hot corrosion resistance of YSZ, $Gd_2Zr_2O_7$, and $Gd_2Zr_2O_7$+ YSZ composite thermal barrier coatings in Na_2SO_4+ V_2O_5 at 1050 °C. *Journal of the European Ceramic Society*, 32(8):1635–1642, 2012.

[17] Yasin Ozgurluk, Kadir Mert Doleker, and Abdullah Cahit Karaoglanli. Hot corrosion behavior of YSZ, $Gd_2Zr_2O_7$ and YSZ/$Gd_2Zr_2O_7$ thermal barrier coatings exposed to molten sulfate and vanadate salt. *Applied Surface Science*, 438:96–113, 2018.

[18] Yichuan Yin, Wen Ma, Xilong Jin, Xiaoying Li, Yu Bai, Ruiling Jia, and Hongying Dong. Hot corrosion behavior of the $La_2(Zr_{0.7}Ce_{0.3})_2O_7$ ceramic in molten V_2O_5 and a Na_2SO_4+ V_2O_5 salt mixture. *Journal of Alloys and Compounds*, 689:123–129, 2016.

[19] Mohammad Reza Loghman-Estarki, Mehrdad Nejati, Hossein Edris, Reza Shoja Razavi, Hossein Jamali, and Amir Hossein Pakseresht. Evaluation of hot corrosion behavior of plasma sprayed scandia and yttria co-stabilized nanostructured thermal barrier coatings in the presence of molten sulfate and vanadate salt. *Journal of the European Ceramic Society*, 35(2):693–702, 2015.

[20] MH Habibi, Shizhong Yang, and SM Guo. Phase stability and hot corrosion behavior of ZrO_2–Ta_2O_5 compound in Na_2SO_4-V_2O_5 mixtures at elevated temperatures. *Ceramics International*, 40(3):4077–4083, 2014.

[21] MH Habibi, Li Wang, Jiandong Liang, and SM Guo. An investigation on hot corrosion behavior of YSZ-Ta_2O_5 in Na_2SO_4+V_2O_5 salt at 1100 °C. *Corrosion Science*, 75:409–414, 2013.

[22] SY Park, JH Kim, MC Kim, HS Song, and CG Park. Microscopic observation of degradation behavior in Yttria and Ceria stabilized zirconia thermal barrier coatings under hot corrosion. *Surface and Coatings Technology*, 190(2):357–365, 2005.

[23] YS Hwang and RA Rapp. Thermochemistry and solubilities of oxides in sodium sulfate-vanadate solutions. *Corrosion*, 45(11):933–937, 1989.

[24] XQ Cao, R Vassen, and D Stoever. Ceramic materials for thermal barrier coatings. *Journal of the European Ceramic Society*, 24(1):1–10, 2004.

[25] Joseph R Davis. *Handbook of thermal spray technology*. ASM international, 2004.

[26] Klaus Erich Schneider, Vladimir Belashchenko, Marian Dratwinski, Stephan Siegmann, and Alexander Zagorski. *Thermal spraying for power generation components*. John Wiley & Sons, 2006.

[27] P Fauchais, J Heberlein, and M Boulos. *Thermal spray thermal spray fundamentals*. Springer, Berlin, 2014.

[28] Lech Pawlowski. *The science and engineering of thermal spray coatings*. John Wiley & Sons, 2008.

[29] Darío Fernando Zambrano Mera. Estudio calorimétrico mediante análisis por DSC y TGA de la degradación de recubrimientos de YSZ depositados por Air Plasma Spray, 2015.

[30] University of Stony Brook, Materials science engineering data: pictures, micrographs, spectra. http://www.matscieng.sunysb.edu/pictures/srini/300c2d.jpg.

[31] Gopal Dwivedi, Toshio Nakamura, and Sanjay Sampath. Controlled introduction of anelasticity in plasma-sprayed ceramics. *Journal of the American Ceramic Society*, 94:s104–s111, 2011.

[32] R Darolia. Thermal barrier coatings technology: critical review, progress update, remaining challenges and prospects. *International materials reviews*, 58(6):315–348, 2013.

[33] Sanjay Sampath, Uwe Schulz, Maria Ophelia Jarligo, and Seiji Kuroda. Processing science of advanced thermal-barrier systems. *MRS bulletin*, 37(10):903–910, 2012.

[34] Sudhangshu Bose. *High temperature coatings*. Butterworth-Heinemann, 2011.

[35] Roger C Reed. *The superalloys: fundamentals and applications*. Cambridge university press, 2008.

[36] Alvarado Orozco, Juan Manuel. Kinetics Study and Characterization of Thermally Grown Oxide on Commercial β-(Ni,Pt)Al Bond Coats used in Thermal Barrier Coating Systems for Gas Turbine Engine Applications, 2012.

[37] Nageswara Rao Muktinutalapati. Materials for gas turbines–an overview. In *Advances in Gas Turbine Technology*, page 303. InTech, 2011.

[38] Meherwan P Boyce. *Gas turbine engineering handbook*. Elsevier, 2011.

[39] Brian Gleeson. Thermal barrier coatings for aeroengine applications. *Journal of propulsion and power*, 22(2):375–383, 2006.

[40] Adriaan Thomas Jacques Verbeek. *Plasma sprayed thermal barrier coatings: production, characterization and testing*. Technische Universiteit Eindhoven, 1992.

[41] Carlos G Levi. Emerging materials and processes for thermal barrier systems. *Current Opinion in Solid State and Materials Science*, 8(1):77–91, 2004.

[42] Paolo Francesco Manicone, Pierfrancesco Rossi Iommetti, and Luca Raffaelli. An overview of zirconia ceramics: basic properties and clinical applications. *Journal of dentistry*, 35(11):819–826, 2007.

[43] Anthony G Evans, David R Clarke, and Carlos G Levi. The influence of oxides on the performance of advanced gas turbines. *Journal of the European Ceramic Society*, 28(7):1405–1419, 2008.

[44] Giovanni Di Girolamo, Caterina Blasi, Monica Schioppa, and Leander Tapfer. Structure and thermal properties of heat treated plasma sprayed ceria–yttria co-stabilized zirconia coatings. *Ceramics International*, 36(3):961–968, 2010.

[45] CH Lee, HK Kim, HS Choi, and HS Ahn. Phase transformation and bond coat oxidation behavior of plasma-sprayed zirconia thermal barrier coating. *Surface and Coatings Technology*, 124(1):1–12, 2000.

[46] Andrés González, John Henao, Andrés Felipe Díaz, Esperanza López, and Fabio Vargas. Influencia de los parámetros de proyección térmica en la microestructura de los recubrimientos de circona-alúmina y circonaceria usados como barreras térmicas. *Revista Latinoamericana de Metalurgia y Materiales*, 33(2):272–281, 2013.

[47] Hanshin Choi, Hyungjun Kim, and Changhee Lee. Phase evolutions of plasma sprayed ceria and yttria stabilized zirconia thermal barrier coating. *Journal of materials science letters*, 21(17):1359–1361, 2002.

[48] GM Ingo, E Paparazzo, O Bagnarelli, and N Zacchetti. XPS studies on cerium, zirconium and yttrium valence states in plasma-sprayed coatings. *Surface and Interface Analysis*, 16(1-12):515–519, 1990.

[49] Bin Ma, Yao Li, and Ke Su. Characterization of ceria–yttria stabilized zirconia plasma-sprayed coatings. *Applied Surface Science*, 255(16):7234–7237, 2009.

[50] Anthony Glyn Evans, DR Mumm, JW Hutchinson, GH Meier, and FS Pettit. Mechanisms controlling the durability of thermal barrier coatings. *Progress in materials science*, 46(5):505–553, 2001.

[51] Gregoire Witz, Valery Shklover, Walter Steurer, Sharath Bachegowda, and Hans-Peter Bossmann. Phase evolution in yttria-stabilized zirconia thermal barrier coatings studied by rietveld refinement of x-ray powder diffraction patterns. *Journal of the American Ceramic Society*, 90(9):2935–2940, 2007.

[52] F Cernuschi, L Lorenzoni, S Ahmaniemi, P Vuoristo, and T Mäntylä. Studies of the sintering kinetics of thick thermal barrier coatings by thermal diffusivity measurements. *Journal of the European Ceramic Society*, 25(4):393–400, 2005.

[53] Branko N. Popov. *Corrosion Engineering -Principles and Solved Problems*. Elsevier, 2015.

[54] Robert A Rapp. Hot corrosion of materials: a fluxing mechanism? *Corrosion science*, 44(2):209–221, 2002.

[55] Neil Birks, Gerald H Meier, and Frederick S Pettit. *Introduction to the high temperature oxidation of metals*. Cambridge University Press, 2006.

[56] Isidor Zaplatynsky. Reactions of yttria-stabilized zirconia with oxides and sulfates of various elements. Technical report, NASA, 1978.

[57] Douglas W McKee and Paul A Siemers. Resistance of thermal barrier ceramic coatings to hot salt corrosion. *Thin Solid Films*, 73(2):439–445, 1980.

[58] AS Nagelberg. Destabilization of yttria-stabilized zirconia induced by molten sodium vanadate-sodium sulfate melts. *Journal of the electrochemical society*, 132(10):2502–2507, 1985.

[59] YS Zhang and RA Rapp. Solubilities of CeO_2, HfO_2 and Y_2O_3 in fused Na_2SO_4-30 mol$\%$ $NaVO_3$ and CeO_2 in pure Na_2SO_4 at 900 $^\circ$C. *Corrosion*, 43(6):348–352, 1987.

[60] RL Jones, CE Williams, and AJ Jones. Reaction of vanadium compounds with ceramic oxides. *Journal of Electrochemical Society*, 133(1), 1986.

[61] I Gurrappa. Thermal barrier coatings for hot corrosion resistance of CM 247 LC superalloy. *Journal of materials science letters*, 17(15):1267–1269, 1998.

[62] W Hertl. Vanadia reactions with yttria stabilized zirconia. *Journal of applied physics*, 63(11):5514–5520, 1988.

[63] Prabhakar Mohan. Environmental degradation of oxidation resistant and thermal barrier coatings for fuel-flexible gas turbine applications, 2010.

[64] Subramaniam Yugeswaran, Akira Kobayashi, and PV Ananthapadmanabhan. Hot corrosion behaviors of gas tunnel type plasma sprayed $La_2Zr_2O_7$ thermal barrier coatings. *Journal of the European Ceramic Society*, 32(4):823–834, 2012.

[65] Carlos G Levi, John W Hutchinson, Marie-Hélène Vidal-Sétif, and Curtis A Johnson. Environmental degradation of thermal-barrier coatings by molten deposits. *MRS bulletin*, 37(10):932–941, 2012.

[66] Zheng Chen, NQ Wu, J Singh, and SX Mao. Effect of Al_2O_3 overlay on hot-corrosion behavior of yttria-stabilized zirconia coating in molten sulfate-vanadate salt. *Thin solid films*, 443(1-2):46–52, 2003.

[67] Imran Nazir Qureshi, Muhammad Shahid, A Nusair Khan, and Yaseer A Durrani. Evaluation of titanium nitride-modified bondcoat system used in thermal barrier coating in corrosive salts environment at high temperature. *Journal of Thermal Spray Technology*, 24(8):1520–1528, 2015.

[68] Zun Chen, Scott Speakman, Jane Howe, Hsin Wang, Wally Porter, and Rodney Trice. Investigation of reactions between vanadium oxide and plasma-sprayed yttria-stabilized zirconia coatings. *Journal of the European Ceramic Society*, 29(8):1403–1411, 2009.

[69] Zohre Soleimanipour, Saeid Baghshahi, Reza Shoja-razavi, and Mehdi Salehi. Hot corrosion behavior of Al_2O_3 laser clad plasma sprayed YSZ thermal barrier coatings. *Ceramics International*, 42(15):17698–17705, 2016.

[70] DR Clarke and CG Levi. Materials design for the next generation thermal barrier coatings. *Annual review of materials research*, 33(1):383–417, 2003.

[71] MC Mayoral, JM Andrés, MT Bona, V Higuera, and FJ Belzunce. Yttria stabilized zirconia corrosion destabilization followed by Raman mapping. *Surface and Coatings Technology*, 202(21):5210–5216, 2008.

[72] Lei Guo, Mingzhu Li, and Fuxing Ye. Comparison of hot corrosion resistance of $Sm_2Zr_2O_7$ and $(Sm_{0.5}Sc_{0.5})_2Zr_2O_7$ ceramics in Namolten salt. *Ceramics International*, 42(12):13849–13854, 2016.

[73] M Bahamirian, SMM Hadavi, M Farvizi, MR Rahimipour, and A Keyvani. Enhancement of hot corrosion resistance of thermal barrier coatings by using nanostructured $Gd_2Zr_2O_7$ coating. *Surface and Coatings Technology*, 2018.

[74] Morteza Hajizadeh-Oghaz, Reza Shoja Razavi, Ali Ghasemi, and Zia Valefi. Na_2SO_4 and V_2O_5 molten salts corrosion resistance of plasma-sprayed nanostructured ceria and yttria co-stabilized zirconia thermal barrier coatings. *Ceramics International*, 42(4):5433–5446, 2016.

[75] MH Habibi and SM Guo. The hot corrosion behavior of plasma sprayed zirconia coatings stabilized with yttria, ceria, and titania in sodium sulfate and vanadium oxide. *Materials and Corrosion*, 66(3):270–277, 2015.

[76] Vaishak Viswanathan, Gopal Dwivedi, and Sanjay Sampath. Engineered multilayer thermal barrier coatings for enhanced durability and functional performance. *Journal of the American Ceramic Society*, 97(9):2770–2778, 2014.

[77] Abbas Afrasiabi, Mohsen Saremi, and Akira Kobayashi. A comparative study on hot corrosion resistance of three types of thermal barrier coatings: YSZ, YSZ+ Al_2O_3 and YSZ/Al_2O_3. *Materials Science and Engineering: A*, 478(1-2):264–269, 2008.

[78] M Saremi and Z Valefi. Thermal and mechanical properties of nano-ysz–alumina functionally graded coatings deposited by nano-agglomerated powder plasma spraying. *Ceramics International*, 40(8):13453–13459, 2014.

[79] Dowon Song, Taeseup Song, Ungyu Paik, Guanlin Lyu, and Yeon-Gil Jung. Hot corrosion behavior in thermal barrier coatings with heterogeneous splat boundary. *Corrosion Science*, page in press, 2019.

[80] PG Lashmi, Sumil Majithia, V Shwetha, N Balaji, and ST Aruna. Improved hot corrosion resistance of plasma sprayed ysz/$gd_2zr_2o_7$ thermal barrier coating over single layer ysz. *Materials Characterization*, 147:199–206, 2019.

[81] A Keyvani, M Saremi, and M Heydarzadeh Sohi. Microstructural stability of zirconia–alumina composite coatings during hot corrosion test at 1050°c. *Journal of Alloys and Compounds*, 506(1):103–108, 2010.

[82] AH Pakseresht, AH Javadi, E Ghasali, A Shahbazkhan, and S Shakhesi. Evaluation of hot corrosion behavior of plasma sprayed thermal barrier coatings with graded intermediate layer and double ceramic top layer. *Surface and Coatings Technology*, 288:36–45, 2016.

[83] A Keyvani and M Bahamirian. Hot corrosion and mechanical properties of nanostructured Al_2O_3/CSZ composite TBCs. *Surface Engineering*, 33(6):433–443, 2017.

[84] Ahmad Keyvani. Microstructural stability oxidation and hot corrosion resistance of nanostructured Al_2O_3/YSZ composite compared to conventional YSZ TBC coatings. *Journal of Alloys and Compounds*, 623:229–237, 2015.

[85] Lewis E Shoemaker. Alloys 625 and 725: trends in properties and applications. *Superalloys*, 718:625–706, 2005.

[86] GD Smith, DJ Tillack, and SJ Patel. Alloy 625: impressive past, significant presence, awesome future. *Superalloys*, 718:625–706, 1991.

[87] HX Hu, YG Zheng, and CP Qin. Comparison of inconel 625 and inconel 600 in resistance to cavitation erosion and jet impingement erosion. *Nuclear Engineering and Design*, 240(10):2721–2730, 2010.

[88] Dominic Mercier, Bryan D Gauntt, and Mathieu Brochu. Thermal stability and oxidation behavior of nanostructured nicocraly coatings. *Surface and Coatings Technology*, 205(17-18):4162–4168, 2011.

[89] Masatomo Yashima, Kenji Morimoto, Nobuo Ishizawa, and Masahiro Yoshimura. Diffusionless tetragonal–cubic transformation temperature in zirconia–ceria solid solutions. *Journal of the American Ceramic Society*, 76(11):2865–2868, 1993.

[90] Masatomo Yashima, Haruo Arashi, Masato Kakihana, and Masahiro Yoshimura. Raman scattering study of cubic–tetragonal phase transition in $Zr_{1-x}Ce_xO_2$ solid solution. *Journal of the American Ceramic Society*, 77(4):1067–1071, 1994.

[91] Vaishak Viswanathan, Gopal Dwivedi, and Sanjay Sampath. Multilayer, multimaterial thermal barrier coating systems: design, synthesis, and performance assessment. *Journal of the American Ceramic Society*, 98(6):1769–1777, 2015.

[92] Oerlikon Metco. SinplexPro Plasma Spray gun.

[93] ASM Thermal Spray Society (TSS). *Accepted Practice to Test Bond Strength of Thermal Spray Coatings*, 2013.

[94] J Zhang and V Desai. Determining thermal conductivity of plasma sprayed TBC by electrochemical impedance spectroscopy. *Surface and Coatings Technology*, 190(1):90–97, 2005.

[95] M Leoni, RL Jones, and P Scardi. Phase stability of scandia–yttria-stabilized zirconia TBCs. *Surface and coatings technology*, 108:107–113, 1998.

[96] Jing Wu, Hong-Bo Guo, Le Zhou, Lu Wang, and Sheng-Kai Gong. Microstructure and thermal properties of plasma sprayed thermal barrier coatings from nanostructured YSZ. *Journal of Thermal Spray Technology*, 19(6):1186–1194, 2010.

[97] Vanni Lughi and David R Clarke. Transformation of Electron-Beam Physical Vapor-Deposited 8 wt$\%$ Yttria-Stabilized Zirconia Thermal Barrier Coatings. *Journal of the American Ceramic Society*, 88(9):2552–2558, 2005.

[98] Robert A Rapp. Chemistry and electrochemistry of hot corrosion of metals. *materials science and engineering*, 87:319–327, 1987.

[99] M Seiersten and P Kofstad. The effect of SO_3 on vanadate-induced hot corrosion. *High Temperature Technology*, 5(3):115–122, 1987.

[100] S Erdei and FW Ainger. Crystal growth of YVO_4 using the LHPG technique. *Journal of crystal growth*, 128(1-4):1025–1030, 1993.

[101] A Keyvani, M Saremi, and M Heydarzadeh Sohi. Oxidation resistance of YSZ-alumina composites compared to normal YSZ TBC coatings at 1100 °C. *Journal of alloys and compounds*, 509(33):8370–8377, 2011.

[102] Reza Ghasemi, Reza Shoja-Razavi, Reza Mozafarinia, and Hossein Jamali. Comparison of microstructure and mechanical properties of plasma-sprayed nanostructured and conventional yttria stabilized zirconia thermal barrier coatings. *Ceramics International*, 39(8):8805–8813, 2013.

[103] Christopher C Berndt. Tensile adhesion testing methodology for thermally sprayed coatings. *Journal of materials engineering*, 12(2):151–158, 1990.

[104] CRC Lima and JM Guilemany. Adhesion improvements of thermal barrier coatings with hvof thermally sprayed bond coats. *Surface and Coatings Technology*, 201(8):4694–4701, 2007.

[105] Luis Tobón, César Barrios, Darío Zambrano, and Alejandro Toro. Análisis morfológico de la porosidad de un sistema de barrera térmica sometido a cargas térmicas cosntantes. *Revista Colombiana de Materiales*, (5):35–41, 2014.

[106] Anand A Kulkarni, Allen Goland, Herbert Herman, Andrew J Allen, Jan Ilavsky, Gabrielle G Long, and Francesco De Carlo. Advanced microstructural characterization of plasma-sprayed zirconia coatings over extended length scales. *Journal of Thermal Spray Technology*, 14(2):239–250, 2005.

[107] Anand Kulkarni, A Vaidya, A Goland, S Sampath, and H Herman. Processing effects on porosity-property correlations in plasma sprayed yttria-stabilized zirconia coatings. *Materials Science and Engineering: A*, 359(1-2):100–111, 2003.

[108] M Karger, R Vassen, and D Stover. Atmospheric plasma sprayed thermal barrier coatings with high segmentation crack densities: Spraying process, microstructure and thermal cycling behavior. *Surface and Coatings Technology*, 206(1):16–23, 2011.

[109] Manish Madhwal, Eric H Jordan, and Maurice Gell. Failure mechanisms of dense vertically-cracked thermal barrier coatings. *Materials Science and Engineering: A*, 384(1-2):151–161, 2004.

[110] HB Guo, R Vassen, and D Stover. Atmospheric plasma sprayed thick thermal barrier coatings with high segmentation crack density. *Surface and Coatings technology*, 186(3):353–363, 2004.

[111] Biao Li, Xueling Fan, Hiroshi Okada, and Tiejun Wang. Mechanisms governing the failure modes of dense vertically cracked thermal barrier coatings. *Engineering Fracture Mechanics*, 189:451–480, 2018.

[112] P Fauchais, A Vardelle, M Vardelle, and M Fukumoto. Knowledge concerning splat formation: an invited review. *Journal of Thermal Spray Technology*, 13(3):337–360, 2004.

[113] S Sampath and X Jiang. Splat formation and microstructure development during plasma spraying: deposition temperature effects. *Materials Science and Engineering: A*, 304:144–150, 2001.

[114] A Nusair Khan and J Lu. Behavior of air plasma sprayed thermal barrier coatings, subject to intense thermal cycling. *Surface and Coatings Technology*, 166(1):37–43, 2003.

[115] AGEA Rabiei and AG Evans. Failure mechanisms associated with the thermally grown oxide in plasma-sprayed thermal barrier coatings. *Acta materialia*, 48(15):3963–3976, 2000.

[116] Feifei Zhou, You Wang, Liang Wang, Yaming Wang, Wenlong Chen, Changxiang Huang, and Min Liu. Synthesis and characterization of nanostructured t'-YSZ spherical feedstocks for atmospheric plasma spraying. *Journal of Alloys and Compounds*, 740:610–616, 2018.

[117] P Mohan, T Patterson, VH Desai, and YH Sohn. Degradation of free-standing air plasma sprayed conicraly coatings by vanadium and phosphorus pentoxides. *Surface and Coatings Technology*, 203(5-7):427–431, 2008.

A ANNEX 1: Academic production and Future research

A.1 Academic production

Congress presentations:

- Hot Corrosion behavior of Yttria-Stabilized Zirconia powders on presence of Na_2SO_4+V_2O_5 molten salts. XXVI International Materials Research Congress 2017, Cancun México.

Publications:

- Hot Corrosion mechanism of Yttria-Stabilized Zirconia powder in the presence of molten Na_2SO_4+V_2O_5 salts, *Accepted*, Rare Metals, 2020.
- Hot corrosion and thermal shock resistance of CYSZ/YSZ bilayer thermal barrier coatings applied onto Ni-base superalloy, *In revision*.
- Hot corrosion behavior of CYSZ/YSZ bilayer coatings deposited by atmospheric plasma spay in Na_2SO_4+V_2O_5 molten salts, *In construction*.

Works in co-authorship:

- Efecto de la microestructura sobre la resistencia a la corrosión en caliente de recubrimientos de circonia estabilizada con itria y ceria (CYSZ) depositadas por aspersión térmica por plasma atmosférico. Congreso internacional de materiales- CIM 2019, Bucaramanga, Colombia.
- Influence of heat treatment on the abrasive and erosive wear resistance of WC-10Co4Cr coating deposited onto stainless steel by HVOF, XXVIII International Materials Research Congress 2019, Cancun México

A.2 Future research

- Thermomechanical behavior of CYSZ/YSZ coatings: How to avoid the generation of vertical cracks.
- Hot corrosion and thermal shock resistance of CYSZ with DVC microstructure deposited using atmospheric plasma spray.

B | ANNEX 2: Rietveld procedure in GSAS software

B.1 Create your calibration pattern

First you must have three types of files:

- X-ray diffraction pattern of LaB_6 or Silicon (Calibration patterns used in a X-ray equipment) in .raw format measured with same conditions of your samples
- Crystallographic information file (.CIF)
- Instrument parameter file (.prm)

Now you can start with create your calibration file:

1. Phase tab: Add phase (.CIF file)
2. Powder tab: Add new histogram and then add .raw and .prm files
3. Powder tab: Edit background, Option 1 with 8 terms
4. Profile tab: Change profile function to type 4
5. Press Powpref button
6. Press Genles button
7. Profile tab: Shft + Genles x 2
8. Phase tab: Refine cell + Genles
9. Profile tab: LX + Genles
10. Profile tab: GV + Genles
11. Profile tab: GW + Genles
12. Profile tab: GU + (Damping 5) + Genles
13. Profile tab: GP + Genles
14. Ls controls tab: Set Marquardt damping in 1.15
15. Profile tab: S/L + Genles

16. Profile tab: H/L + Genles
17. Phase tab: Select atoms + U + Damping 5 + Genles x 2
18. Phase tab: Select atoms + X + Damping 5 + Genles x 2
19. Phase tab: Select atoms + F + Damping 5 + Genles x 3
20. Profile tab: Ptec + Genles
21. Powder tab: Ratio + Genles
22. Powder tab: POLA + Genles

Note: Always register Chi^2 and R^2 values in each step, if these values do not change, do not save the modification.

B.2 Multiple phases refinement

Similar to last section, you must have:

- .CIF files of each phase
- Experimental X-ray diffraction pattern with .raw extension and instrument parameter file created in last section.

Now, to start the refinement:

1. Phase tab: Add each phase and then add your .CIF file
2. Powder tab: Add new histogram and then add .raw and .prm files
3. Powder tab: Edit background, Option 1 with 8 terms
4. Press Powpref button
5. Press Genles button
6. Scaling tab: Deselect scale factor and select refine each phase (Phase fractions) + Genles
7. Scaling tab: Select scale factor
8. Profile tab: Select shft + Genles (Fist in bigger phase) and then, repeat this action in each phase (from the largest to the smallest)
9. Phase tab: Refine cell + Genles (repeat this action in each phase from the largest to the smallest)

Now make these actions in each phase (Bigger phase first):

10. Profile tab: LX + Genles
11. Profile tab: GU + Damping 5 + Genles

12. Profile tab: GP + Genles
13. Profile tab: S/L + Set Marquardt damping in 1.15 + Genles
14. Profile tab: S_{HKL}
15. Phase tab: Select atoms + U + Damping 5 + Genles
16. Phase tab: Select atoms + X + Damping 5 + Genles
17. Phase tab: Select atoms + F + Damping 5 + Genles
18. Profile tab: Ptec

Finally, for all phases:

19. Powder tab: Ratio + Genles
20. Powder tab: POLA + Genles